Winter 1-15-2021

Measuring and Manipulating Tension-Dependent Behavior of Mechanosensitive Ion Channels

Angela M. Schlegel
Washington University in St. Louis

WASHINGTON UNIVERSITY IN ST. LOUIS

Division of Biology and Biomedical Sciences
Plant and Microbial Biosciences

Dissertation Examination Committee:
Elizabeth S. Haswell, Chair
Philip V. Bayly
Jianmin Cui
Ram Dixit
Joseph M. Jez

Measuring and Manipulating Tension-Dependent Behavior of Mechanosensitive Ion Channels

by

Angela M. Schlegel

A dissertation presented to
The Graduate School
of Washington University in
partial fulfillment of the
requirements for the degree
of Doctor of Philosophy

January 2021
St. Louis, Missouri

Table of Contents

List of Figures

List of Tables

Acknowledgments

I first would like to thank the funding sources that made this work possible. My research in the Haswell lab was primarily supported by funding from the Gordon and Betty Moore Foundation and an HHMI-Simons Foundation Faculty I also gratefully acknowledge generous funding from the Spencer T. and Ann W. Olin Fellowship for Women in Graduate Study and the William H. Danforth Plant Sciences Fellowship, which have provided me with financial support for the entirety of my graduate career.

Next are my mentors, advisors, and teachers. I have been lucky to have worked in research my entire life in the labs of Dr. Anna Dornhaus, Dr. David Gang, Dr. Sam Campos, and, finally, Dr. Liz Haswell. Their mentorship, both professionally and personally, have tremendously shaped the scientist I am today and I am grateful for their time and effort in working with me. I also want to thank the members of those labs for comradery, assistance, support, and friendship, particularly Dr. Hyun Jo Koo and Dr. Eric McDowell from Gang Lab, Dr. Matthew Bronnimann and Janice Chapman from Campos Lab, and Emma January, Dr. Grigory Maksaev, Ryan Richardson, and Dr. Maggie Wilson from Haswell Lab. Finally, I had the tremendous pleasure of being taught by many outstanding educators over the years. Shoutouts to Ms. Guevara, Dr. Furnier, Mx. B-A, Ms. Wilch, Dr. Kevin Vogel, Dr. Matt Herron, Mr. Goldsmith, Professor Jackson, and Dr. Hazzard - thank you for your enthusiasm, your outreach, and your energy. I hope I’ve made you all proud.

Finally, the sincerest and biggest of thank yous and love to my community, my friends, and my family. I am fortunate to have far too many of you to thank here, which would require a separate dissertation, but big ups to my Tucson best friends Emily (the bestest of friends), Julia, Karen, and Troy, my St. Louis crew Sarah, Chris (Bowie), Sadie, and Monica. The community I have found here in St. Louis has been incredible and has truly made this a second home, it is with the utmost gratitude that I write this. Thank you especially to Connie at the Hillman Hall coffee shop, Cliff, Danielle, Phoebe, and Shane at Left Bank Books, and Gena, Alex and Sarah T. at Subterranean Books.

My family have always been right there for me from the very beginning, supporting me wherever my interests have led, and I love you all. Mom, Kristian, Valerie, Dad, Rebecca, Kathy, Karen, and Tim – thank you especially for your support these past seven years. It has meant the world.

Papa and Papa Jack – this one's for you. I miss you and wish I could share this with you both. It's very "cool, man"!

Angela M. Schlegel

Washington University in St. Louis

January 2021

Dedicated to my grandpas, Dr. Harry M. Graham and Mr. John W. “Jack” Schlegel.

ABSTRACT OF THE DISSERTATION

Measuring and Manipulating Tension-Dependent Behavior of Mechanosensitive Ion Channels

by

Angela M. Schlegel

Mechanical forces play critical roles throughout the lives of all organisms and, as such, diverse arrays of mechanotransduction systems have evolved to detect and initiate responses to force. Many mechanotransduction systems consist of mechanosensitive (MS) ion channels, membrane pores that open in response to sufficient mechanical force. My dissertation focuses on both the study and application of force-dependent conformational changes of MS channels. I tested whether charged pore-lining residues R326 and D327 of the *Arabidopsis thaliana* mitochondrial MS channel MSL1 function in inward rectification or gating kinetics. Mutating these residues showed no effect on MSL1 rectification; however, these residues are important for gating transitions and open state stability of MSL1. I also attempted to develop a genetically-encoded, fluorescence-based membrane tension sensor using the Mechanosensitive ion channel of Small conductance (MscS) from *E. coli* as a tension-sensing scaffold and circularly permuted GFP (mcpGFP) as the fluorescence reporter. While responses to tension by sensor candidates could not be ruled out, signal changes from mcpGFP that were not dependent on the tension-sensing scaffold dominated sensor responses to osmotic shock. Finally, I developed a detailed protocol for single-channel analysis of plant MS

channels using patch-clamp electrophysiology in *E. coli* spheroplasts. This protocol provides users with detailed descriptions covering sample prep through data analysis of a typical experiment and includes equipment and set-up descriptions geared towards the inexperienced user. Thus my dissertation advances the study of plant mechanobiology by increasing knowledge about the function, study, and application of MS ion channels.

Chapter 1: Introduction

1.1. Mechanical Forces Impact Living Organisms via Mechanotransducers

Mechanical forces play many important roles in living organisms. These mechanical forces can arise from external sources, internal sources, or a combination of the two, as external forces or stimuli often lead to changes in the internal mechanical environment of a given organism. We can broadly think of mechanical forces as arising from three major sources: physical contact, osmotic homeostasis, and environmental factors like gravity and air pressure, responses to which depend on the magnitude, location, and frequency of the specific force. Of course, mechanical forces can arise from multiple types of sources and the sum of these forces is ultimately what will dictate a given response.

Physical contact generates many types of stress, including shear stress, pressure, stretch, and compression. Responses to physical contact can include immediate conformational changes, signaling responses, or transcriptional changes. In the vascular systems of multicellular animals, arterial stretching caused by high blood pressure triggers the baroreflex response, a form of rapid negative feedback that decreases heart rate to reduce pressure (Teng et al., 2015). In contrast, perturbations of shear stress in arteries lead to altered gene expression and more long-tern responses (Lim et al., 2018). In plants, touch-based interactions can arise from encountering obstacles both biotic and abiotic in the environment, which include both gentle and

harsh, damaging stimuli that lead to distinct responses. In *Arabidopsis*, leaf damage caused by physical damage triggers production of electrical signals and defense responses, which does not occur upon gentle touch (Mousavi et al., 2013; Salvador-Recatalà, 2016). In contrast, repeated light touching of *Arabidopsis* plants over multiple days produced shorter plants (Jensen et al., 2017). Thus the same type of stimulation, touch, but of different magnitude can produce very different plant responses.

Osmotic forces arise from imbalances in solute across semi-impermeable membranes and can be the result of normal variations in osmotic homeostasis or abnormal imbalances. Such stresses typically trigger cellular responses to restore or re-establish osmotic homeostasis, and in multicellular organisms can occur in cell types exposed directly to osmotic changes, as with epithelial cells in renal tubes (Lim et al., 2018). Osmotic forces are particularly critical for plants, as turgor pressure helps plants maintain their shape, is required for cell elongation, and is critical for reproduction. Cell wall structure and orientation are critical for determining cell shape and length, with cell wall modifications controlling turgor-driven cell expansion (Hamant & Haswell, 2017), though this process must be carefully regulated to prevent cell damage (E. S. Hamilton et al., 2015; Eric S. Hamilton & Haswell, 2017). For bacteria, being single-celled organisms, environmental solute changes have direct, immediate consequences for cell shape, size (Rojas et al., 2014), and the balance between free and macromolecule-occupied cell volume, requiring frequent adjustments to maintain proper homeostasis (Wood, 2011).

Gravity is also an important and ever-present influence on living organisms. In plants, growth in response to gravity, or gravitropism, can be difficult to separate from growth due to changes in body structure and mass, particularly for trees (Hamant & Moulia, 2016; Roignant et al., 2018). While mechanosensitive ion channels, described below, have long been hypothesized to sense and signal in response to gravity as gravity perception is associated with Ca^{2+} flux (Eric S. Hamilton et al., 2015), no definitive proof has emerged with respect to this connection, thus the way in which gravity itself is sensed is uncertain.

To detect and respond to these mechanical forces, living organisms employ a wide array of mechanotransductory systems that can range from single macromolecules to entire tissues and structures. A mechanotransductory system detects and responds to mechanical force, either directly or by triggering downstream signaling processes required for force response (Hamant & Haswell, 2017; Hamant & Moulia, 2016; Lim et al., 2018; Persat, 2017; Persat et al., 2015). Mechanotransductory systems exists at many different levels and can include entire tissues or appendages, cells, or single proteins that may act solely in their mechanical function or may act in multiple ways. For single-celled organisms, there is no distinction between mechanosensing and non-mechanosensing tissues. Various species of bacteria often rely on detection of physical obstacles by cell extensions like flagella (Belas, 2014; Gode-Potratz et al., 2011) and by changes in the way they interact with their surroundings, for example upon encountering adhesive surfaces or experiencing fluid flow while adhered (Alsharif et al., 2015).

For multicellular organisms, mechanotransductory systems exist at the organellar through tissue levels and can function in one or multiple systems. Many of these systems utilize the cytoskeleton as a way to transmit forces between or within single cells. For force transmission between the cytoskeleton and plasma membrane, this may involve membrane attachment points such as ankyrin repeats or actin binding sites within integral membrane proteins or interactions with the lipid bilayer itself (Huse, 2017; Lim et al., 2018). For force transmission over longer distances multiple sets of linkages may be involved, as with actin-based connections between the Linker of Nucleoskeleton Complexes (LINC) and focal adhesion zones (FAZs), which in turn connect to the extracellular matrix (Nourse & Pathak, 2017). In addition, multicellular animals typically possess dedicated mechanosensory cells specialized to respond to internal and external mechanical forces,

In plants, tissue-level mechanotransductory systems control some of the most iconic and dramatic mechanical force responses. For example, Venus flytraps (*Dionaea*) possess trigger hairs on the inner portions of trap lobes that, when deflected beyond a specific level of deformation with a minimum level of force trigger action potentials, trap closure, and the production of digestive enzymes (S. Scherzer et al., 2019; Sönke Scherzer et al., 2017; Volkov et al., 2013).

To summarize, mechanical forces emerge from internal and external forces to act throughout the life of a given organism, which depends on different types of mechanotransduction systems for proper interpretation and response. By studying specific mechanotransductory systems, we can gain a better idea of how different types

of mechanical forces are or are not distinguished and how mechanosensation interacts with other perceptive processes.

1.2. Mechanosensitive Ion Channels: Ubiquitous Mechanotransducers

Mechanosensitive (MS) ion channels are a widespread mechanotransductory mechanism found in every kingdom of life (Anna Kloda & Martinac, 2001; Kung et al., 2010; Ranade et al., 2015; Eric S. Hamilton et al., 2015). MS ion channels are ion channels whose main opening, or gating, stimulus is mechanical force. Unlike many other groups of ion channels, such as ligand-gated or voltage-gated ion channels, there currently is no known “mechanosensitive” domain that can be used to identify novel channels, although conservation of the pore-lining domains defines multiple MS channel families including Piezos, MscS, and MscL families (B. Coste et al., 2010; Pivetti et al., 2003). In addition, there have only been extremely limited reports of separable tension-sensing and pore domains for MS ion channels. For example, non-pore domain residues 1-2190 aa of mPiezo1 can confer mechanosensitivity to the otherwise tension-insensitive acid-sensing ion channel (ASIC), indicating separate mechanosensing and conducting regions (Q. Zhao et al., 2016). Instead, founding members of MS channel families are often identified in functional screens or reverse genetic approaches to identify the proteins underlying specific stretch-activated currents.

MS channels can be found in many types of cellular and organellar membranes (Basu & Haswell, 2017; Ranade et al., 2015; Murthy et al., 2018) and in plants have been identified in the plasma membrane as well as membranes of chloroplasts (Haswell

& Meyerowitz, 2006), mitochondria (C. P. Lee et al., 2016), and vacuoles (Gobert et al., 2007; Maathuis, 2011). As with localization, the ion selectivity of MS channels can also vary dramatically, as evidenced by the MscS family, which contains relatively nonselective (Petrov et al., 2013; S. Sukharev, 2002; E. S. Hamilton et al., 2015; G. Maksaev & Haswell, 2012), anion-selective (Y. Nakayama et al., 2007), and cation-selective members (Börngen et al., 2010; Anna Kloda & Martinac, 2001; Yoshitaka Nakayama et al., 2013).

There are two main mechanisms by which MS ion channels are gated: tether-gating and non-tether-gating. Non-tether-gated MS channels are those in which forces transmitted solely through the membrane are sufficient for channel gating. In contrast, tether-gated MS channels are thought to gate upon tension application to the channel or the surrounding bilayer via protein tether, sufficiently altering protein-lipid interactions such that the MS channel open state is favored (Charles D. Cox et al., 2019; Kung, 2005). Multiple broad models describe the types of interactions that may be involved, with varying applicability to a given channel depending on things like the profile of that channel's membrane interface and the degree of interaction between a given MS channel and the membrane (Charles D. Cox et al., 2019; Phillips et al., 2009; Eric S. Hamilton et al., 2015).

One of these models is the hydrophobic mismatch model, in which maximizing interactions between hydrophobic parts of the MS channel and the lipid bilayer is key. Under normal conditions, these hydrophobic interactions are maximized by the closed state of the MS channel. Upon increases in membrane tension, the bilayer thins,

disrupting these interactions and forcing tilting of the transmembrane portion of the MS channel to restore hydrophobic interactions, causing opening of the MS channel. Hydrophobic mismatch is thought to be a major driver in gating of the *E. coli* MS channel MscL. The gating tension threshold of MscL decreases with shortening lipid tail lengths, suggesting the thickness of the bilayer governs closed vs open state equilibrium (T. Nomura et al., 2012; Perozo et al., 2002).

The second model is the lipid disorder or curvature model, in which the presence of an MS channel increases the amount of disorder in a bilayer, which is minimized under normal conditions by the closed state of the MS ion channel. In a similar manner to the hydrophobic mismatch model, changes in membrane tension increase the amount of disorder at the bilayer-channel interface, which are reduced by MS channel gating. Evidence for this model includes activation of MS channels like MscS by addition of lysophosphatidylcholine (LPC) (Vásquez et al., 2008) and molecular dynamics simulations in which membrane curvature is altered to simulate LPC insertion (Zhu et al., 2020).

Additionally, some MS ion channels induce membrane curvature in the closed state, which has been proposed to enhance mechanosensitivity by enhancing energetic favorability of channel gating (Deng et al., 2020; Haselwandter & MacKinnon, 2018). Using cryoEM, such membrane curvature has been shown for mPiezo1 (Guo & MacKinnon, 2017) and predicted for *A. thaliana* MSL1 (Deng et al., 2020). For a two-state MS ion channel with a tension-dependent equilibrium between closed and open states, increased amounts of in-plane area expansion during gating favors the open

state by increasing the drop in free energy occurring during gating (Wiggins & Phillips, 2005). By greatly increasing membrane curvature, the amount of in-plane area increase for the same amount of channel conformation change can be increased, enhancing the favorability of the open state in the presence of heightened membrane tension (Haselwandter & MacKinnon, 2018).

Additionally, lipids may act as ligands for multiple MS ion channels, with movement of lipids in and out of MS channel crevices driving gating transitions. This has been demonstrated for the K^+ channel TRAAK, whose closed state is defined by pore blockage by a lipid acyl chain. Opening of TRAAK involves rotation of its TM4 helix on its hinge, preventing lipid insertion and permitting ion flow through the now-open pore (Brohawn et al., 2014). The lipids-as-ligands model was also initially proposed for *E. coli* MscS gating based on the presence of lipids within “pockets” near the cytoplasmic face of MscS and gating by LPC addition. However, the altered position of MscS within the membrane and additional lipid presence in the cryoEM MscS structure generated by (Reddy et al., 2019) disagrees with this model.

Protein tethers, including those connected to the cytoskeleton and extracellular matrix, may also serve as the primary source of gating force for or may modulate force sensitivity of MS channels. For example, gating of the MS channel NOMPC from *Drosophila melanogaster* requires the presence of multiple Ankyrin repeats in its N-terminus, which facilitate interactions with microtubules. These Ankyrin repeats also represent a separable mechanosensitive domain, as fusions between the NOMPC N-

terminus and the typically force-insensitive channel Kv1.2 confer mechanosensitive gating to Kv1.2 (W. Zhang et al., 2015).

In addition, mPiezo1 can be activated by force solely transmitted through the membrane based, as indicated by experiments involving mPiezo1 incorporation into artificial lipid bilayers (Bertrand Coste et al., 2012; Syeda et al., 2016). However, the presence of the cytoskeleton modulates the tension sensitivity of mPiezo1 activation, as mPiezo1 gating tension decreases in cytoskeleton-free blebs compared to normal cell-attached patches (Charles D. Cox et al., 2016). This suggests that mPiezo1 gating is modulated by the cytoskeleton while occurring via the cell membrane. In addition, mPiezo1 can be gated by force applied to artificial tethers attached to extracellular domains of mPiezo1 (Wu et al., 2016). However, whether such tethers exist *in vivo*, or whether the cytoskeletal sensitivity is indirect is unknown.

1.3. MscS is a Well-Studied Non-Tether-Gated MS Ion Channel

One of the most well-studied MS ion channels is the *E. coli* channel Mechanosensitive ion channel of Small conductance. MscS was initially observed as one of two stretch-activated currents in patches of giant *E. coli* spheroplasts (Martinac et al., 1987), which was later attributed to the *yggB* gene (S. Sukharev, 2002; Levina, 1999). MscS is very slightly anion preferring, thought to emerge from selection via side portals in its large cytoplasmic domain (C. D. Cox et al., 2013; S. Sukharev, 2002). MscS is also gated directly in response to changes in membrane tension, as channel activity is detected when MscS is incorporated into artificial bilayers (Okada et al., 2002;

S. Sukharev, 2002). As might be predicted for a non-tether-gated MS channel, lipid composition of the bilayer in which MscS is embedded can have a dramatic effect on gating behavior and properties, with increased curvature promoting opening (Ridone et al., 2015), increased stiffness raising gating tension (Xue et al., 2020), and decreased thickness and unsaturation delaying closure (Ridone et al., 2018). In typical buffer conditions used for patching giant *E. coli* spheroplasts, MscS exhibits a conductance of ~1.2 nS. MscS also exhibits slight inward rectification that increases with higher hydrated ionic radii of the dominant cation present and shows subconducting states with increased prevalence at more extreme negative membrane potentials (C. D. Cox et al., 2013).

Structures of MscS homologs from multiple species, including *E. coli* MscS, have been published, some generated using x-ray crystallography while some, more recently, have been generated using cryoEM. The first *E. coli* MscS crystal structure was published by (Bass et al., 2002), with protein orientation and structural domains confirmed in a subsequent study (Miller, 2003). Eventually classified as a nonconducting structure based on the small pore size (Andriy Anishkin & Sukharev, 2004), this structure revealed MscS to be a homoheptamer, with each monomer containing three transmembrane helices. Later $MscS^{A106V}$ and MscS crystal structures represent the hypothesized open state (Lai et al., 2013; Wang et al., 2008), providing additional data for gating transition simulations and helping support functional relevance of previously identified structural features.

While lipid identities and membrane composition had long been proposed to play important roles in MscS gating, later crystal and cryoEM structures of MscS have solidified the presence of fairly intimate interactions between MscS and individual lipids. The crystal structure of MscS containing an adduct attached to the D67C mutation generated by (Pliotas et al., 2015) possessed lipids or lipid-like molecules in voids formed by TM1, TM2, and TM3b and packed against TM3b, with lipid removal proposed to trigger channel gating. Later cryoEM structures also support the presence of lipids in gaps formed by TM1, TM2, and TM3 and indicate additional interactions between the very N-terminus of MscS and the lipid bilayer (T. Rasmussen et al., 2019; Tim Rasmussen et al., 2019; Reddy et al., 2019).

In addition to closed and open states, MscS exhibits an inactivated state, in which the channel is both nonconducting and unresponsive to tension, even at extreme levels. Inactivation occurs when patches are stimulated by slowly increasing suction or sustained sub-saturating pressures (Akitake et al., 2005; Çetiner et al., 2018), as activation of all channels in a given patch does not appear to trigger inactivation, and has some dependency on the composition of the bilayer in which MscS is embedded (Battle et al., 2009; S. Sukharev, 2002). This inactive state is thought to involve kinking of the pore-lining TM3 helix at G113, while kinking of TM3 at G121 is associated with the closed state (Akitake et al., 2007; Boer et al., 2011b). Recovery from inactivation and transitioning to the closed state requires the loss of added tension to the membrane, as any applied tension delays closed state transitions (Kamaraju et al., 2011). Inactivation does not appear to be a hallmark of the MscS family, as many MscS

family members do not exhibit inactivation (Vásquez, 2013). The inactivated state of MscS is distinct from the desensitized state, in which channels are nonconducting in the presence of increased tension but become conducting upon application of even higher levels of tension, which is thought at least partially to be an artifact of the patch-clamp electrophysiology set-up (Belyy, Kamaraju, et al., 2010).

The primary physiological function of MscS is osmoregulation of *E. coli*, as both MscS and MscL are redundantly required for *E. coli* survival of hypoosmotic shock (Levina, 1999). While additional MscS family members are expressed in *E. coli*, these other channels are not sufficient for severe hypoosmotic shock survival and only help modulate responses to subtle hypoosmotic shock (Bialecka-Fornal et al., 2015). Optical density measurements and single cell microscopy of cells during hypoosmotic shock indicate that swelling occurs during the first 30-50 ms post-shock, followed by post-shock equilibration (Boer et al., 2011b; Buda et al., 2016), further supporting a role for MS channels like MscS in hypoosmotic shock. Additionally, MscS is proposed to sense levels of cytoplasmic crowding through its cage domain as a way to trigger channel closure to prevent excessive ion release (Rowe et al., 2014) There has also been speculation about additional roles for MscS in signaling and division based on its Ca^{2+} conducting ability (C. D. Cox et al., 2013) and interaction with FtsZ (Koprowski et al., 2015), but both of these possibilities lack further substantiation.

1.4. Measuring Mechanical Forces in Living Cells

Full comprehension of mechanotransductory process in living organisms requires quantifying relevant material properties and mechanical forces of the system and process in question. To do this, a variety of approaches and techniques have been developed involving active probing and passive monitoring of living organisms. Some approaches involve applying force to biological molecules, cells, or tissues then monitoring the resulting conformational changes or deformations (Bidhendi et al., 2020; Freikamp et al., 2017; Sen & Kumar, 2010; Siedlik et al., 2016). This can be used to determine material properties of a given system, measure forces being exerted by that system, and examine responses to very controlled amounts of force.

Probing and indentation techniques include atomic force microscopy (AFM), in which surfaces like cells are probed using micro- and nanoscale tips (Kasas et al., 2018). When minimal amounts of force are applied to a given sample, topological maps of cell surface can be generated while application of force. Alternatively, the force applied by the AFM tip can be used to measure resistance from the surface and measure mechanical properties (Sen & Kumar, 2010). Additionally, AFM has been adapted for use with larger tip sizes and samples in a technique called cellular force microscopy (CFM). Both AFM and CFM have recently been used to study plant cells, for which many techniques are too invasive to capture the product of high turgor and cell wall stiffness that governs the balance of mechanical forces in these cells (Braybrook, 2015; Majda et al., 2019; Vogler et al., 2015). Alternatively, individual molecules or

points on cell surfaces can be manipulated and deformed using tools like magnetic and optical tweezers, micropipettes for aspiration (as in some forms of patch-clamp electrophysiology), fluid flow, and simple glass probes for poking (Brenner et al., 2011; Freikamp et al., 2017; Sen & Kumar, 2010).

Alternatively, forces exerted by proteins or organisms can be studied based their impact on deformable surfaces (Brenner et al., 2011; Roca-Cusachs et al., 2017; Sen & Kumar, 2010). In this case, cells or tissues are grown on or near deformable structures made of materials with known material properties, thus their deformation can be used to calculate the force exerted by the biological structure under study. Depending on the cell type and mechanisms of growth, different types of surfaces and structures may be required. For example, the Flexure integrated Lab-on-a-Chip (FiLoC) device measures forces exerted on a flexible cantilever by growing pollen tubes and was used to demonstrate that these growing tubes can exert μN forces (Ghanbari et al., 2018). Pollen tube growth has also been examined in agar of varying stiffnesses to examine effects of environmental mechanical properties on growth rates (Reimann et al., 2020).

Biosensors represent an additional passive system of monitoring and quantifying levels of a particular stimuli, such as mechanical force or membrane tension, over time. A biosensor is a molecular device that measures and reports levels of a particular stimulus. Biosensors conceptually consist of two components, a stimulus sensor and a reporter (Jones et al., 2013). The sensor detects and responds to the stimulus, often by a conformational change. This in turn impacts the reporter in a detectable manner, for example, by altering its fluorescence intensity or spectra. While the sensor and reporter

are often separable proteins or entities, sometimes the same protein or compound serves both functions. This can be more common for chemically synthesized biosensors than genetically-encoded biosensors. However, GFP-based sensors like roGFP (Aller et al., 2013; Meyer & Dick, 2010) and pHluorin (Moseyko & Feldman, 2001) are commonly used genetically-encoded biosensors in which the reporter and sensor are the same protein.

Both chemically-synthesized and genetically-encoded biosensors have been created that measure different types of mechanical forces in living cells. Chemically-synthesized force sensors typically consist of a single unit that can be imaged inside cells and whose responses to deformations and force can be visualized. In the case of fluorescent lipid droplets, droplet shape before and after force application is measured and combined with information on material properties of the droplet to produce maps of exerted force (Campàs et al., 2014). Alternatively, for nanoparticles (Lay et al., 2017, 2018, 2019), nanocrystals (Fischer et al., 2017), and push-pull probes (Colom et al., 2018), changes in force change the qualities of fluorescence emitted, either altering relative intensities of multiple emission wavelengths or fluorescence emission lifetimes. Finally, most genetically-encoded force sensors published to date rely on a FRET-based reporting system, in which members of a FRET pair are separated by a compressible protein linker. Changes in force result in altered separation between FRET pair components, leading to detectable changes in the FRET ratio (W. Li et al., 2018; Meng et al., 2008). Thus, many options exist for measuring force in living organisms, however, choosing a specific tool must keep in mind factors including the

location in which the forces of study occur, the magnitude of those forces, and the timescale and degree of expected force change.

As described above, mechanobiology is an incredibly rich topic with many potential areas of study. For my dissertation, I chose to focus on the function of MS ion channels and their potential application as membrane tension sensors. I first describe investigations into the role of charged pore-lining residues of the *A. thaliana* MS ion channel MSL1 and determine that rather than determining MSL1 rectification, these residues instead modulate gating kinetics.

Chapter 2: Charged Pore-lining Residues are Required for Normal Channel Kinetics in the Eukaryotic Mechanosensitive Ion Channel MSL1

Published as: A. M. Schlegel, E. S. Haswell (2020). Charged Pore-lining Residues are Required for Normal Channel Kinetics in the Eukaryotic Mechanosensitive Ion Channel MSL1. *Channels.*

2.1 Abstract

Mechanosensitive (MS) ion channels are widespread mechanisms for cellular mechanosensation that can be directly activated by increasing membrane tension. The well-studied MscS family of MS ion channels is found in bacteria, archaea, and plants. MscS-Like (MSL)1 is localized to the inner mitochondrial membrane of *Arabidopsis thaliana*, where it is required for normal mitochondrial responses to oxidative stress. Like *Escherichia coli* MscS, MSL1 has a pore-lining helix that is kinked. However, in MSL1 this kink is comprised of two charged pore-lining residues, R326 and D327. Using single channel patch-clamp electrophysiology in *E. coli*, we show that altering the size and charge of R326 and D327 leads to dramatic changes in channel kinetics. Modest changes in gating pressure were also observed while no effects on channel rectification or conductance were detected. MSL1 channel variants had differing physiological function in *E. coli* hypoosmotic shock assays, without clear correlation between function and

particular channel characteristics. Taken together, these results demonstrate that altering pore-lining residue charge and size disrupts normal channel state stability and gating transitions, and led us to propose the “sweet spot” model. In this model, the transition to the closed state is facilitated by attraction between R326 and D327 and repulsion between R326 residues of neighboring monomers. In the open state, expansion of the channel reduces inter-monomeric repulsion, rendering open state stability influenced mainly by attractive forces. This work provides insight into how unique charge-charge interactions can be combined with an otherwise conserved structural feature to help modulate MS channel function.

2.2 Introduction

Living organisms constantly experience physical force from both internal and external sources and possess a variety of mechanisms for detecting and responding to key mechanical stimuli (Fruleux et al., 2019; Persat et al., 2015; Yang et al., 2015). Among these mechanisms are mechanosensitive (MS) ion channels, which are found in all kingdoms of life (Anna Kloda & Martinac, 2001; Kung et al., 2010; Ranade et al., 2015; Eric S. Hamilton et al., 2015). Most MS channels are opened (gated) primarily by increases in lateral membrane tension (Charles D. Cox et al., 2019).

While MS ion channels are united by their primary gating stimulus rather than a common mechanosensory sequence or structure, individual MS channel families have been identified by the presence of conserved domains. One such family is the MscS family, which is defined by similarity to the *E. coli* Mechanosensitive ion channel of Small conductance (*Ec*MscS) (Malcolm & Maurer, 2012; Haswell, 2007; Pivetti et al., 2003). *Ec*MscS, along with the Mechanosensitive ion channel of Large conductance (MscL), allow *E. coli* cells to survive hypoosmotic shock. Sudden transfer into a hypotonic solution leads to water entry into the cell, subsequent swelling, and presumably an increase in lateral membrane tension. Increased membrane tension in turn opens MscS and MscL, allowing for rapid osmoregulation and preventing cell damage (Boer et al., 2011a; Rojas et al., 2014; Bialecka-Fornal et al., 2015; Buda et al., 2016; Levina, 1999).

Multiple structures of *Ec*MscS describe a homoheptameric channel with a transmembrane (TM) domain, comprised of three TM helices per monomer, atop a large cytoplasmic “cage” (Bass et al., 2002; Lai et al., 2013; Pliotas et al., 2015; Rasmussen et

al., 2019; Reddy et al., 2019; Steinbacher et al., 2007; Wang et al., 2008). A key feature of the *Ec*MscS structure is the pore-lining TM helix, TM3, which, in the nonconducting state, kinks mid-way through at G113, such that its C-terminal portion points outward from the pore and lies parallel to the lipid bilayer (Bass et al., 2002; Lai et al., 2013; Rasmussen et al., 2019; Reddy et al., 2019). During gating, TM3 is proposed to pivot outward around and partially straighten this kink, thus removing pore occlusions and allowing for ion flow (Lai et al., 2013; Pliotas et al., 2015; Vásquez et al., 2008; Wang et al., 2008). Mutations to either G113 or neighboring Q112 alter channel characteristics such as desensitization/inactivation and entry into subconducting states (Akitake et al., 2007; Edwards et al., 2008), highlighting the importance of this structural feature in shaping channel behavior.

Based on homology to the pore-lining domain and top portion of the cytoplasmic domain of *Ec*MscS, MscS family members have been found throughout the bacterial and archaeal kingdoms, in all currently available plant genomes, and in some protist genomes (Basu & Haswell, 2017). The genome of the model flowering plant *Arabidopsis thaliana* encodes ten homologs of *Ec*MscS, termed MscS-Like (MSL) channels (Haswell, 2007). MSLs localize to various compartments, including the plasma membrane (E. S. Hamilton et al., 2015; Haswell et al., 2008), chloroplast membrane (Haswell & Meyerowitz, 2006), and inner mitochondrial membrane (C. P. Lee et al., 2016). Mechanosensitive channel activity has been demonstrated in heterologous systems for MSL1, MSL8, and MSL10 (C. P. Lee et al., 2016; Eric S. Hamilton & Haswell, 2017; G. Maksaev & Haswell, 2012) and in native membranes for MSL8 and MSL10 (E. S. Hamilton et al., 2015; Haswell et

al., 2008). MSL2/3 and MSL8 are involved in osmoregulation of chloroplasts and pollen, respectively (Veley et al., 2012; E. S. Hamilton et al., 2015; Eric S. Hamilton & Haswell, 2017), much like *Ec*MscS in *E. coli* cells. However, MSL10 has a cell-death signaling activity that is separable from its MS channel activity (Veley et al., 2014; Grigory Maksaev et al., 2018), revealing MSL function beyond maintaining osmotic homeostasis.

MSL1 is localized to the inner membrane of mitochondria and appears to be involved in regulating the redox status of mitochondria during stress (C. P. Lee et al., 2016). Of all the Arabidopsis MSLs, it most closely resembles *Ec*MscS in overall structure, channel behavior, and sequence. Structural and biochemical analyses of MSL1 revealed a homoheptameric channel consisting of a TM domain, comprised of 5 TM helices per monomer, atop a large cage region likely to be located in the mitochondrial matrix (Deng et al., 2020; Y. Li et al., 2020; C. P. Lee et al., 2016). MSL1 and *Ec*MscS are both slightly anion preferring and have average conductances of ~1.2 nS at negative membrane potentials (S. Sukharev, 2002; Edwards et al., 2008; C. P. Lee et al., 2016). However, compared to *Ec*MscS, MSL1 shows both stronger rectification (a directional preference for ion flow) and hysteresis (a difference in open and closing tensions), with a preference for transporting anions out of the cell, and with channel closure often occurring at lower membrane tension than channel opening (Anishkin et al., 2010; Belyy et al., 2010; Sukharev et al., 2007). A sequence alignment (Figure 2.1A) revealed strong conservation between the pore-lining helices of MSL1 and *Ec*MscS with a singular exception: two neighboring residues are charged in MSL1 (R326 and D327) and polar in *Ec*MscS (Q112 and G113) (red box, Figure 2.1A).

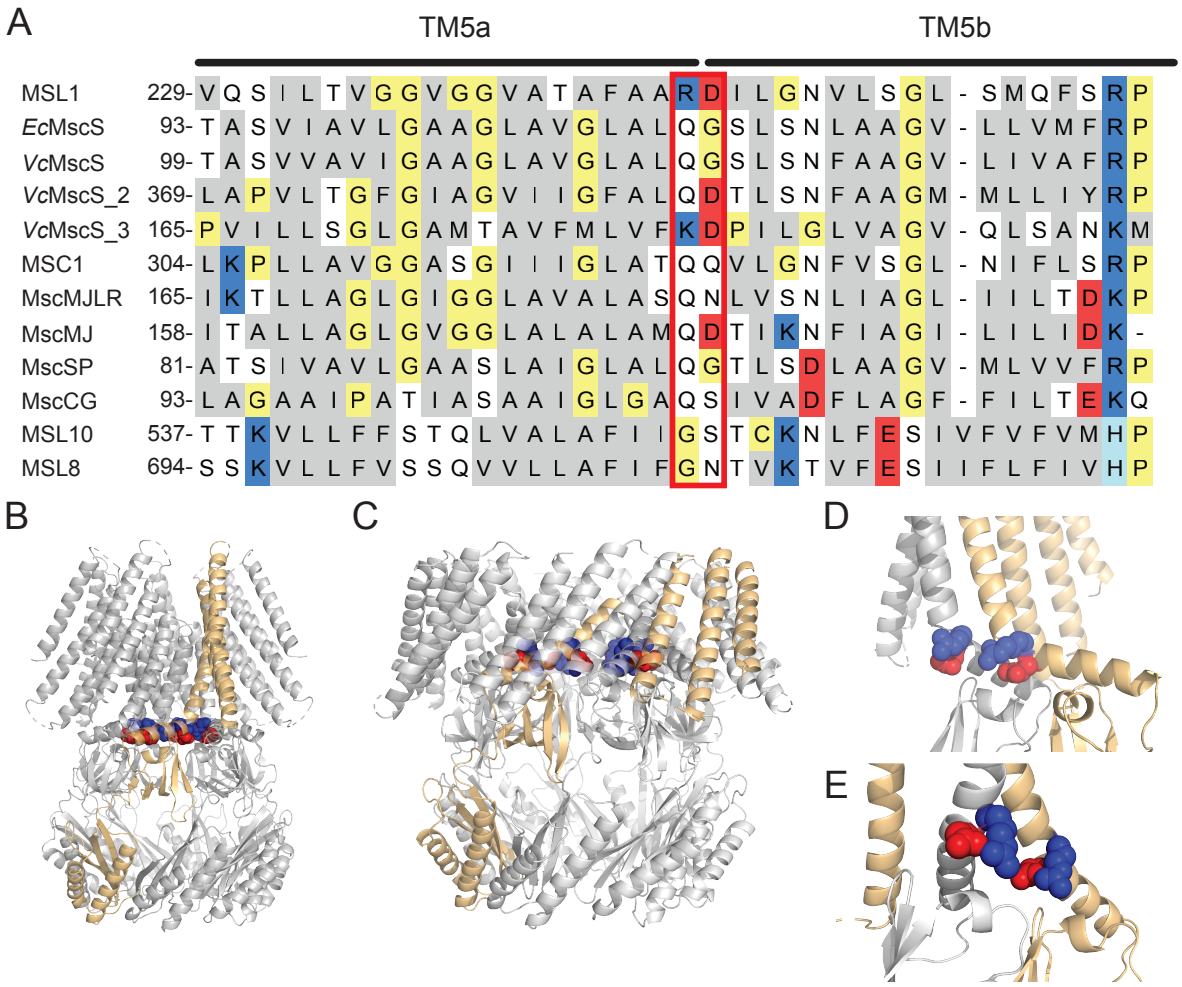

Figure 2.1. R326 and D327 are charged residues in the kinked pore-lining TM5 helix of the MS ion channel MSL1. (A) Alignment of pore-lining helices from MscS family members for which rectification information is available. Non-polar residues are gray, polar residues white, positively charged residues blue, negatively charged residues red, and other residues pale yellow. R326 and D327 of MSL1 and the corresponding residues in other MscS family members are highlighted by a red box. (B-E) Images of cryoEM structures of MSL1 (PDB file 6VXM (Deng et al., 2020)) and MSL1^{A320V} (PDF file 6VXN (Deng et al., 2020)) in closed and open states, respectively. One monomer is light orange and residues R326 (blue) and D327 (red) are indicated. (B, C) Side view of the placement of R326 and D327 in the TM5 kink of MSL1 (B) and MSL1^{A320V} (C) multimers, respectively. (D, E) Close-up view of the R326 and D327 residues in two adjacent monomers, one grey and one light orange, as viewed from inside the MSL1 (D) and MSL1^{A320V} (E) pores.

Rectification of MSL1 is also strong compared to other MscS family members for which this feature has been characterized (C. P. Lee et al., 2016) and most closely resembles that of MscS-like activity detected in *V. cholerae* cells (Rowe et al., 2013). One of three MscS-like genes from *V. cholerae* also encodes a positively charged and a negatively charged residue at the same position as R326 and D327 (Figure 1A). With the exception of MSC1 from *Chlamydomonas reinhardtii* chloroplasts and MscMJ from *Methanocaldococcus jannaschi*, (Kloda & Martinac, 2001; Nakayama et al., 2007), other MscS family members from archaea, bacteria, and plants show only mild rectification (A Kloda & Martinac, 2001; Yoshitaka Nakayama et al., 2013; Petrov et al., 2013; Edwards et al., 2008; E. S. Hamilton et al., 2015; G. Maksaev & Haswell, 2012). While the correlation between charged residues and rectification in the MscS family is not strict, charged residues have been demonstrated to control rectification in other channels (Li et al., 2008).

Recently reported cryoEM structures of MSL1 in the closed state (Deng et al., 2020; Li et al., 2020) place R326 and D327 at the kink of the pore-lining helix TM5, which is bent such that its C-terminal half runs parallel to the bilayer (Figure 2.1B), similar to TM3 in the non-conducting state of *Ec*MscS. In the MSL1^{A320V} structure, proposed to represent the open state (Deng et al., 2020), TM5 is almost completely straight and sits diagonally within the bilayer (Figure 2.1C). These structures support a gating transition in which neighboring R326 and D327 side chains point inward from the TM5 kink in the closed state (Figure 2.1D), then are pushed towards each other and away from the pore during opening (Figure 2.1E). TM5 helices from neighboring monomers also move farther

apart during channel opening. As with Q112 and G113 of *Ec*MscS (Akitake et al., 2007; Edwards et al., 2008), altering R326 and D327 of MSL1 may affect kink formation and thus channel behavior.

In this study, we investigated the roles of R326 and D327 in MSL1 rectification and other hallmarks of MSL1 channel behavior using single-channel patch-clamp electrophysiology and physiological assays in *E. coli*. Our results provide insight into the roles of individual residues in the MSL1 pore-lining helix and validate recently published MSL1 cryoEM structures (Deng et al., 2020; Li et al., 2020). More broadly, our study contributes to the understanding of how the specific composition of common structural features, like the kinked pore-lining helix found in the MscS family, can influence properties of MS ion channels.

2.3 Materials and Methods

*Subcloning and E. coli strains***.** The MSL1 sequence lacking the putative N-terminal mitochondrial transit peptide sequence (residues 1-79; (C. P. Lee et al., 2016)), codon-optimized for translation in *E. coli*, was synthesized (ThermoFisher Scientific, USA) and cloned into the pET300 vector to create pET300-MSL1. A C-terminal GFP tag was then added before the stop codon of MSL1 with an EcoRI cut site as the linker sequence between MSL1 and GFP to create pET300-MSL1-GFP. Site directed mutagenesis was then used to create pET300-MSL1^{R326Q}-GFP, pET300-MSL1^{D327G}-GFP, pET300-MSL1$^{R326Q\ D327G}$-GFP, pET300-MSL1^{D327N}-GFP, and pET300-MSL1$^{R326Q\ D327N}$-GFP (primer sequences in Table S1). Mutations were verified using restriction enzyme digest and sequencing; the R326Q mutation causes the loss of a PmlI site, the D327G mutation creates an EcoRI site, and the D327N mutation creates a SspI site. To create pET300-MscS-GFP, the MSL1 sequence was replaced with the full-length *Ec*MscS sequence. Lysogenization of *E. coli* strains FRAG-1 (Epstein & Kim, 1971), MJF465 (Levina, 1999), MJF641, and MJF516 (Edwards et al., 2012) was performed using the Novagen λDE3 Lysogenization Kit (Millipore Sigma) following manufacturer's instructions. Lysogenized strains used in this study are indicated by (DE3).

*Sequence alignment and functional predictions***.** The MSL1 cryoEM structures (RCSB Protein Data Bank, PDB ID 6VXM (Deng et al., 2020) and 6LYP (Li et al., 2020)) were visualized and images generated using PyMol (Schrödinger, Inc.). MscS family member protein sequences were obtained from publicly available data bases with

accession numbers as follows: *Escherichia coli* MscS (*Ec*MscS), UniProt ID P0C0S2; *Arabidopsis thaliana* MSL1 (MSL1), At4g00290; *Arabidopsis thaliana* MSL8 (MSL8), At2g17010; *Arabidopsis thaliana* MSL10 (MSL10), At5g12080; *Corynebacterium glutamicum* MscCG, RefSeq WP_011014245.1; *Chlamydomonas reinhardtii* MSC1, GenBank ID AB288852.1; *Silicibacter pomeroyi* MscSP, UniProt ID Q5LMR6; *Methanococcus jannaschii* MscMJ, UniProt ID Q6M0K6; *M. jannaschii* MscMJLR, UniProt ID Q58543. Structural features of sequences were either assigned based on previously published structural data or, when none was available, predicted using the TMHMM server, v 2.0 (DTU HealthTech). Sequences of 70 amino acids containing predicted or known pore-lining sequences were then aligned in Unipro UGENE software using the built-in MUSCLE algorithm.

MSL1 variant expression and localization in E. coli**.** Approximately 10 colonies of MJF465(DE3) cells expressing GFP-tagged MSL1 variants were placed into a 14 mL culture tube with 3 mL LB + 1 mM carbenicillin and shaken at 37°C, 250 rpm to an OD_{600} of ~0.5. 2 mL of this culture was added to 100 mL LB + 1 mM carbenicillin and shaken at 37°C, 250 rpm until OD_{600} ~0.5. Isopropyl β-D-1-thiogalactopyranoside (IPTG) was then added to a final concentration of 1 mM and cultures shaken at 37°C, 250 rpm for either 30 min (for expression of MscS-GFP and GFP) or 1 hour (for expression of untagged MSL1 and GFP-tagged MSL1 variants). To image GFP signal, cells were placed on a 1% agarose pad, covered with a coverslip, then imaged using an Olympus FV3000 confocal microscope. GFP was excited using a 488 nm laser and GFP emission was collected from 493-533 nm. For images of cells expressing cytoplasmic GFP, laser transmissivity

was 5% and PMT voltage was 436 V. For cells expressing either a GFP-tagged MSL1 variant or MscS-GFP, laser transmissivity was set at 6% and PMT voltage was 515 V. Both bright field and GFP fluorescence images were taken for each sample.

*Patch-clamp electrophysiology***.** Giant *E. coli* spheroplasts were made according to (Schlegel & Haswell, 2020). The MJF641(DE3) strain was used for conductance analysis, MJF516(DE3) cells for tension sensitivity measurements, and either MJF641(DE3) or MJF516(DE3) cells for open state dwell time measurements. Cells were transformed with the appropriate expression constructs and grown overnight on LB plates containing 1 mM carbenicillin at 37°C. Cells were then cultured in LB with 1 mM carbenicillin at 37°C, 250 rpm to an OD_{600} of 0.4-0.5, then diluted 1:10 in 30 mL LB + 60 µg/mL cephalexin (without carbenicillin) and shaken at 42°C, 180 rpm until cells reached ~75-100 µm in length. IPTG was added to each culture to a final concentration of 1 mM and cultures shaken at 42°C, 180 rpm for 1 hour. Cultures were incubated at 4°C overnight, then spun down at 3000 xg. Cell pellets were gently resuspended in 2.5 mL 0.8 M sucrose and the following spheroplast reaction components added in order to the resuspension, with gentle swirling after each addition: 150 µL 1 M Tris-HCl (pH 7.2), 120 µL 5 mg/mL lysozyme, 50 µL 5 mg/mL DNase I, 150 µL 0.125 M EDTA. The reaction was incubated at room temperature for 5-7 min, then stopped by adding 1 mL stop solution (0.68 M sucrose, 19 mM $MgCl_2$, 9.5 mM Tris-HCl pH 7.2, 0.22 µm filter-sterilized) and swirling to mix. 3.5 mL dilution solution (0.78 M sucrose, 1 mM $MgCl_2$, 1 mM Tris-HCl pH 7.2, 0.22 µm filter-sterilized) was added, and 275 µL aliquots stored at -80°C.

All data were collected from inside-out configuration patches. The pipette buffer used was 200 mM KCl, 90 mM $MgCl_2$, 5 mM $CaCl_2$, 5 mM HEPES, pH 7.4. The bath buffer was identical to the pipette buffer with the addition of 400 mM sucrose. Pressure application was controlled using an HSPC-1 pressure clamp system (ALA Scientific Instruments) and data were acquired using an Axopatch 200B amplifier and a Digidata 1440A digitizer (Molecular Devices) at 20 kHz and low-pass filtered at 5 kHz except for open state dwell time measurements, for which data was collected at 10 kHz. Data were analyzed using Clampfit 10.6 (Molecular Devices).

Conductance measurements were performed at membrane potentials ranging from -150 mV to 80 mV using 5 s symmetric pressure ramps. The largest conductance value for each gating event was taken to avoid including potential substate conductance measurements in the average conductance calculations. Conductances were then calculated using Ohm's law at membrane potentials of -120 mV, -60 mV, and 60 mV.

Tension sensitivity of MSL1 variants was assessed by determining the gating pressure of MSL1 or an MSL1 variant relative to that of endogenously expressed MscL, using 5-10 s symmetric pressure ramps at a membrane potential of -70 mV. The first gating events observed for each channel in a single trace were used and only MSL1 gating events lasting a minimum of 1 s were considered. Data were only analyzed if both MSL1 variant and MscL gating events were observed in the same trace and if no MSL1 variant gating events were observed prior to application of additional negative pressure to the patch.

Open state dwell time, closed state dwell time, and channel activity duration measurements were performed using a 2-4 s symmetric pressure ramp followed by monitoring of channel activity until 97.7 s after the start of the pressure ramp. Membrane potential was maintained at -70 mV throughout the course of this protocol. Traces were not analyzed if channel activity was detected prior to application of the pressure ramp, and open and closed state dwell times were only measured for traces in which a single gating event occurred. Open state dwell time was determined by measuring the duration of the first pressure-triggered gating event for each patch, regardless of the length of its subsequent closure. Closed state dwell time was considered the amount of time between the initial pressure-triggered gating event and a second gating event within the same trace. Instances in which either no additional gating event occurred and when the initial pressure-triggered gating event lasted until the end of the trace were noted as separate categories. The channel activity duration was defined as the length of time between the start of the first pressure-triggered gating event and the first channel closure lasting for ≥ 5 s. Results from individual traces were pooled from 7-10 patches per channel to determine open and closed state dwell times and from 9-10 patches per channel to determine channel activity durations measurements. For each measurement, events were sorted into one of five bins: 0-19.99 s, 20-39.99 s, 40-59.99 s, 60-79.99 s, 80+ s, with the additional categories of “No Closure” and No Re-Opening” for closed state dwell time measurements.

E. coli *growth assay***.** Five freshly transformed MJF465(DE3) colonies were grown at 37°C, 250 rpm in LB with 1 mM carbenicillin to an OD_{600} of ~0.5. Cultures were then

diluted to an OD_{600} of 0.05 in either LB only or LB + 1 mM IPTG and three 250 µL aliquots of each dilution transferred to a clear, flat-bottom 96-well plate. This plate was then placed in an Infinite M200 Pro plate reader, then incubated at 37°C with continuous shaking and OD_{600} measurements made every 15 min for a total of 6 h. Growth assays were repeated using cells from three independent transformations.

E. coli *hypoosmotic shock survival assay***.** Assays were conducted as described in (Bartlett et al., 2004) with some modifications. Freshly transformed colonies were grown overnight at 37°C, 250 rpm in low glucose citrate-phosphate media (60 mM Na_2HPO_4, 5 mM K_2HPO_4, 7 mM citric acid, 7 mM NH_4SO_4, 0.4 mM $MgSO_4$, 3 µM thiamine, 6 µM iron) with 0.04% glucose and 1 mM carbenicillin. Overnight cultures were diluted 1:5 in citrate-phosphate media with 0.2% glucose and grown to an OD_{600} of ~0.3 at 37°C, 250 rpm. Cultures were then diluted 1:1 in citrate-phosphate media with 0.2% glucose and 1 M NaCl and grown to an OD_{600} of ~0.3, at which point expression was induced for 1 hour by the addition of 1 mM IPTG. Cultures were diluted 1:20 in either ddH_2O for shocked samples or 0.5 M NaCl citrate-phosphate buffer (60 mM Na_2HPO_4, 5 mM K_2HPO_4, 7 mM citric acid, 7 mM NH_4SO_4) for unshocked controls and shaken at 37°C, 250 rpm for 15 min. Cultures were serially diluted 1:10 six times in either ddH_2O (shocked samples) or 0.5 M NaCl citrate-phosphate buffer (unshocked controls). A 5 µL aliquot of each dilution was then spotted onto LB + carbenicillin plates and grown overnight at 30°C. The next day, the number of colonies grown from each dilution were counted and survival ratios of shocked/unshocked colonies calculated for each strain/construct combination calculated using values from dilutions producing up to 50 colonies.

2.4 Results

To begin to study the role of R326 and D327 in MSL1 function, an *E. coli* codon-optimized version of MSL1 lacking the predicted mitochondrial target sequence (2-79 aa; (C. P. Lee et al., 2016)), was fused to GFP and expressed from the T7-inducible pET300 vector. For all experiments, constructs were transformed into lysogenized *E. coli* containing IPTG-inducible T7 promoters (see Methods). Four different lysogenized *E. coli* strains were used: MJF465(DE3) (*mscS*$^{-}$ *mscK*$^{-}$ *mscL*$^{-}$ (Levina, 1999)), MJF516(DE3) (*mscS*$^{-}$ *mscK*$^{-}$ *ybiO*$^{-}$ *yjeP*$^{-}$ (Edwards et al., 2012)), MJF641(DE3) (*mscS*$^{-}$ *mscK*$^{-}$ *ybdG*-*ybiO*$^{-}$ *yjeP*$^{-}$ *ynaI*$^{-}$ *mscL*$^{-}$ (Edwards et al., 2012)), and their parental strain FRAG-1(DE3) (Epstein & Kim, 1971).

GFP-tagged MSL1 variants localize to the periphery of E. coli *cells and do not strongly affect cell growth***.** We assessed the expression and localization of GFP-tagged MSL1 variants in *E. coli* strain MJF465(DE3) cells by imaging induced cells using a confocal microscope (Figure 2.2A). All versions of GFP-tagged MSL1 produced punctate GFP signal around the cell periphery that was similar to *Ec*MscS-GFP (as previously observed (Romantsov et al., 2010; van den Berg et al., 2016)), and distinct from cytoplasmic free GFP. Growth rates of all strains showed only minor differences (Figure 2.2B-C) (Okada et al., 2002).

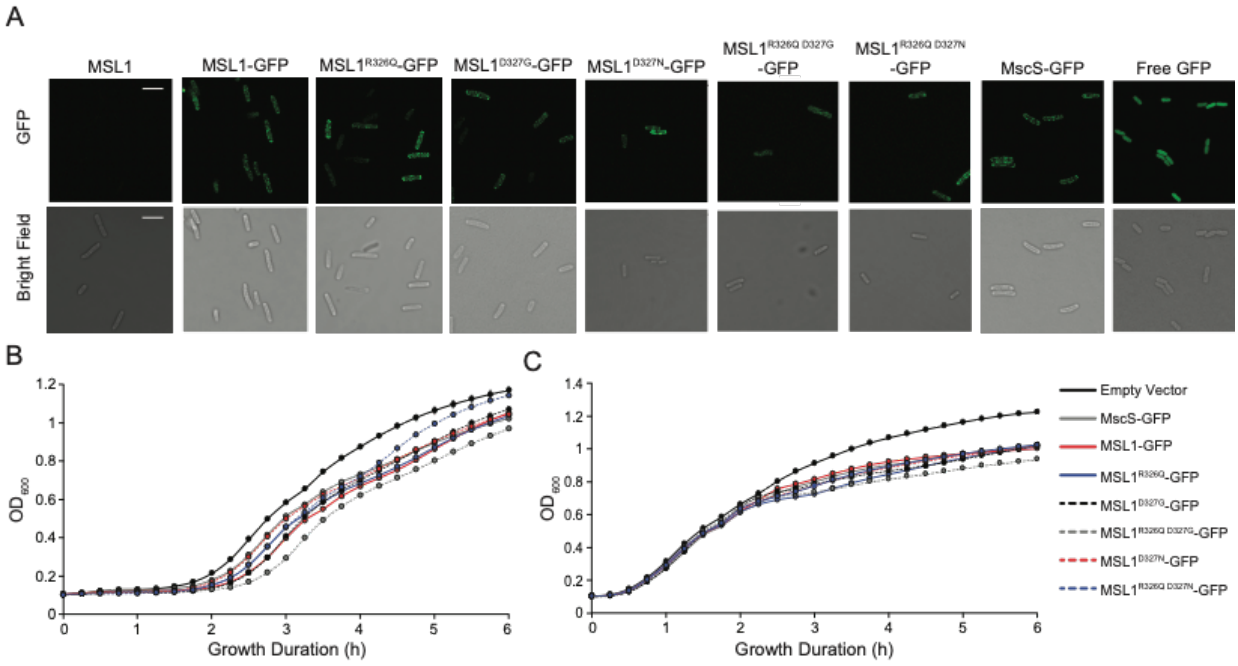

Figure 2.2. MSL1 variants localize to *E. coli* cell membranes and do not impact *E. coli* cell growth in LB. (A) Confocal micrographs of MJF465(DE3) cells expressing untagged MSL1, MSL1-GFP, a GFP-tagged MSL1 variant, MscS-GFP, or cytoplasmic GFP. Scale bars are 5 μm. (B-C) Growth curves of MJF465(DE3) cells transformed with pET300 vectors encoding the indicated protein or an empty pET21b(+) control. Cells were grown in LB with (B) or without (C) IPTG and OD_{600} values measured every 15 min. Data points are shown ± standard deviation, although error bars may be too small to be visible.

Mutations to R326 and D327 do not alter channel conductance or rectification. We next sought to characterize the channel behavior of MSL1-GFP variants using single-channel patch-clamp electrophysiology in giant *E. coli* spheroplasts as in (Schlegel and Haswell, 2020). IV curves with membrane potentials ranging from -150 mV to 80 mV for each GFP-tagged MSL1 variant are shown in Figure 2.3. As demonstrated previously (C. P. Lee et al., 2016), MSL1-GFP channel activity was triggered by application of suction to inside-out excised patches and was characterized by a single-channel conductance of ~1.2 nS at negative membrane potentials and markedly reduced

conductance at membrane potentials greater than 20 mV. No major differences were observed between the IV curves of MSL1-GFP and any GFP-tagged MSL1 variant. Thus, none of the mutations to R326 nor D327 we tested changed the rectification behavior of MSL1.

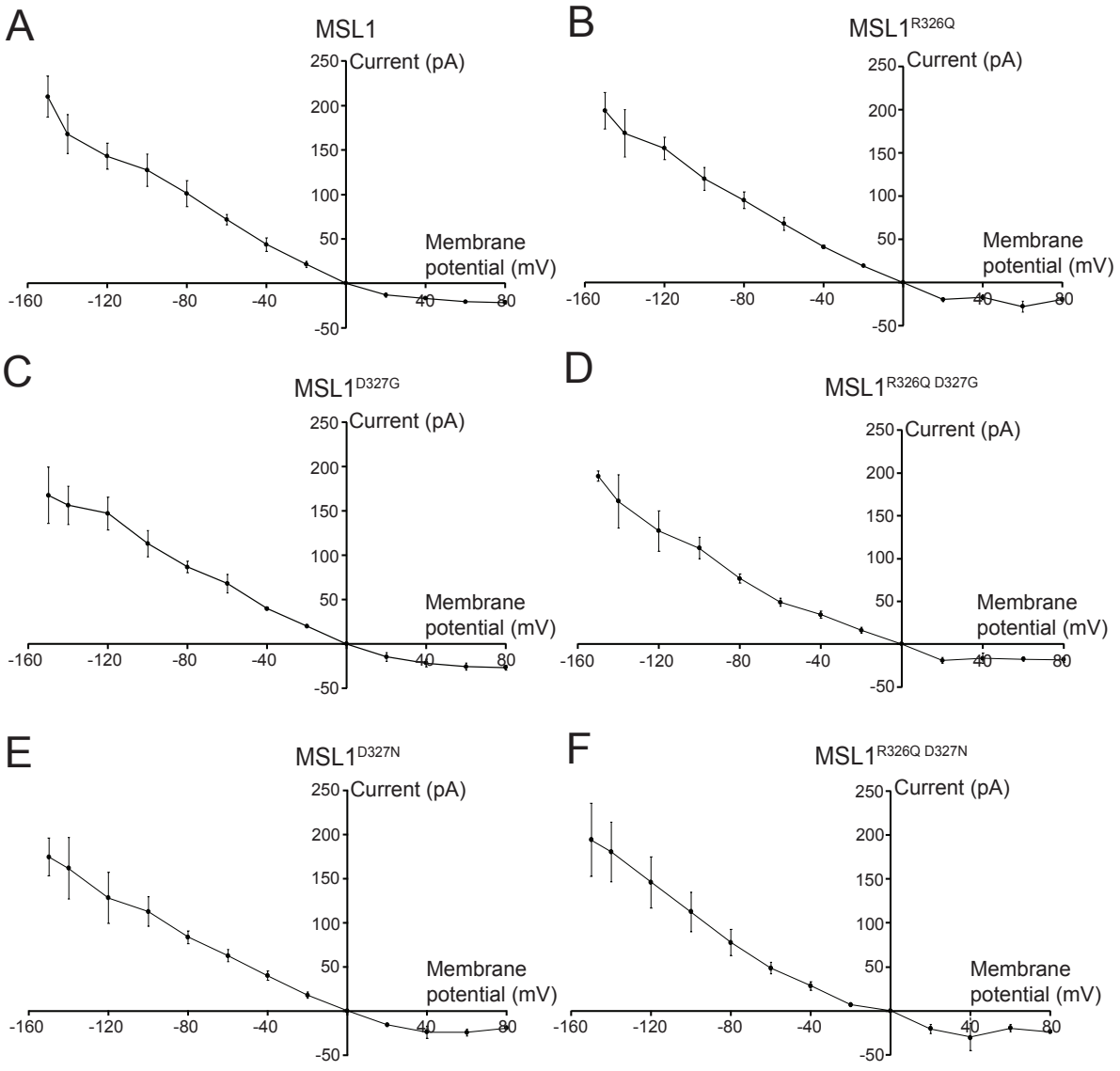

Figure 2.3. Mutations to R326 and D327 of MSL1 do not affect rectification. IV curves for GFP-tagged MSL1 variants expressed in MJF641(DE3) cells. Each data point represents the average single-channel current for 3 to 17 patches. Error bars indicate standard deviation.

The IV curves shown in Figure 2.3 were used to calculate conductance at 60 mV, -60 mV, and -120 mV for each GFP-tagged MSL1 variant (Table 2.1). The single-channel conductances of MSL1$^{R326Q\ D327G}$-GFP and MSL1$^{R326Q\ D327N}$-GFP were significantly lower than that of MSL1-GFP at -60 mV (0.82±0.08 nS, 0.81±0.11 nS, and 1.19±0.10 nS, respectively). However, no significant differences in conductance between any variants were detected at 60 mV nor -120 mV. Conductances at -120 mV are the most physiologically relevant, as plant mitochondria maintain very negative inner membrane potentials (Gerencser et al., 2012; Schwarzländer et al., 2012). We also note that in 2, MSL1$^{R326Q\ D327G}$ showed reduced single channel current but greater total current than MSL1. While this was interpreted to a higher number of channels open, this could also be due to longer open state dwell times, as described below. Taken together, the data shown in Figure 2, Figure 3, and Table 1 indicate that the size and charge at 326 and 327 are not critical for protein stability, localization, or single channel conductance. Unexpectedly, changing R326 and D327 to the analogous resides in *Ec*MscS did not reduce MSL1 rectification (Figure 3).

MSL1 Variant	**Conductance (nS)**		
	-120 mV	**-60 mV**	**60 mV**
MSL1-GFP	1.19 ± 0.12[a]	1.19 ± 0.10[a]	0.34 ± 0.02[a]
MSL1^{R326Q}-GFP	1.29 ± 0.11[a]	1.13 ± 0.12[a]	0.46 ± 0.11[a]
MSL1^{D327G}	1.22 ± 0.15[a]	1.14 ± 0.17[a]	0.42 ± 0.06[a]

MSL1$^{R326Q\ D327G}$	1.10 ± 0.20^{a}	0.82 ± 0.08^{bc}	0.29 ± 0.04^{a}
MSL1^{D327N}	1.07 ± 0.24^{a}	1.04 ± 0.12^{ab}	0.41 ± 0.07^{a}
MSL1$^{R326Q\ D327N}$	1.22 ± 0.24^{a}	0.81 ± 0.11^{c}	0.33 ± 0.07^{a}

Table 2.1. Mutations to R326 and D327 in MSL1 have little effect on channel conductance. Conductance values represent the mean of average patch conductances for 3-7 patches per variant. Differences were statistically evaluated using one-way ANOVA with post-hoc Scheffe's test; letters indicate statistical differences ($p < 0.05$).

Mutations to R326 and D327 have modest effects on MSL1 tension sensitivity. Given that R326 and D327 did not affect rectification, we next wanted to examine their role in the gating process of MSL1. We started by determining the gating pressure of each MSL1-GFP variant. Gating pressure is a proxy for tension sensitivity; for MS channels in *E. coli* it is often measured relative to endogenously expressed MscL and reported as the pressure threshold ratio (P_x/P_L) (Blount et al., 1996). We expressed each GFP-tagged MSL1 variant in *E. coli* strain MJF516(DE3) (Edwards et al., 2012) and generated giant spheroplasts. Using 5-10 s pressure ramps, we measured gating pressures of the first channel openings of each GFP-tagged MSL1 variant and of MscL, and calculated the P_x/P_L values for each variant (Figure 2.4). MSL1$^{R326Q\ D327G}$-GFP, MSL1^{D327N}-GFP, and MSL1$^{R326Q\ D327N}$-GFP had significantly higher P_x/P_L than MSL1-GFP (0.65-0.71 compared to 0.49, respectively). In contrast, pressure threshold ratios of MSL1^{R326Q}-GFP, MSL1^{D327G}-GFP, and MSL1-GFP could not be statistically distinguished, although the average P_x/P_L of individual patches containing MSL1^{D327G}-GFP were typically lower than those of MSL1-GFP. These results thus indicate that both size and

charge at the MSL1 TM5 kink influence gating pressure, and that the residue at 327 appears to play a dominant role.

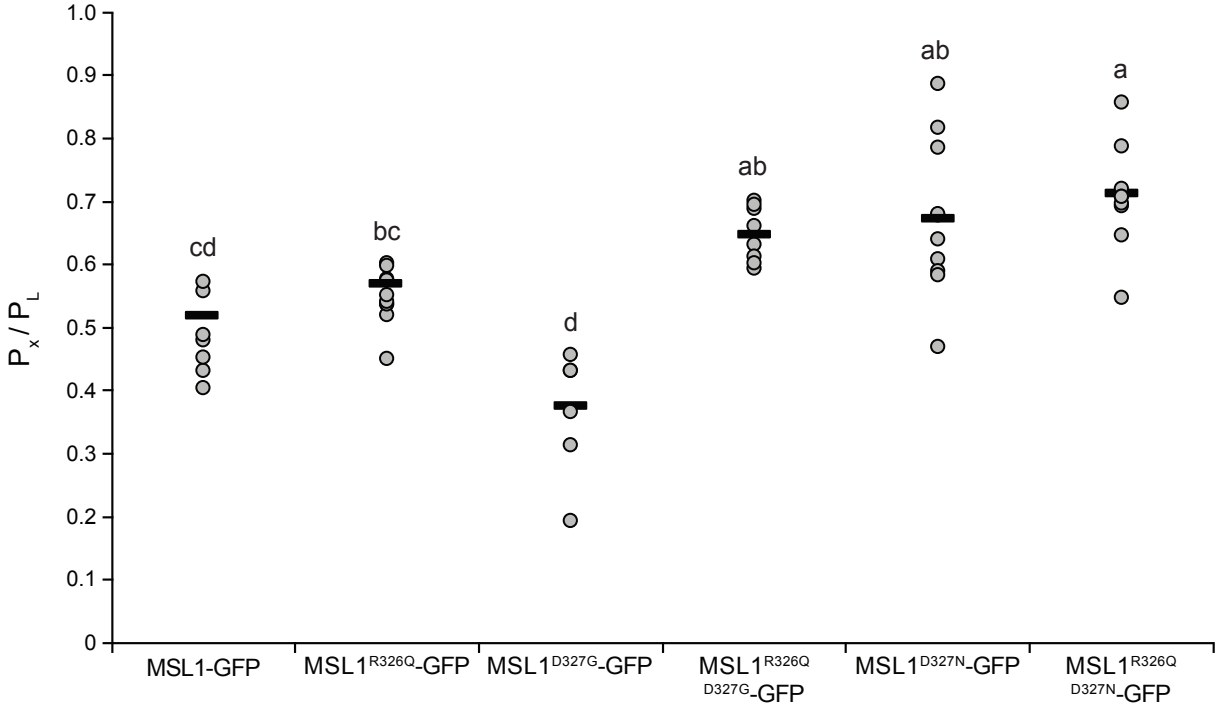

Figure 2.4. MSL1$^{R326Q\ D327G}$-GFP, MSL1^{D327N}-GFP, and MSL1$^{R326Q\ D327N}$-GFP have significantly higher gating pressures than MSL1-GFP. Gating pressures of the indicated GFP-tagged MSL1 variants relative to the gating pressures of endogenously expressed MscL. Channels were gated using 5-10 s symmetric pressure ramps at a membrane potential of -70 mV. Each gray circle represents the average of all gating pressure ratios obtained for a single patch, while the black bars represent the mean of patch averages for each sample. N = 6-10 patches per variant. Statistical differences are indicated by different letters and were determined using one-way ANOVA followed by Scheffe's post-hoc test; $p < 0.05$). Data points greater than two standard deviations beyond the sample average were excluded.

R326 and D327 exert dramatic and opposing effects on channel kinetics. We also examined the channel activity duration, a parameter we previously referred to as open state dwell time (Deng et al., 2020), open state dwell time, and closed state dwell time of GFP-tagged MSL1 variants (Figure 2.5). These measurements allowed us to

analyze the gating kinetics of our MSL1 variants without achieving patch saturation, as low expression of our GFP-tagged MSL1 variants produce low numbers of channels per patch, as seen previously (Deng et al., 2020). As in (Deng et al., 2020), we used a modified version of a previously published protocol (Akitake et al., 2007). Mechanosensitive gating was triggered by applying a brief 2-4 s negative pressure ramp at a membrane potential of -70 mV, then this membrane potential was maintained without any additional suction for a total of 100 s.

Channel activity duration was defined as the time from the initial pressure-triggered channel opening to final channel closure, as indicated by the complete cessation of channel activity for 5 s. Using this protocol, most (89%) MSL1-GFP activity lasted less than 20 s and only 5.5% of activities lasted more than 80 s (Figure 2.5A). Similarly, no MSL1^{R326Q}-GFP activity lasted longer than 20 s. In contrast, large proportions of MSL1^{D327G}-GFP and MSL1^{D327N}-GFP activities lasted for more than 80 s (62.5% and 72.9%, respectively) before final closure. Adding the R326Q mutation to these channels reduced the occurrence of extended activity to 48.4% and 42.1% of traces for MSL1$^{R326Q\ D327G}$-GFP and MSL1$^{R326Q\ D327N}$-GFP, respectively.

Open state dwell time was defined as the length of the initial pressure-gated channel opening before closure of any duration, as in (Malcolm & Blount, 2015; Edwards et al., 2008). As shown in Figure 2.5B, the open state dwell time of MSL1-GFP was almost always (97% of the time) less than 20 s. However, we observed that MSL1^{D327N}-GFP and MSL1$^{R326Q\ D327N}$-GFP open states often persisted for much longer, in many cases (61.9% and 30.7%, respectively) remaining open until the end of the trace. MSL1^{D327G}-GFP and

MSL1$^{R326Q\ D327G}$-GFP also occasionally exhibited long open state dwell times (19% and 10.6%, respectively).

Closed state dwell time was defined as the time between the closure of the first pressure-gated channel and the second opening event. MSL1-GFP gating events had relatively short closed state dwell times, with most traces (74.6%) showing a second opening event within 20 s (Figure 2.5C). For MSL1^{R327Q}-GFP most (59.6%) channel closing events were never followed by a second opening. On the other hand, almost all (85.7%) MSL1^{D327G}-GFP events had the shortest closed state dwell times, as did MSL1$^{R326Q\ D327G}$-GFP (70.2%). MSL1^{D327N}-GFP and MSL1$^{R326Q\ D327N}$-GFP frequently (61.9% and 30.7%, respectively) did not close at all during the assay.

To summarize, reducing the size and positive charge of the amino acid at position 326 decreased channel activity duration and open state dwell time while increasing closed state dwell time. Reducing the size and negative charge of the amino acid at position 327 caused the opposite effect, increasing channel activity duration and open state dwell time, and decreasing closed state dwell time. Finally, both double mutants showed intermediate phenotypes, suggesting that R326 and D327 in TM5 of MSL1 have opposite effects on closure efficiency.

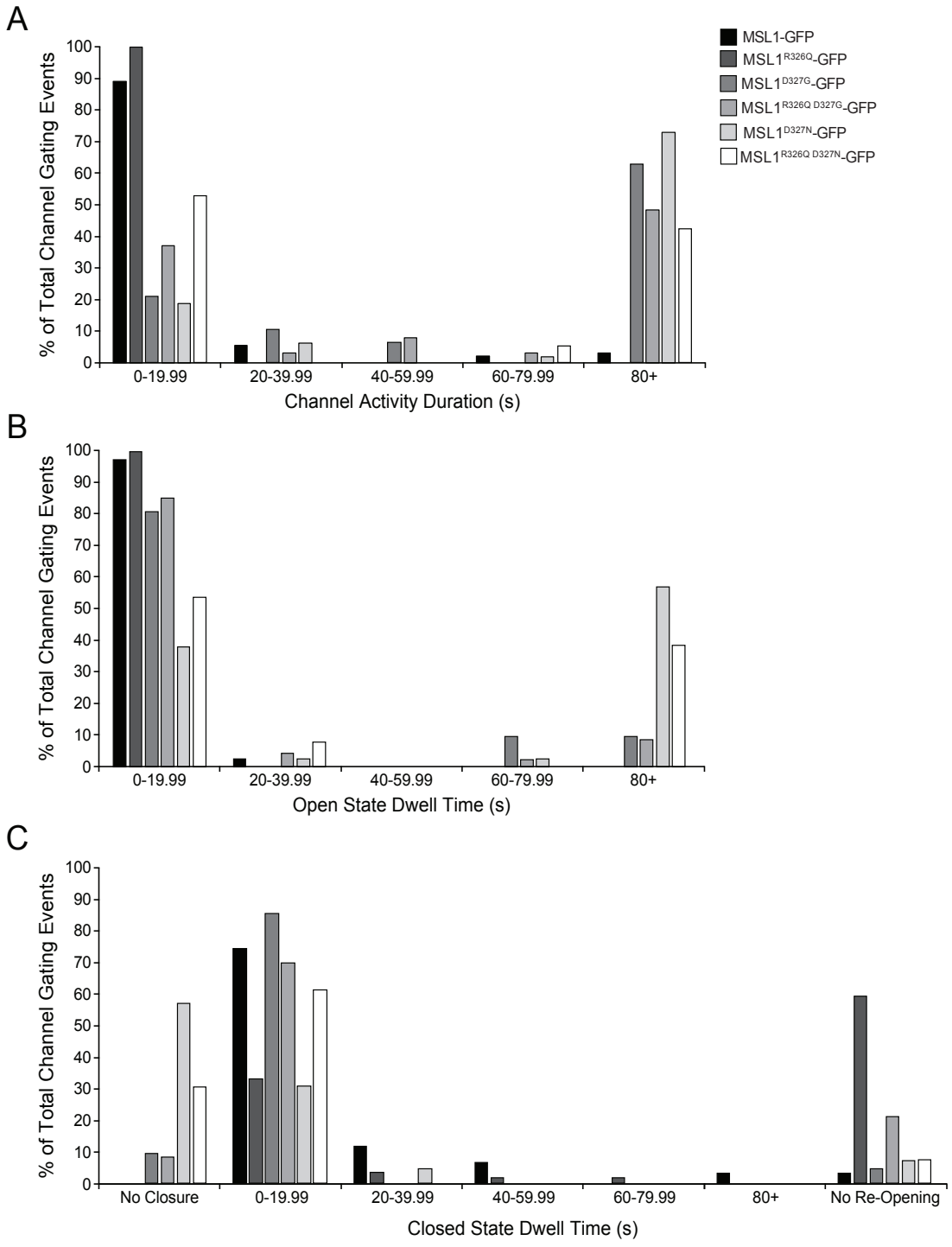

Figure 2.5. Effect of R326 and D327 mutations on the channel kinetics of MSL1-GFP variants. Membrane potential was maintained at -70 mV and channel gating was triggered by either a 2 s or 4 s symmetric pressure ramp followed by monitoring of channel activity without additional pressure until 97.7

s. (A) Channel activity duration, defined as the time from pressure-triggered gating to ≥ 5 s of channel closure. (B) Open state dwell time of initial pressure-triggered gating events. (C) Closed state dwell time, defined as the time from closure of the initial pressure-triggered gating event to the first subsequent gating event. Results from 19-97 traces from 9-10 patches (A) and 13-59 traces from 7-10 patches (B, C) per variant are shown.

Some MSL1 variants have unstable open states. Individual traces (Figure 2.6) at both -60 mV and -120 mV showed generally stable open states for MSL1-GFP, MSL1^{R326Q}-GFP, and MSL1^{D327N}-GFP. However, MSL1$^{R326Q\ D327G}$-GFP, MSL1$^{R326Q\ D327N}$-GFP, and MSL1^{D327G}-GFP were flickery (Figure 2.6). Flickery channel behavior is produced by rapid transitions between nonconducting, conducting, and subconducting states, and is thought to be indicative of an unstable open state (Malcolm & Blount, 2015; Rasmussen et al., 2007). Thus, both the size and charge of residues at 326 and 327 are important to the stability of the MSL1 open state.

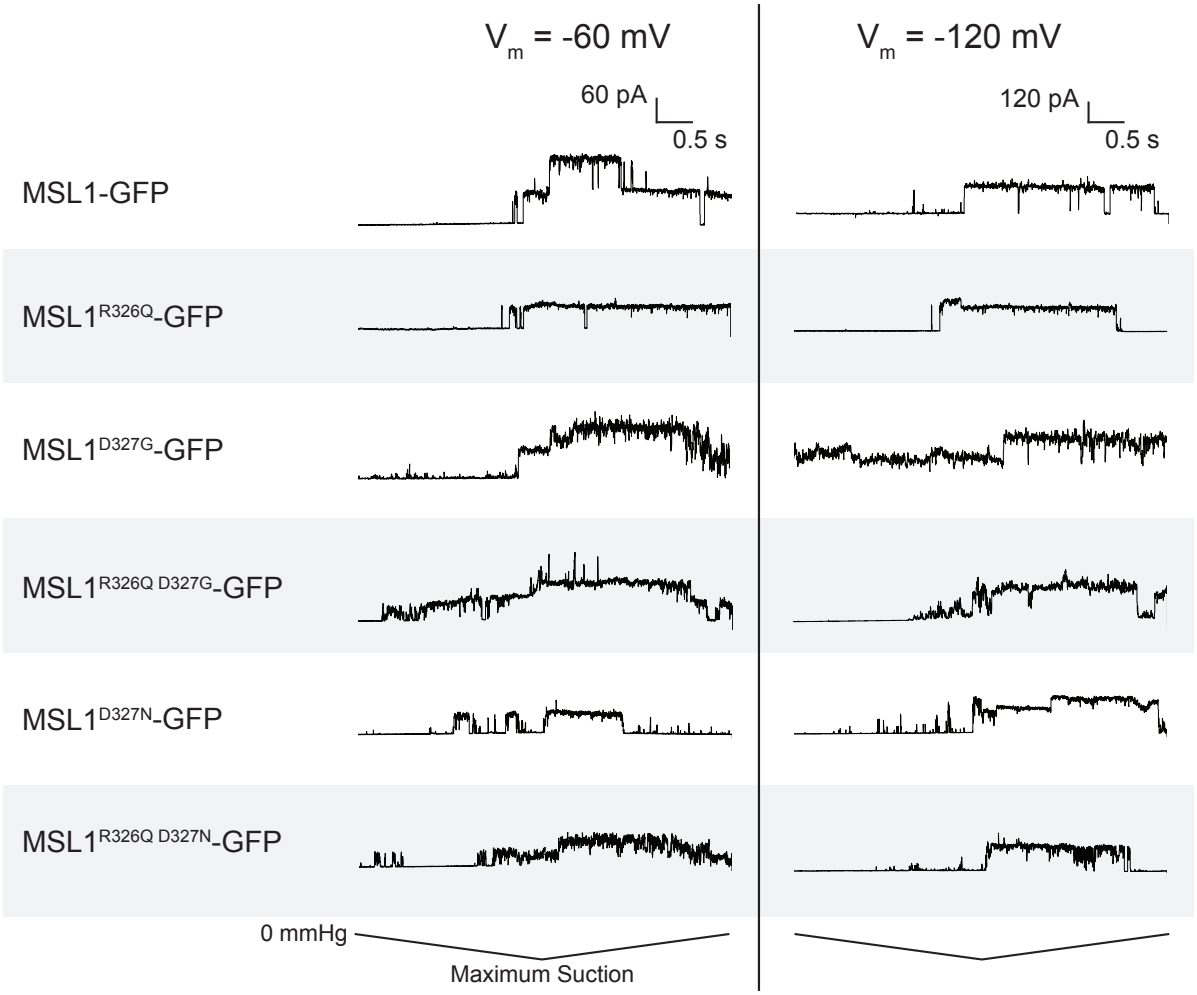

Figure 2.6. R326 and D327 influence open state stability of MSL1. Representative traces from inside-out excised patches showing pressure-activated gating events of MJF641(DE3) cells expressing the indicated constructs at two membrane potentials. Traces show current measurements taken during a 5 s symmetric negative pressure ramp, with the maximum amount of negative pressure (and therefore rate of pressure application) varying between traces.

R326 and D327 mutations alter the physiological function of MSL1 in *E. coli*.

Like *Ec*MscS, MSL1 provides protection from hypo-osmotic shock to *E. coli* (C. P. Lee et al., 2016). To determine the effects of R326 and D327 mutations on this osmoregulatory function, we examined the ability of *E. coli* MJF465(DE3) cells expressing GFP-tagged MSL1 variants to survive hypoosmotic shock. MJF465(DE3) cells lack MscS, MscL, and

MscK and therefore cannot survive severe hypoosmotic shock without expressing a functional MS ion channel (Levina, 1999). In this assay, cells are grown in high salt citrate-phosphate media, channel expression is induced, then cells are either hypoosmotically shocked in water or transferred to the same high salt media. FRAG-1(DE3) cells, which contain all endogenous MS channels, survive, while MJF465(DE3) cells do not. MSL1-GFP, MSL1^{R326Q}-GFP, and MSL1$^{R326Q\ D327G}$-GFP all conferred hypoosmotic shock survival rates comparable to that of FRAG-1 cells, suggesting they all contribute to osmoregulation during hypoosmotic shock (Figure 2.7A, B). Survival rates conferred by MSL1^{D327G}-GFP expression were unusually variable and often higher for shocked cells than nonshocked cells (average survival rate of 160%, Figure 2.7A). Cells expressing MSL1^{D327N}-GFP or MSL1$^{R326Q\ D327N}$-GFP grew too slowly in citrate-phosphate media to be analyzed in this assay.

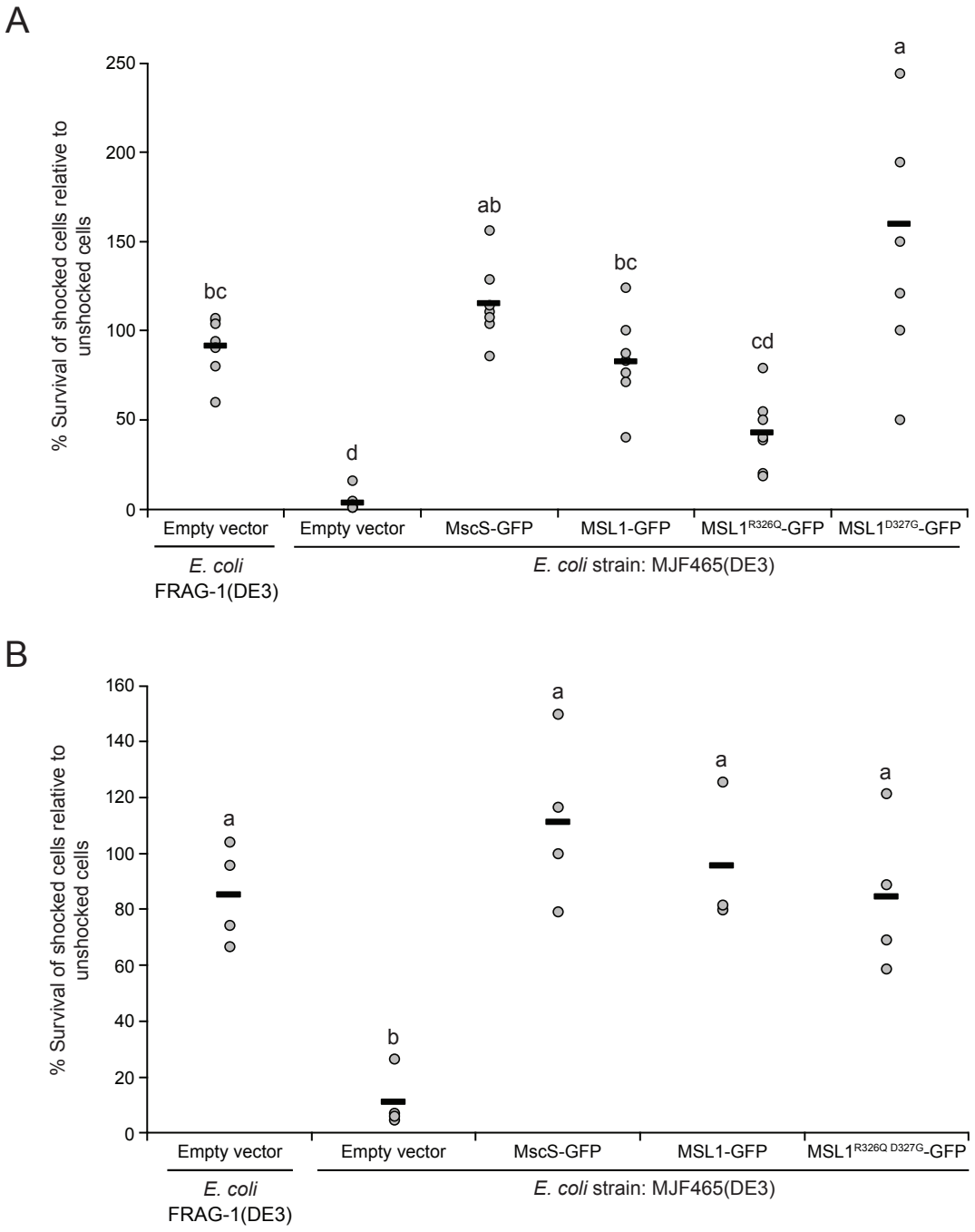

Figure 2.7. Some MSL1 variants protect *E. coli* strain MJF465(DE3) from hypoosmotic shock. Hypoosmotic shock survival rates of cells from the indicated strains relative to unshocked controls. Each circle represents the relative survival rate for an experiment and black bars indicate the average survival rate for all experiments. For each panel, statistical differences were evaluated using one-way ANOVA

followed by a post-hoc Scheffe's test; different letters indicate samples that are statistically different ($p < 0.05$). One data point greater than two standard deviations beyond the sample average was excluded.

MSL1-GFP variants thus had a variety of effects on *E. coli* physiology that may be attributed to a combination of gating pressure (Figure 2.4), channel activity duration, open and closed state dwell times (Figure 2.5), and open state stability (Figure 2.6). The reduced duration of MSL1^{R326Q}-GFP activity, and the increased gating pressure and activity duration of MSL1$^{R326Q\ D327G}$-GFP did not seem to affect their function in *E. coli* cells during hypoosmotic shock. In contrast, we observed large variations in protection by MSL1^{D327G}-GFP between experiments, perhaps due to the combination of a lower gating threshold and extended activity duration. Based on our electrophysiological analysis, it is possible that the extended open dwell times and extended durations of MSL1^{D327N}-GFP and MSL1$^{R326Q\ D327N}$-GFP activity impaired cell growth. However, as both variants had higher gating pressures than MSL1-GFP, they do not fit classic gain-of-function characteristics (Blount et al., 1997).

2.5 Discussion

The *Arabidopsis* mitochondrial MS channel MSL1 contains a notable feature midway through its pore-lining TM5 helix: a kink formed by charged residues R326 and D327. In *Ec*MscS, the pore-lining kink is proposed to play important roles in transitions between channel states (Akitake et al., 2007; Lai et al., 2013; Pliotas et al., 2015; Vásquez et al., 2008; Wang et al., 2008; Edwards et al., 2008), but the residues that comprise it are nonpolar. To determine the role played by R326 and D327 in both distinct and shared characteristics of MSL1 and *Ec*MscS, we created MSL1 variants in which the charges and size of R326 and D327 were altered, then evaluated their channel behavior and physiological function in *E. coli* Mutations to R326 and D327 affected tension sensitivity, the duration of channel activity, open and closed state dwell times, and open state stability, indicating a role in modulating MSL1 channel state stabilities and transitions, but did not affect stability, localization, conductance, nor rectification.

Based on open and closed state cryoEM structures, we have proposed that MSL1 opening is driven by membrane flattening and area expansion (Deng et al., 2020). These forces drive the outward rotation and tilting of TM5 and the straightening of the kink that joins TM5a and TM5b during the MSL1 gating transition. The data presented here, summarized in Table 2.2, suggest that the charge and size of R326 and D327 side chains are important for the stability of the open state and for gating and closing transitions. Combining these results with cryoEM structures (Deng et al., 2020; Li et al., 2020), we infer that in the closed state, charge-charge repulsion between R326 side chains on

different monomers is finely balanced by charge-charge attractions between R326 and D327 within each monomer (Figure 2.1B, D). In the open state, intra-monomeric attractive forces between R326 and D327 dominate and inter-monomeric repulsions lose strength, due to the increased distance between helices from different monomers and the shortened distance between R327 and D327 (Figure 2.1C, E). Below, we describe how our results can be explained by this “sweet spot” model.

MSL1 Variant	Conductance	Gating Pressure	Open State Stability	Channel Activity Duration
WT MSL1	-	-	Stable	-
$MSL1^{R326Q}$	WT	1.12 WT^{ns}	Stable	Short
$MSL1^{D327G}$	WT	0.75 WT^{ns}	Flickery	Very Long
$MSL1^{R326Q\ D327G}$	Low at -60 mV	1.32 WT	Slight Flicker	Long
$MSL1^{D327N}$	WT	1.39 WT	Stable	Very Long
$MSL1^{R326Q\ D327N}$	Low at -60 mV	1.45 WT	Slight Flicker	Long

Table 2.2. Summary of GFP-tagged MSL1 variant properties. Conductance and gating pressure are presented relative to MSL1-GFP measurements. ^{ns} indicates differences from WT are not statistically significant.

The most dramatic effect of the lesions we created was on channel activity duration and open dwell time. The activity of $MSL1^{D327G}$-GFP, $MSL1^{R326Q\ D327G}$-GFP, $MSL1^{D327N}$-GFP, and $MSL1^{R326Q\ D327N}$-GFP lasted far longer than that of MSL1-GFP (Figure 2.5A). All mutations to D327 caused extended channel activity durations (Figure 2.5A), and both $MSL1^{D327N}$-GFP and $MSL1^{R326Q\ D327N}$-GFP had longer open state and shorter closed state dwell times (Figure 2.5B, C). These results suggest that the charge-charge attraction between D327 and R326 facilitates closure. In contrast, $MSL1^{R326Q}$-GFP exhibited

reduced channel activity duration (Figure 2.5A). According to our sweet spot model, the R326Q mutation on its own also would suffer from a loss of charge-charge attraction, but this effect is overshadowed by the loss of repulsion between R326 on different monomers in the closed state. Combining mutations in both residues leads to a channel where both attractive and repulsive forces are lost, and the channel activity duration and open state dwell time are intermediate between the two single mutants. A seemingly counterintuitive observation is that two channels (MSL1^{D327G}-GFP and MSL1$^{R326Q\ D327G}$-GFP) have extended channel activity durations (Figure 2.5A) and are flickery (Figure 2.5, Figure 2.6). Perhaps these channels have both an unstable open state (hence the flickering) and an increased barrier to closing. Once they are stably closed, however, they stay closed until additional tension is applied.

Modest but statistically significant increases in gating pressure were observed with MSL1$^{R326Q\ D327G}$-GFP, MSL1^{D327N}-GFP, and MSL1$^{R326Q\ D327N}$-GFP (Figure 2.4). These results cannot be easily explained by the sweet spot model described above, but are reminiscent of the attractive charge-charge interactions between the transmembrane and cytoplasmic domains of *Ec*MscS (Machiyama et al., 2009; Takeshi Nomura et al., 2008). We also observed a mild decrease in the gating pressure of MSL1^{D327G}-GFP (Figure 2.4). This may arise from destabilization of the closed state due to the loss of attractive charge-charge interactions and dominance of repulsive forces. The addition of the R326Q mutation in the MSL1$^{R326Q\ D327G}$-GFP may ameliorate this closed state repulsion, reversing the effects of the D327G mutation (Figure 2.4). However, due to the subtlety of

all gating pressure changes we observed, other factors may also play a role that are beyond the scope of our model.

The results presented here establish the importance of two rings of oppositely charged neighboring residues in the channel pore in modulating channel kinetics and open state stability for the mitochondrial MS ion channel MSL1. Our data support a sweet spot model wherein attraction between oppositely charged residues on the same monomer and repulsion from identical residues on different monomers work together to facilitate opening and closing transitions as well as the stability of the closed and open states. Given their position at the pore-lining helix kink, a structural feature with demonstrated importance in *Ec*MscS gating (Akitake et al., 2007; Edwards et al., 2008), this work provides a glimpse into how the same structural features can be composed of entirely distinct residues amongst members of the same MS channel family, creating different mechanisms of control. These results provide a starting point for future investigations into the fine-tuning of MSL1 gating transition, as well as insight into the dynamic network of side chain interactions contributing to MS channel behavior.

2.6 Supplementary Information

Primer Name	Sequence	Template
R326Q_F	ATGGCCGGAGTTAGGTTATCGC	MSL1
R326Q_R	CTTCTCCCTATCAAGCCCACC	MSL1
D327G_F	CAAGAAGACGACGATGGCTGT	MSL1
D327G_R	ATATTGACCATCATACTCATTGC	MSL1
R326Q_D327G_F	GCATTTGCAGCACAGGGAATTCTGGGTAATG	$MSL1^{R326Q}$
R326Q_D327G_R	CATTACCCAGAATTCCCTGTGCTGCAAATGC	$MSL1^{R326Q}$
D327N_F	CCGCATTTGCAGCACGTAATATTCTGGGTAATG	MSL1
D327N_R	CATTACCCAGAATATTACGTGCTGCAAATGCGG	MSL1
R326Q_D327N_F	CCGCATTTGCAGCACAGAATATTCTGGGTAATG	$MSL1^{R326Q}$
R326Q_D327N_R	CATTACCCAGAATATTCTGTGCTGCAAATGCGG	$MSL1^{R326Q}$

Table S2.1. Site-directed mutagenesis primers. Primers used to generate MSL1 variants, their corresponding sequences, and the template used.

Chapter 3: Progress Towards Creation of a Genetically-Encoded Fluorescence-Based Membrane Tension Sensor

3.1 Abstract

Mechanical forces, including membrane tension, impact all living organisms and convey critical information about that organism's external and internal environments. However, currently available techniques can make quantification of membrane tension in difficult-to-access membranes, like those of walled cells, internal tissues, or organelles tricky. In addition, distinguishing between tension and other membrane characteristics, such as composition, can be difficult, as seen for the biosensor FliptR. We attempted to develop a genetically-encoded, fluorescence-based membrane tension sensor using the mechanosensitive (MS) ion channel MscS as a tension-sensitive scaffold and circularly permuted GFP (mcpGFP) as a fluorescent reporter. Insertion of mcpGFP at ten different sites throughout MscS produced stable membrane-localized proteins, of which $MscS^{S58}$-mcpGFP and $MscS^{A286}$-mcpGFP showed strong baseline GFP signal and MS channel activity. $MscS^{S58}$-mcpGFP or $MscS^{A286}$-mcpGFP were then expressed in *E. coli* cells exposed to sustained hypoosmotic shock or alternating hypo- and hyperosmotic shocks to evaluate sensor function. While the initial hypoosmotic shock produced a 20-30% drop in signal intensity, subsequent hypo- and hyperosmotic shocks produced < 10% increases and decreases in signal intensity, respectively. Point mutations known to alter

MscS function were introduced into MscS^{S58}-mcpGFP and MscS^{A286}-mcpGFP but *E. coli* cells expressing those mutants failed to exhibit dramatically changes in osmolarity-induced fluorescence intensity. Finally, signal intensity changes of a single TM helix C-terminally tagged by mcpGFP (TM1-mcpGFP) in *E. coli* cells undergoing cycling shocks were indistinguishable from those of MscS^{S58}-mcpGFP or MscS^{A286}-mcpGFP. These results suggest that MscS^{S58}-mcpGFP and MscS^{A286}-mcpGFP do not directly report membrane tension changes, but instead report changes in another cellular factor altered during osmotic shock. Our work thus provides a cautionary description of tension sensor design, demonstrating the need to ensure specificity of sensor candidates for membrane tension rather than other cellular characteristics.

3.2. Introduction

Mechanical forces in living organisms. Mechanical forces are ubiquitous sources of information and stimulation for living organisms that arise from both internal and external sources. Such information is critical for a variety of processes touching on all aspects of life, including growth and development (Eng & Sampathkumar, 2018; Hernández-Hernández et al., 2014; Persat, 2017; Vining & Mooney, 2017; F. Zhao et al., 2018), biotic and abiotic stress responses (Cheng et al., 2018; Lopez-Bellido et al., 2019; Roignant et al., 2018; Vaahtera et al., 2019), and maintenance of osmotic homeostasis (Bremer & Krämer, 2019; Hamant & Haswell, 2017). In some of these situations, mechanical force directly triggers an immediate physical response to a given stimuli. In others, mechanical force triggers signaling cascades to promote force responses.

Tools for a quantitative understanding of mechanobiology. Quantification of mechanical forces and material properties of living systems is important for a complete understanding of how mechanical forces are perceived and responded to. Techniques to measure mechanical properties of cellular components, including atomic force microscopy (AFM), optical and magnetic tweezers, micropipette suction, and micropipette needles often involve direct manipulation of a biological component or system as part of quantifying a response or material property (Brenner et al., 2011; Freikamp et al., 2017; Sen & Kumar, 2010; Siedlik et al., 2016). A subset of techniques emphasize the passive reporting of force levels during process like development,

growth, or stress responses and include genetically-encoded force sensors (Brenner et al., 2011; Freikamp et al., 2017; Iwai & Uyeda, 2008; Siedlik et al., 2016), nanoparticles (Lay et al., 2017), nanocrystals (Fischer et al., 2017), oil droplets (Campàs et al., 2014), and push-pull probes (Colom et al., 2018).

Biosensors can be either chemically-synthesized or genetically-encoded depending on their mechanism of production. Chemically-synthesized biosensors are synthesized in the lab then introduced into a living organism, cell, or tissue by processes like incubation, ingestion, or injection. One advantage of chemically-synthesized biosensors is the sheer variety of sensor types, and current force sensors include lipid droplets, chemical dyes, nanoparticles, and other nano-based structures.

Lipid droplets are fluorescent, cell-sized microdroplets with known mechanical properties (Campàs et al., 2014). These droplets can be injected between cells in a given tissue and imaged, after which the 3D shape of the droplet is reconstructed. Because the material properties of the droplet are known, a force map can then be generated that describes forces exerted by neighboring cells. Theoretically, such a method could be used on a small scale to look at forces within cells, although this would complicate the method for introducing the lipid droplet.

Another type of chemically-synthesized force biosensor are nanostructures, including up-converting nanoparticles (Lay et al., 2017, 2018). These nanoparticles consist of an $NaYF_4$ lattice into which the lanthanides Yb^{3+} and Er^{3+} and the *d*-metal Mn^{2+} have been incorporated. Upon application of either near-IR light (for upconversion)

or visible light (for photoluminescence), these nanoparticles emit light whose intensities at multiple wavelengths are dependent on the amount of force being applied to the particle, which alters the influence of Mn^{2+} on the emission spectra. These nanoparticles can report forces ranging from 100 nN to 10 μN, which are much higher magnitude forces than many other force biosensors. In addition, these nanoparticles appear non-toxic based on ingestion experiments with *C. elegans* (Lay et al., 2019), a potentially major issue for chemically synthesized biosensors.

Genetically-encoded biosensors are expressed by cells themselves and, as such, often consist of or utilize fluorescent proteins as reporters. Many genetically-encoded force biosensors are based on a biosensor published by (Meng et al., 2008). These biosensors are made by inserting a force-sensing module consisting of a FRET-pair separated by a stretchable and compressible linker into a protein of choice. Application of force to protein in which the force-sensing module is embedded changes the pressure on the linker, thus changing its length. This alters the separation distance between the FRET-pair partners, changing the FRET ratio detected during imaging. The initial sensor set utilized a rigid α-helix (Chen et al., 1995) of varying lengths as the force-sensitive linker with initial application in *C. elegans* and migrating 3T3 cells and was later calibrated to enable quantitative measurements (Meng et al., 2011). Additional variations on this sensor design have involved use of different fluorophore FRET pairs (Meng & Sachs, 2012) and linker sequences, enabling detection of forces ranging the single pN level (Grashoff et al., 2010) through tens of pN (Austen et al., 2015).

One type of mechanical force that has been particularly difficult to quantify in living organisms is lateral membrane tension. Lateral membrane tension is an intrinsic property of biological membranes and can be altered by membrane stretching or bending. There have also been multiple attempts to create membrane tension sensors, including a chemically synthesized biosensor and genetically-encoded biosensor. One of these membrane tension sensors is FliptR (Colom et al., 2018), a push-pull probe whose fluorescence lifetime, rather than intensity or wavelength, depends on the density of the lipid bilayer in which it is embedded. FliptR consists of two planar ring structures connected by a carbon-carbon bond around which they can rotate. FliptR sits in the membrane due to the presence of charged, polar regions at either end, with the spacing between individual lipid tails determining whether the planar rings sit parallel or perpendicular to each other, with each conformation possessing different fluorescence lifetimes. This means that changes in either relative levels of ordered vs disordered lipids, membrane tension, or both can alter fluorescence lifetime of FliptR, rendering it useful but with data that can be complicated to interpret.

One issue with FliptR that has recently begun to be addressed is targeting of the sensor to specific membranes. As it is not genetically-encoded, specific tags or signal peptides cannot be attached or must be synthesized. The addition of chemical groups with specific properties that allow them to accumulate in the membranes of specific organelles, including mitochondria, has had some success (Goujon et al., 2019). Such an approach is especially viable in light of work with organelle-specific dyes like tetramethyl rhodamine methyl ester (TMRM), which specifically accumulated in

Arabidopsis root mitochondria (Schwarzländer et al., 2012). However, such targeting will require empirical testing and may vary in effectiveness between cell types and conditions, depending on changes in the properties and presence of different organelles.

In addition, a genetically-encoded biosensor for membrane tension has been developed involving the force-sensing module described above is the membrane tension sensor MSS (W. Li et al., 2018). Instead of inserting a force-sensing module in a single protein, FRET-pair members are linked to lipid raft and non-lipid raft portions of the plasma membrane by Lyn and K-Ras kinases, respectively. While function of such a sensor is highly dependent on membrane composition and the kinase connectors, such a scheme could be used to make tension sensors for a variety of membranes with different membrane linkers, assuming similar basal FRET ratios to enable detection of FRET ratio changes with tension.

A MscS-based approach for building a membrane tension sensor. We attempted to create a genetically-encoded fluorescence-dependent membrane tension sensor using a tension-sensitive protein scaffold and single fluorescent protein reporter. For the tension-sensing scaffold, we chose the *E. coli* mechanosensitive channel of small conductance (MscS). MscS possesses multiple advantages as a tension-sensing scaffold. First, it is directly opened by membrane tension (Okada et al., 2002; S. Sukharev, 2002), enabling direct reporting of tension changes. Second, multiple structures have been determined by x-ray crystallography (Bass et al., 2002; Lai et al., 2013; Pliotas et al., 2015; Wang et al., 2008) and cryoEM (T. Rasmussen et al., 2019;

Reddy et al., 2019), allowing for identification of regions likely to tolerate fluorescent reporter insertion. Finally, a large number of MscS variants have been created and tested to probe underlying causes of channel characteristics. We chose a select group of these MscS mutations for use in this study that either alter physiological function (Malcolm et al., 2011), gating kinetics (Akitake et al., 2007; Belyy, Anishkin, et al., 2010; Boer et al., 2011b; Machiyama et al., 2009; Takeshi Nomura et al., 2008; Edwards et al., 2008), tension sensitivity, or ion transport (Machiyama et al., 2009; Takeshi Nomura et al., 2006). We anticipated that these mutations enable us to alter sensor behavior in a potentially predictable manner, which is useful for altering tension sensor characteristics including tension sensitivity and ion transport ability.

For the fluorescent protein reporter, we chose modified circularly permuted GFP (mcpGFP). mcpGFP contains N- and C-termini locations modified from those of normal GFP that render its fluorescence intensity sensitive to conformational changes, including those caused by movement of a protein in which mcpGFP is inserted. The specific version of cpGFP we have chosen, mcpGFP, has already been used in ammonium transport biosensors, indicating its suitability for biosensor applications (De Michele et al., 2013). Our tension sensor candidates consist of MscS containing mcpGFP inserted at particular locations. Increases in lateral membrane tension are expected to cause conformational changes in MscS as it opens, which will alter the conformation of mcpGFP embedded within MscS and cause detectable changes in fluorescence intensity that reverse when the channel closes. Changes in mcpGFP fluorescence intensity are thus expected to reflect changes in membrane tension.

MscS is an MS ion channel that functions in *E. coli* osmoregulation. The physiological role of MscS also provides a straightforward way to trigger rapid, reversible changes in membrane tension to use for evaluating tension sensor candidates. MscS and another MS channel in *E. coli*, MscL, are required for hypoosmotic shock survival (Levina, 1999). During hypoosmotic shock, dramatic changes in cell size occur due to large influxes of water, which swells the cell and is proposed to increase membrane tension (Buda et al., 2016). Cells can then be hyperosmotically shocked, shrinking cells below their pre-shock volumes (Rojas et al., 2014), enabling a wide range of tensions to be assayed. All this can be monitored using conventional fluorescence microscopy and millifluidics devices, allowing for continuous monitoring of cell shape and fluorescence intensity during osmotic shock.

Membrane tension increases experienced by *E. coli* cells during hypoosmotic shock activate multiple MS ion channels, including MscS. MscS is a largely non-selective ion channel (S. Sukharev, 2002) with a conductance of ~330 pS when expressed in *Xenopus* oocytes (Grigory Maksaev & Haswell, 2011). MscS appears to be directly gated by forces from the membrane, as MscS retains mechanosensitive channel function when reconstituted into liposomes (S. Sukharev, 2002). In addition to closed and open states, MscS is proposed to enter a nonconductive, tension-insensitive inactivated state in response to sustained subsaturating tension or gradually increasing tension, speculated to protect *E. coli* from excessive ion release (Akitake et al., 2005, 2007; Belyy, Anishkin, et al., 2010; Boer et al., 2011b; Çetiner et al., 2018; Kamaraju et al., 2011).

MscS and mcpGFP-based tension sensor candidates are likely only indirectly tension sensitive when expressed in *E. coli* undergoing osmotic shock.

In this chapter, I describe our attempts at building a membrane tension sensor. First, we constructed an initial set of ten tension sensor candidates, each with a different insertion location for mcpGFP. Next, the MS channel activity of each sensor candidate was assessed to identify candidates likely undergoing dramatic tension-dependent conformational changes. The fluorescence intensity of two sensor candidates, $MscS^{S58}$-mcpGFP and $MscS^{A286}$-mcpGFP, and point mutants of each candidate was then measured when expressed in *E. coli* cells undergoing osmotic shock. Finally, signal intensities of *E. coli* cells expressing the first TM helix of MscS C-terminally tagged with mcpGFP were monitored and found to be identical to those of $MscS^{S58}$-mcpGFP when cells underwent osmotic shock. This indicated that fluorescence intensity changes of our tension sensor candidates likely indirectly reflect membrane tension during osmotic shock and do not directly reflect MscS mechanosensitivity.

3.3 Methods

Subcloning and site-directed mutagenesis. To create each sensor candidate, the full mcpGFP sequence, with XbaI cut site linker sequences on either side of mcpGFP was amplified from pDRf1-GW-mcpGFP (De Michele et al., 2013) and inserted at the desired location within MscS in pB10b-MscS (Okada et al., 2002). To create pOO2-MscS^{S58}-mcpGFP and pOO2-MscS^{A286}-mcpGFP for sensor candidate expression in *Xenopus* oocytes, MscS^{S58}-mcpGFP and MscS^{A286}-mcpGFP were cloned into pENTR using the pENTR/D-TOPO cloning kit (ThermoFisher Scientific) then cloned into a Gateway compatible version of pOO2 (Ludewig et al., 2002). Site directed mutagenesis was used to create L35A, D62N, L86N L35N, L86N I37N, F68N A51N, and G113A variants of MscS^{S58}-mcpGFP and MscS^{A286}-mcpGFP and mutations verified by sequencing.

Sensor candidate expression and localization in *E. coli*. Sensor candidate expression and membrane localization were verified by membrane fractionation and immunoblot analysis of *E. coli* cell lysates. ~10 colonies from freshly transformed MJF465 cells were added to 3 mL LB with 1 mM carbenicillin in a 14 mL culture tube and shaken at 37ºC, 250 rpm until OD600 ~0.5. 2 mL of this culture then added to 100 mL LB with 1 mM carbenicillin in a 250 mL flask and shaken at 37ºC, 250 rpm until OD600 ~0.5. Isopropyl β-D-1-thiogalactopyranoside (IPTG) then added to each culture to a final concentration of 1 mM and cultures shaken at 37ºC, 250 rpm for 30 min. For GFP signal imaging, cells were placed on 1% agarose pads, covered with a coverslip,

then brightfield and epifluorescent images obtained using an Olympus BX61 microscope, an Olympus DP71 digital camera, DP Controller software, and filter sets for GFP (470/40 nm excitation, 525/50 nm emission).

For fractionation, cell pellets were thawed on ice, then resuspended in 1 mL cold lysis buffer (50 mM Tris-HCl pH 7.5, 100 mM KCl, 10 mM EDTA, 10% glycerol, 1 mg/mL lysozyme, 1 mM DTT, one cOmplete Mini EDTA-free Protease Inhibitor tablet (Roche)). The resuspensions were then sonicated at 30% amplitude for six cycles of 10 s sonication/20 s rest. Lysates were spun down at 11,000 rpm, 4°C for 15 min, supernatant transferred to a new tube, then spun again at 11,000 rpm, 4°C for 15 min. The supernatant was spun in an ultracentrifuge using a TLA-100 rotor at 250,000 xg, 4°C for 30 min. The resulting supernatant was used as the soluble protein fraction and the resulting pellet was resuspended in an amount of 2x sample buffer equivalent to 24 µL per OD_{600} = 0.2 based on the final OD600 of the culture at the end of induction.

Sample volumes equivalent to equal cell densities were run on an SDS-PAGE gel with a 10% resolving gel then transferred to a PVDF membrane and blocked with 5% milk in 1x TBST overnight at 4°C. The blot was then probed with a 1:10,000 dilution of the Living Colors A.v. Monoclonal Antibody (JL-8) primary antibody (TaKaRa Bio USA, Inc) in 1x TBST with 5% milk, washed with 1x TBST, probed with a 1:10,000 dilution of anti-mouse HRP secondary antibody in 1x TBST with 5% milk, and washed again in 1x TBST. Signal detection was performed using SuperSignal West Dura Extended Dilution Substrate (ThermoFisher Scientific) and The blot was then washed with TBST and rocked for 5 min in Coomassie stain solution (50% methanol, 7% glacial

acetic acid, 0.1% w/v Coomassie Brilliant Blue R-250 (ThermoScientific), destained in a solution of 50% methanol, 7% glacial acetic acid, followed by a brief second destain in a solution of 90% methanol, 10% glacial acetic acid.

***E. coli* growth assays.** ~10 colonies of freshly transformed *E. coli* MJF465 cells dispersed in 3 mL normal glucose citrate-phosphate media (CphM; 60 mM Na_2HPO_4, 5 mM K_2HPO_4, 7 mM citric acid, 7 mM NH_4SO_4, 0.4 mM $MgSO_4$, 3 μM thiamine, 6 μM iron, 0.2% glucose) with 1 mM carbenicillin in a 14 mL culture tube and shaken at 30ºC, 250 rpm for 1 h. Two dilutions of each culture then made by mixing 750 μL culture with 750 μL normal glucose CphM, one with 1 mM IPTG and the other without. Dilutions then vortexed to mix and three 300 μL aliquots of each dilution loaded into a clear 96-well plate and placed into a plate reader. Plate was then shaken at 37ºC for 8 h, with OD_{600} measurements every 30 min.

***E. coli* hypoosmotic shock plating assays.** Plating assays were performed as described in (Bartlett et al., 2004) with some modifications. ~10 colonies of freshly transformed cells were dispersed in 3 mL normal glucose CphM with 1 mM carbenicillin in 14 mL culture tubes and shaken at 37ºC, 250 rpm until OD_{600} ~0.2. Cultures then diluted 1:1 in 1 M NaCl normal glucose citrate-phosphate media and shaken at 37ºC, 250 rpm until OD600 ~0.2. IPTG then added to each culture to a final concentration of 1 mM and cultures shaken at 37ºC, 250 rpm for 30 min to induce protein expression. Cultures then diluted 1:20 in either Millipore water (for shocked samples) or 0.5 M NaCl normal glucose CphM (for unshocked samples) and incubated at 37ºC for 15 min. Shock and unshocked samples then serially diluted six times, 1:10 for each dilution, in

either water or 0.5 M NaCl normal glucose CphM and 5 µL aliquots of each serial dilution plated on an LB plate containing 1 mM carbenicillin. Plates incubated at 30ºC overnight then the number of colonies for each dilution counted. % survival then calculated for each construct by dividing the number of colonies for shocked samples by the number of colonies for unshocked samples for dilutions producing between 1 and 50 colonies.

Patch-clamp electrophysiology. Patch-clamp electrophysiology was performed using *Xenopus* oocytes with buffers, conditions, and protocols described in (Grigory Maksaev & Haswell, 2015).

Flow cell construction and osmotic shock assays. Flow cells were built using a protocol developed by Rob Phillips's group at Caltech and used in (Chure et al., 2018; Bialecka-Fornal et al., 2015). Three holes were drilled in a T-shaped pattern into a 1.0 mm thick glass microscope slide (75 mm x 25 mm, VWR #48300-047) using 1.50 mm plated diamond flat-tip drill bits (C.R. Laurence Co., #MD1126) to create input/output ports for media. Glass then placed into a glass staining jar, covered in 1 M KOH, and sonicated using a sonicating water bath for 30 min. KOH then decanted, slides washed with Millipore water, then slides covered in 100% EtOH and sonicated for 30 min. Slides then dried by briefly running them through a flame and the ends dabbed with a Kimwipe then storing slides in a covered, dust-free container. Glass coverslips (#1.5, 22x50 mm, VWR #16002-264) also washed before use. Coverslips placed in a glass staining jar, covered in acetone, then incubated for 55 min. Coverslips then transferred to a jar filled with 100% EtOH and incubated for 10 min. Coverslips washed twice in Millipore water

then incubated in 0.1 M KOH for 15 min. Coverslips then rinsed twice with Millipore water and flame-dried then stored in a covered, dust-free container.

To construct the flow cells, three pieces of flexible tubing (Cole-Parmer tygon microbore tubing, 0.020” (ID) x 0.06” (OD), #EW-06419-01) cut at sharp angles to form two 15.5 cm long pieces for each input port and one 40.5 cm long tube for the output port. Push about 0.5 cm of tubing (starting from the angled end) through each port hole and apply 5-min epoxy around the external side of the flow cell where the longer length of tubing is. Allow epoxy to dry (be careful that it does not flow away from tubing while drying) then cut off the excess 0.5 cm of tubing from each porthole using a razorblade. Remove backing from T-shaped double-sided tape (SecureSeal adhesive, 0.1 mm thick, Grace Bio Labs) and apply to the inner side of the coverslip, being careful not to cover any portholes. Remove the other side of backing from the tape and carefully apply a clean coverslip, ensuring the seal between coverslip and tape is tight with no major bubbles. Flow cells then baked overnight at 60ºC prior to use.

To perform osmotic shock assays using flow cells, ~10 colonies of freshly transformed *E. coli* cells were placed in a 14 mL culture tube containing 3 mL LB with 1 mM carbenicillin and shaken at 37ºC, 250 rpm until OD600 ~0.5. Next, 100 µL of culture was diluted in 3 mL 500 mM NaCl M9 (48 mM Na_2HPO_4, 22 mM KH_2PO_4, 8 mM NaCl, 2 mM NH_4Cl, 2 mM $MgSO_4$, 0.1 mM $CaCl_2$, 0.4% glucose, pH 7.2) in a 14 mL culture tube until OD600 ~0.3, then IPTG added to a final concentration of 1 mM and culture shaken for another 1.5 h.

Once cells were ready, a flow cell was prepared for experimentation. A flow cell was positioned on an Olympus IX71 inverted microscope equipped with a 100x oil objective with output tubing connected to a syringe and one of the input tubes connected to a container of M9 media. First, 500 µL Millipore water was pulled through the flow cell followed by 500 µL 2.5% polyethyleneimine to create an adherent surface on the microscope slide for *E. coli* cells. Next, 500 µL Millipore water was pulled through the flow cell to remove excess PEI. The flow cell output tube was then connected to a syringe pump (operated at a flow rate of 200 µL/min) and a bubble added to the input tube connected to M9 media then moved such that the bubble separated the flow cell chamber from M9 media in the tube. Next, using the input tube not connected to normal M9 media, the flow cell was flushed with 500 mM NaCl M9 media and cells sucked into the flow cell chamber and allowed to adhere to the slide. After 10 min of incubation, 500 mM NaCl M9 media was pulled through the flow cell to remove unbound cells and osmotic shock experiments performed.

Fluicell osmotic shock assays. To perform osmotic shock assays using the Fluicell, cells were prepared in the same way as for flow cell osmotic shock assays and experiments performed using an Olympus IX71 inverted fluorescence microscope. The bottom of a glass-bottomed dish was covered in 2.5% PEI and incubated at room temperature for 10 min. The bottom of the dish was then gently washed twice with Millipore water, covered in 500 mM NaCl M9 media, and incubated at room temperature for 5 min. Prepared cells then added to the dish and allowed to adhere to the bottom for

10 min at room temperature. Media was then gently aspirated from a corner of the dish and fresh 500 mM NaCl M9 media added to the dish.

Next, the Fluicell was prepared for use in osmotic shock assays. A fresh Fluicell tip was loaded with 30 µL media into each of the four tip wells, two wells were with M9 media and the other two wells with 500 mM NaCl media. After any bubbles present were removed from each well then the Fluicell tip was loaded into the Fluicell chamber and the chamber tightly sealed. The fluidic device was then centered relative to the microscope objective and initialized using the Fluicell software. The resulting drop at the tip of the Fluicell was then removed and the device lowered such that the tip was completely submerged in media, at which point the “run” function of the Fluicell software was engaged. The device was then adjusted using the 10x objective such that the Fluicell tip was centered in the field of view. Next, a 100x objective was used to bring cells into focus and lower the Fluicell tip into the same plane as the bacterial cells. Fluicell flow settings and position were adjusted such that as many cells in a given field of view would be affected by osmotic shocks as possible and experiments begun.

Cell size analysis. Cell size, length, and width were analyzed as follows. First, all images in a given time-lapse were saved as tiff files and loaded in Fiji (Schindelin et al., 2012). A single cell that remained flat throughout the entire experiment and showed a response to osmotic shock was selected and the image cropped in each time-lapse frame such that only that cell was visible. Background intensity was then measured and subtracted from all time-lapse images. The threshold was then adjusted to maximize contrast between the cell and background and this threshold applied to all images in the

series. A macro was then created in which the magic wand tool was used to measure total area of each cell for each image in the time lapse.

3.4 Results

Tension sensor candidate design. We first created ten tension sensor candidates by inserting mcpGFP (De Michele et al., 2013) at locations within MscS that we predicted would be amenable to mcpGFP insertion based on their lack of defined secondary structure in published MscS structures (Bass et al., 2002; Lai et al., 2013; T. Rasmussen et al., 2019; Wang et al., 2008). These included two sites within the cytoplasmic loop connecting TM1 and TM2 (S58 and I61), seven sites within the cytoplasmic cage region of MscS (P129, G139, A172, S179, R185, G265, and P269), and one site at the C-terminus of MscS (A286) (Figure 3.1). The version of mcpGFP inserted into MscS lacked a start codon and was flanked at both the N- and C-terminus by a Ser-Arg linker.

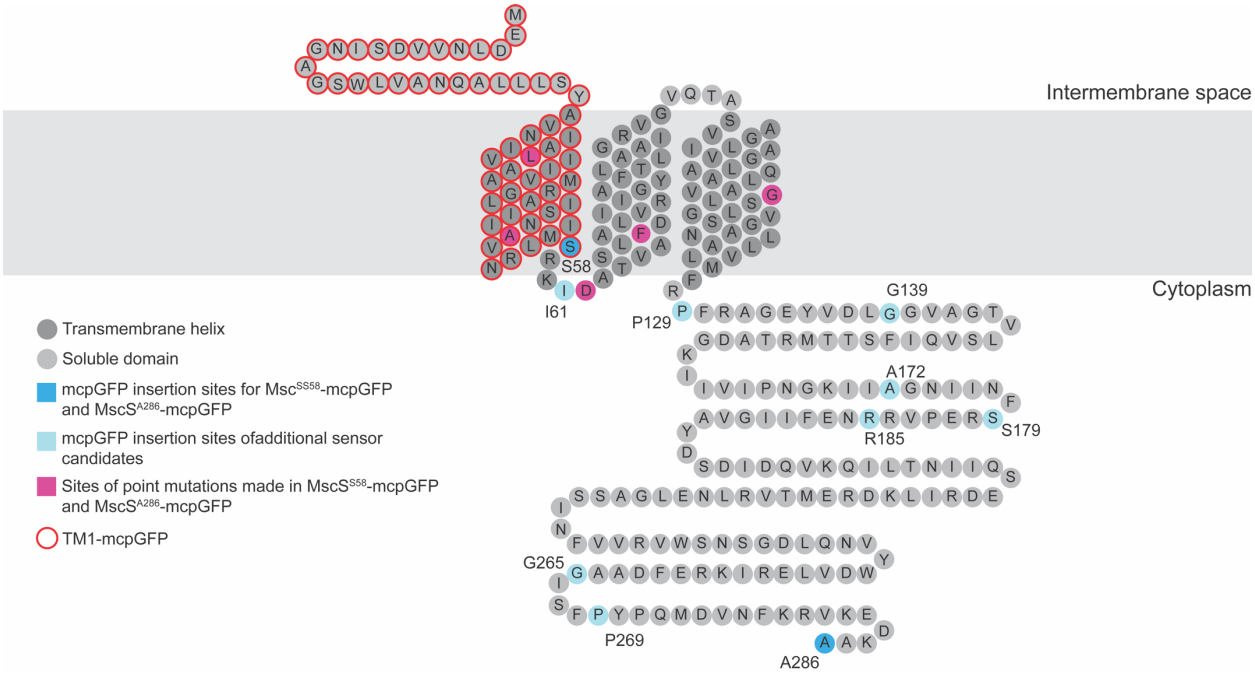

Figure 3.1. Map of mcpGFP insertion sites and mutated residues used for MscS-based tension sensor development. Individual residues of MscS and their position within the inner membrane of *E. coli.*

Residues in transmembrane helices are shown in dark gray and residues in soluble domains are shown in light gray (Bass et al., 2002; Miller, 2003). Sites where mcpGFP was inserted are shown in blue. S58 and A286 (dark blue) were most extensively characterized here. Residues mutated in sensor variants are shown in magenta. Residues included in the TM1-mcpGFP construct are indicated by red outlines.

Sensor candidates are membrane-localized and show varying levels of basal fluorescence intensity when expressed in *E. coli* cells. We also assessed membrane localization of sensor candidates when expressed in *E. coli* MJF465 cells using immunoblotting of microsomal fractions with free GFP as a control (Figure 3.2A). All sensor candidates were present as full-length proteins at similar levels in microsomal fractions except for MscS^{S58}-mcpGFP and MscS^{I61}-mcpGFP, which were present in microsomal fractions at slightly lower levels compared to other sensor candidates. These results demonstrate that all ten sensor candidates are produced as full-length membrane localized proteins, meeting our first requirement for membrane tension sensor candidates.

We next sought to compare the relative levels of basal fluorescence when our sensor candidates were expressed in *E. coli* MJF465 strain cells under normal conditions (Figure 3.2B), since it is possible that placing mcpGFP at different locations in MscS produced signal of varying intensities upon expression. Six sensor candidates (MscS^{S58}-mcpGFP, MscS^{I61}-mcpGFP, MscS^{G139}-mcpGFP, MscS^{S179}-mcpGFP, MscS^{G265}-mcpGFP, and MscS^{A286}-mcpGFP) produced GFP signal localized to the cell periphery that was visible using fluorescence microscopy. This signal was distinct from the cytoplasmic signal of cells expressing free GFP and comparable to previously reported MscS-GFP signal (Romantsov et al., 2010; van den Berg et al., 2016),

suggesting membrane localization of sensor candidates. Four candidates (MscS^{P129}-mcpGFP, MscS^{A172}-mcpGFP, MscS^{R185}-mcpGFP, and MscS^{P269}-mcpGFP) did not produce visible GFP signal when expressed in *E. coli* MJF465 cells.

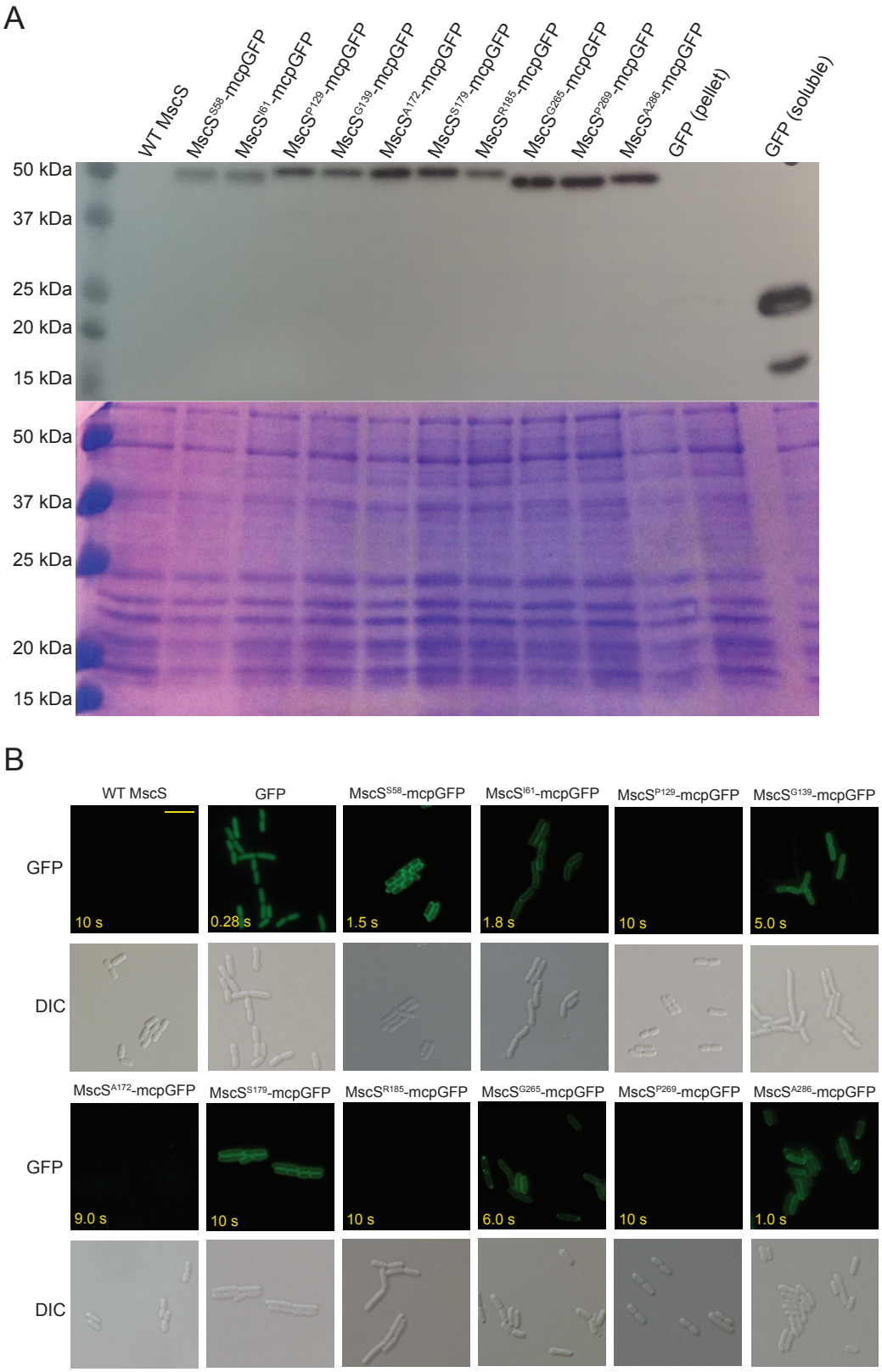
A
WT MscS
MscS^S58-mcpGFP
MscS^I61-mcpGFP
MscS^P129-mcpGFP
MscS^G139-mcpGFP
MscS^A172-mcpGFP
MscS^S179-mcpGFP
MscS^R185-mcpGFP
MscS^G265-mcpGFP
MscS^P269-mcpGFP
MscS^A286-mcpGFP
GFP (pellet)
GFP (soluble)
50 kDa
37 kDa
25 kDa
20 kDa
15 kDa
50 kDa
37 kDa
25 kDa
20 kDa
15 kDa
B
WT MscS
GFP
MscS^S58-mcpGFP
MscS^I61-mcpGFP
MscS^P129-mcpGFP
MscS^G139-mcpGFP
GFP
DIC
10 s
0.28 s
1.5 s
1.8 s
10 s
5.0 s
MscS^A172-mcpGFP
MscS^S179-mcpGFP
MscS^R185-mcpGFP
MscS^G265-mcpGFP
MscS^P269-mcpGFP
MscS^A286-mcpGFP
GFP
DIC
9.0 s
10 s
10 s
6.0 s
10 s
1.0 s

Figure 3.2. The majority of sensor candidates show membrane-localized GFP signal in *E. coli*. (A) Anti-GFP immunoblot of microsomal fractions from lysates of E. coli MJF465 cells expressing sensor candidates and both soluble and microsomal fractions are shown from E. coli MJF465 cells expressing free GFP. Sample volumes were normalized based on cell density after induction to ensure equal loading of total protein. Coomassie staining of the blot to detect total protein levels is shown below the immunoblot. (B) GFP fluorescence and DIC images of E. coli expressing either the indicate sensor candidate, cytoplasmic GFP, or untagged MscS. The exposure time used for each fluorescence image is indicated. Scale bar is 5 μm.

MscS^{A286}-mcpGFP protects *E. coli* MJF465 cells from osmotic shock while MscS^{S58}-mcpGFP and MscS^{I61}-mcpGFP show cell toxicity. We next determined if any sensor candidates protect *E. coli* MJF465 cells from hypoosmotic shock. Such phenotypes would suggest that a particular sensor candidate undergoes conformational changes in response to changes in membrane tension, a critical step for generating tension-dependent conformational changes in mcpGFP. We first examined the growth of *E. coli* MJF465 cells expressing sensor candidates, untagged MscS, or an empty vector in minimal media both with and without IPTG. Expression of MscS^{S58}-mcpGFP or MscS^{I61}-mcpGFP caused dramatic decreases in *E. coli* growth over an 8 h period while no differences were observed in growth during IPTG-induced expression of any other sensor candidates or controls (Figure 3.3A). These results indicate that MscS^{S58}-mcpGFP and MscS^{I61}-mcpGFP alter cellular physiology, perhaps through gain-of-function behavior (Blount et al., 1997).

We also assessed the ability of each sensor candidate to provide protection from cell swelling using a hypoosmotic shock assay with *E. coli* MJF465 cells (Levina, 1999) (Figure 3.3B). *E. coli* MJF465 cells lack the MS channels MscS, MscL, and MscK and thus cannot survive severe hypoosmotic shock without sufficient expression of a

functional MS ion channel (Levina, 1999). In this assay, cells are grown in citrate-phosphate media with 500 mM NaCl, channel expression induced, then cells either transferred to water for a hypoosmotic shock or transferred to the same high salt media, after which cells are plated and grown overnight. MJF465 cells expressing a functional channel like MscS survive and produce colonies, which can be used as an indication of potential MS ion channel activity.

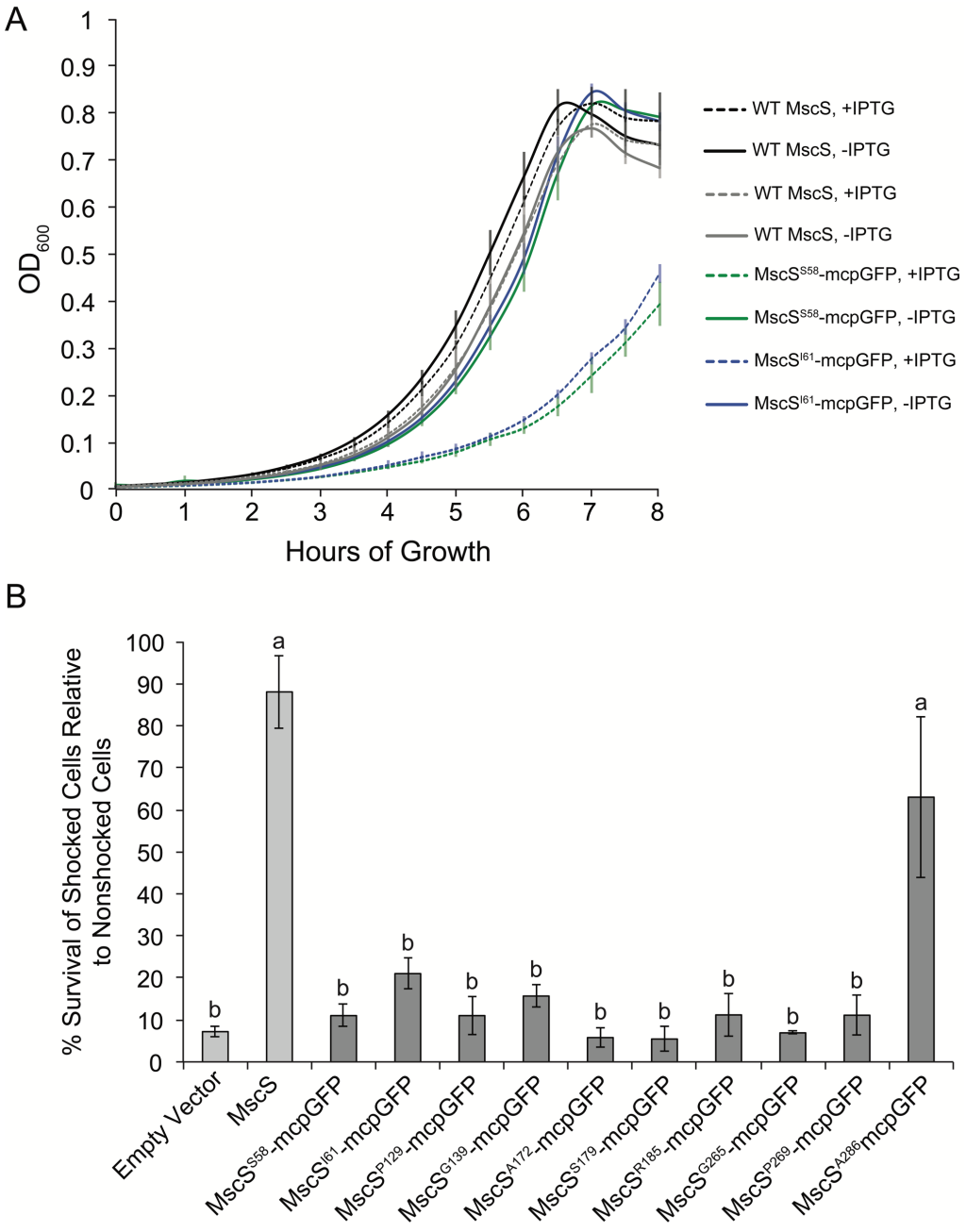

Figure 3.3. MscS^{S58}-mcpGFP and MscS^{I61}-mcpGFP inhibit cell growth while MscS^{A286}-mcpGFP enables hypoosmotic shock survival by *E. coli* MJF465 cells. (A) Representative growth curves of *E. coli* MJF465 cells transformed with either pB10b-MscS (black), pB10b-MscS^{S58}-mcpGFP (red), or pB10b-MscS^{I61}-mcpGFP in the presence or absence of 1 mM IPTG (solid and dashed lines, respectively). OD_{600} measurements were taken every 30 min for a total of 8 h and background absorbance subtracted from each measurement. Each data point represents the average of three technical replicates and the assay

was repeated twice more (data not shown), producing similar results each time. (B) Hypoosmotic shock survival rates of cells expressing either a sensor candidate (dark gray), untagged MscS positive control (light gray), or empty vector negative control (light gray) relative to unshocked controls. Data shown are averages ± standard deviation from three assays per sensor candidate and sixteen assays per control. Statistical analysis performed using one-way ANOVA with post-hoc Scheffe's test, $p < 0.05$.

Out of all ten sensor candidates, only MscS^{A286}-mcpGFP conferred hypoosmotic shock survival at rates statistically comparable to untagged MscS (63.0 ± 33.1% vs 88.0 ± 4.6%, one-way ANOVA with post-hoc Scheffe's test, $p < 0.05$). This suggests that MscS^{A286}-mcpGFP is still functional while the behavior of other candidates is disrupted. We can therefore place our sensor candidates in three categories based on their activity in *E. coli*. The first category are candidates which show no function during hypoosmotic shock yet also do not hinder growth, which includes most sensor candidates. The second category are candidates without function during hypoosmotic shock but that hinder cell growth, which includes MscS^{S58}-mcpGFP and MscS^{I61}-mcpGFP. The third category are candidates with normal function during hypoosmotic shock that do not alter growth and only includes MscS^{A286}-mcpGFP.

Interestingly, candidates belonging to each categories have similarities in their mcpGFP insertion site location (Figure 3.1). This makes sense, as inserting a relatively large protein like mcpGFP into different locations of the same structure in MscS might be expected to similarly perturb channel function. All first category candidates, which lack function, have mcpGFP inserted into the cytoplasmic cage domain of MscS. Since these candidates do not show obvious channel-associated behavior, we chose not to study them further. Both second category candidates MscS^{S58}-mcpGFP and MscS^{I61}-

mcpGFP have mcpGFP inserted in the cytoplasmic loop between TM1 and TM2. These candidates hinder cell growth while lacking function during hypoosmotic shock, potentially indicating gain-of-function MS channel behavior. Since both candidates behaved similarly and have nearby mcpGFP insertion sites, we chose the brighter of the two, MscS^{S58}-mcpGFP, to further test, as brighter signal may allow for a greater dynamic range. Finally, MscS^{A286}-mcpGFP, making up the third category, shows normal function during hypoosmotic shock, suggestive of MS channel activity. As mcpGFP in MscSA286-mcpGFP is only attached to MscS by its N-terminal end and at the C-terminus of MscS, far from S58, we thought it would also provide valuable contrast to MscS^{S58}-mcpGFP. We thus also chose to further examine MscS^{A286}-mcpGFP.

MscS^{S58}-mcpGFP and MscS^{A286}-mcpGFP show MS channel activity when expressed in *Xenopus* oocytes. We next characterized the MS ion channel activity of MscS^{S58}-mcpGFP and MscS^{A286}-mcpGFP in *Xenopus* oocytes, an established system for characterizing MscS channel activity (Grigory Maksaev & Haswell, 2011) (Figure 3.4). MscS^{A286}-mcpGFP produced readily detectable pressure-gated channel activity when expressed in *Xenopus* oocytes (Figure 3.4B-C). An IV curve of single channel conductance of MscS^{A286}-mcpGFP indicated a linear relationship between current and potential that is identical to that of MscS-GFP over membrane potentials from -40 mV to 40 mV (Grigory Maksaev & Haswell, 2011). In addition, MscS^{A286}-mcpGFP also showed similar gating pressures as MscS-GFP, however, without curve fitting of MscS^{A286}-mcpGFP traces the exact relationship between their gating pressures is not known. These results thus confirm that MscSA286-mcpGFP has pressure-gated channel

activity in *Xenopus* oocytes and thus likely undergoes tension-dependent conformational changes.

MscS^{S58}-mcpGFP exhibited flickery pressure-gated activity (Figure 3.4B) that was only detected in 23% of patches (12 out of 53) examined compared to 100% of patches examined for MscS^{A286}-mcpGFP (12 patches total). MscS^{S58}-mcpGFP also required relatively high levels of applied pressure to gate, causing many patches to rupture before any current was detected. This channel also showed a conductance of ~300 pS at 40 mV, similar to that reported for WT MscS (Grigory Maksaev & Haswell, 2011), although this was only determined for one membrane potential. MscS^{S58}-mcpGFP and MscS^{A286}-mcpGFP thus appear to differ in tension sensitivity and open state stability but not conductance.

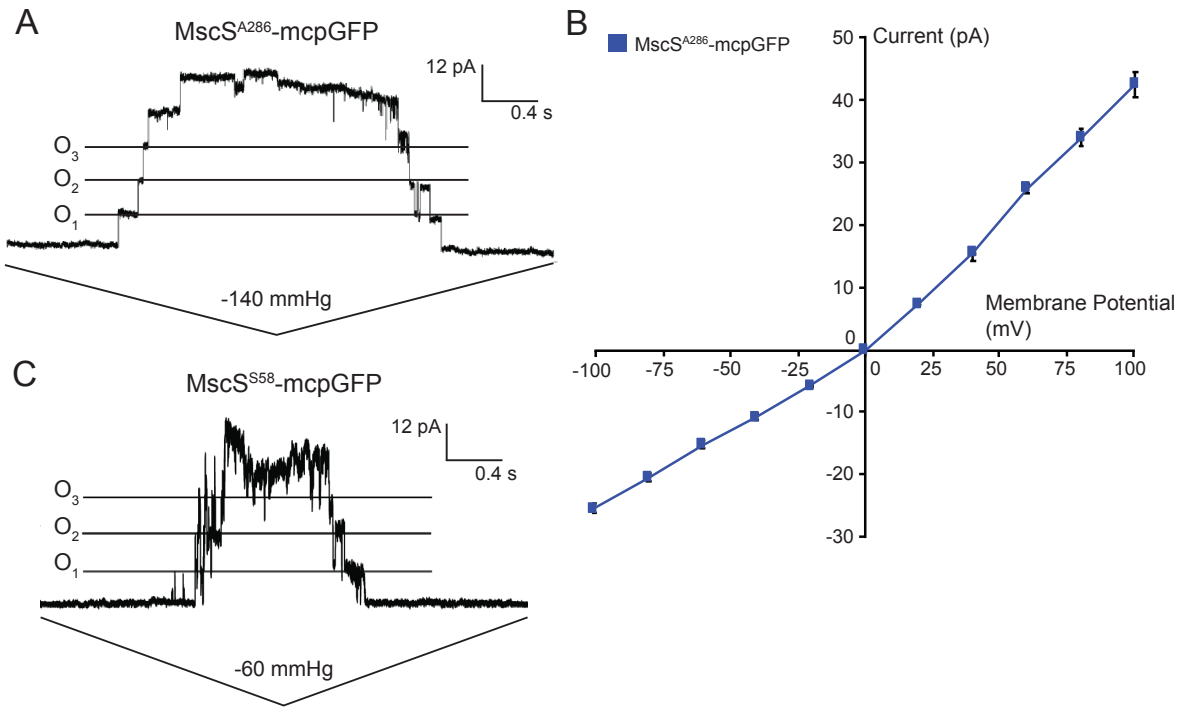

Figure 3.4. MscS^{S58}-mcpGFP shows occasional flickery channel activity while MscS^{A286}-mcpGFP shows typical MscS behavior when expressed in Xenopus oocytes. (A) Representative trace of channel activity from oocytes expressing MscS^{A286}-mcpGFP at a membrane potential of -40 mV in response to a 4 s pressure ramp to a maximum negative pressure of -140 mmHg. Three channel opening events are indicated with O_1, O_2, and O_3 labels. (B) IV curve of single channel currents from Xenopus oocytes MscS^{A286}-mcpGFP at membrane potentials ranging from -100 mV to 100 mV. Each data point represents the average single channel current measured from 3 to 8 oocytes and is shown ± standard deviation. (C) Representative trace of channel activity from oocytes expressing MscS^{S58}-mcpGFP at a membrane potential of -40 mV in response to a 4 s symmetric pressure ramp with maximum negative pressure of -60 mmHg. Three channel opening events were observed and are labelled as O_1, O_2, and O_3.

Cell size and MscS^{A286}-mcpGFP signal intensity change during hypoosmotic shock and alternating hypo- and hyperosmotic shocks in *E. coli* FRAG-1 cells. After selecting sensor candidates for further testing, we developed osmotic shock assays that allowed us to apply severe osmotic shocks while quantifying signal intensity from individual *E. coli* cells. We first determined if hypoosmotic shock

caused by moving FRAG-1 cells from 500 mM NaCl M9 media to 0 mM NaCl M9, similar to conditions used for hypoosmotic plating assays, would trigger measurable changes in size and MscS^{A286}-mcpGFP signal intensity (Figure 3.5). Cells grown in 500 mM NaCl M9 were allowed to adhere to a polyethyleneimine-coated glass dish or flow cell, then media quickly (~1 s) replaced with 0 mM NaCl M9. Cell length, area, and width were then measured by thresholding fluorescence images of single cells to remove background signal, then fitting ellipses and obtaining measurements of the long and short axes using ImageJ. Cell area, width, and length all showed similar patterns of change after the start of hypoosmotic shock and increased for ~10 s, decreased for 50-100 s, then recovered to pre-shock levels over 100-200 s (Figure 3.5A-C). This timeline for cell size change during hypoosmotic shock is consistent with that previously shown (Buda et al., 2016), giving us confidence that we were successfully applying severe hypoosmotic shock to our cells.

MscS^{A286}-mcpGFP signal intensity changes during sustained hypoosmotic shock were divided into four phases: pre-shock, shock response, recovery, and post-recovery (Figure 3.5D). Before hypoosmotic shock, when cells were in 500 mM M9, only minimal intensity changes were observed, indicating that MscS^{A286}-mcpGFP signal does not change under normal conditions. Immediately upon shock, MscS^{A286}-mcpGFP signal drops by 30% for ~10 s then gradually rises to pre-shock levels for ~60 s. MscS^{A286}-mcpGFP signal thus detectably and reversibly changes during hypoosmotic shock, indicating that the dynamic range of MscS^{A286}-mcpGFP signal is appropriate for these experiments. Finally, MscS^{A286}-mcpGFP signal changes coincide with shock-induced

cell swelling and shrinking, indicating a possible link between membrane tension and MscS^{A286}-mcpGFP signal.

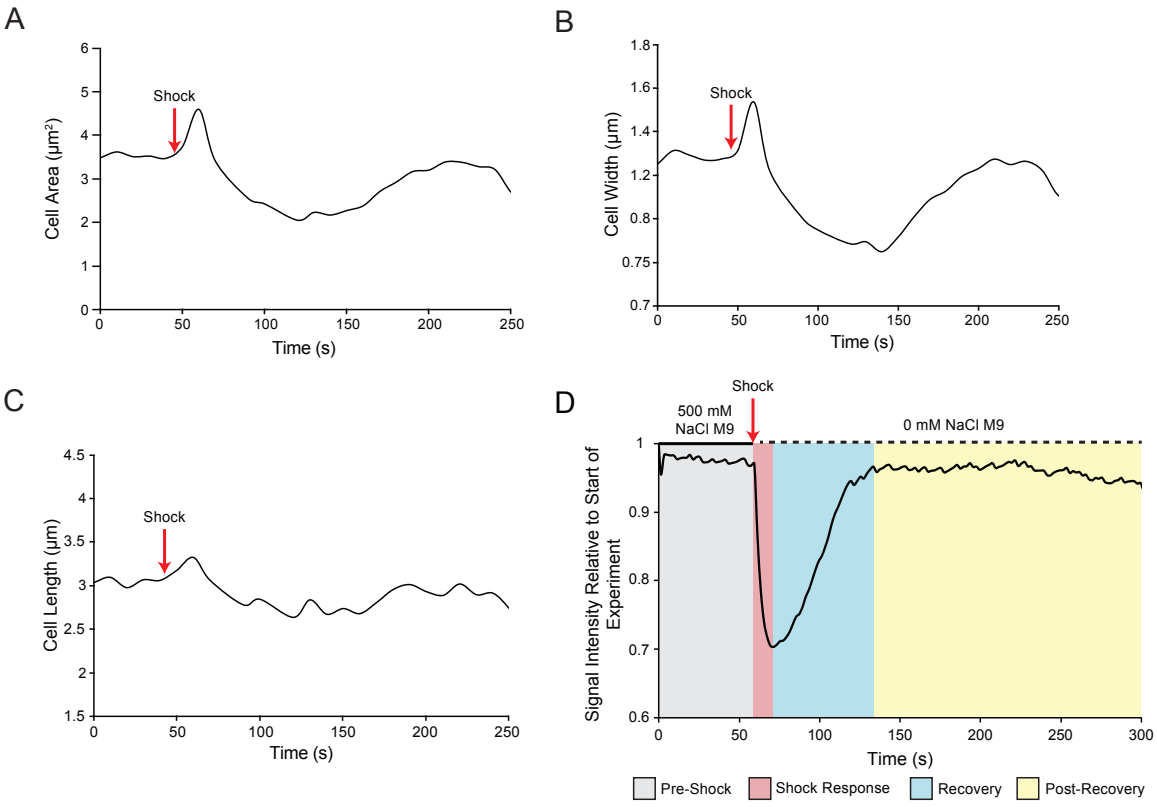

Figure 3.5. Cell size and MscSA286-mcpGFP signal undergo multiple changes during hypoosmotic shock. (A-C) Average cell area (A), width (B), or length (C) of an *E. coli* FRAG-1 cell expressing MscS^{A286}-mcpGFP during hypoosmotic shock. Cell dimensions are shown as either black or grey lines for each respective cell. (D). Relative MscS^{A286}-mcpGFP signal intensity before and during hypoosmotic shock. Signal changes are classified into four categories indicated by background color: pre-shock (gray), shock response (pink), recovery (blue), and post-recovery (yellow).

We next exposed *E. coli* FRAG-1 cells expressing free GFP and MscS^{A286}-mcpGFP to alternating hypo- and hyperosmotic shock by rapidly switching cells between 500 mM NaCl M9 and 0 mM NaCl M9 media. This allowed us to further probe the reversibility and dynamic range of our sensor. Additionally, by only allowing each

shock to occur for 20 s, we can limit cellular responses to osmotic shock beyond changes in cell size and membrane tension. Cells in 500 mM NaCl M9 media were allowed to adhere to polyethyleneimine-coated glass dishes and media exchanged using the Fluicell, which permitted <1 s media exchanges. Cell area and signal intensity changes were then measured from GFP-expressing and MscS^{A286}-mcpGFP-expressing cells, respectively. Cell area was measured from GFP-expressing cells as the brighter signal of cytoplasmic GFP was thought to be better for ensuring accurate area measurements using our thresholding method.

Alternating hypoosmotic and hyperosmotic shocks produced three main types of area change: hypoosmotic response 1, hypoosmotic response 2, and hyperosmotic response (Figure 3.6A). Application of the first hypoosmotic shock after cells had been grown and equilibrated in 500 mM NaCl M9 triggered a small, sudden 5% increase in size (Figure 3.6A, hypoosmotic response 1). Next, during hyperosmotic shock, cells shrank by 25-30%, with similar responses observed for additional hyperosmotic shocks (hyperosmotic response, Figure 3.6A). Finally, application of additional hypoosmotic shocks increased cell size by ~20% (Figure 3.6A, hypoosmotic response 2). Subsequent shock cycles caused cells to alternate between hyperosmotic response and hypoosmotic response 2 without exhibiting hypoosmotic response 1. The size changes observed during the hyperosmotic response and hypoosmotic response 2 are much larger than during hypoosmotic response 1 but occur over smaller values of cell area. Cycling osmotic shocks allow us to probe signal change over larger changes with smaller cell area values, expanding our capabilities for testing sensor candidate

responses. In addition, the short duration of area changes upon shock and lack of subsequent size changes in our cycling experiments suggests minimization of cellular responses to osmotic shock, including restoration of osmotic equilibrium, which might drive opposing cell size changes.

Alternating hypo- and hyperosmotic shocks also produced three different types of signal intensity changes from MscS^{A286}-mcpGFP (Figure 3.6B), corresponding to hypoosmotic response 1, hyperosmotic response, and hypoosmotic response 2 and composed of parts termed “shock response” and “recovery”. Unexpectedly, while hypoosmotic and hyperosmotic shocks were expected to produce opposing changes in MscS^{A286}-mcpGFP signal, hypoosmotic response 1 and hyperosmotic response both coincided with decreases in MscS^{A286}-mcpGFP signal (~20% and ~5%, respectively) while hypoosmotic response 2 was associated with a ~5% increase in MscS^{A286}-mcpGFP. Additionally, while hypoosmotic response 1 includes a much smaller relative change in area compared to hypoosmotic response 2 and hyperosmotic response, it is associated with a much larger change in MscS^{A286}-mcpGFP. Such differences in magnitude may reflect differences in cell size and membrane tension or the presence of additional cellular factors affecting MscS^{A286}-mcpGFP signal intensity during any one of these experimental stages.

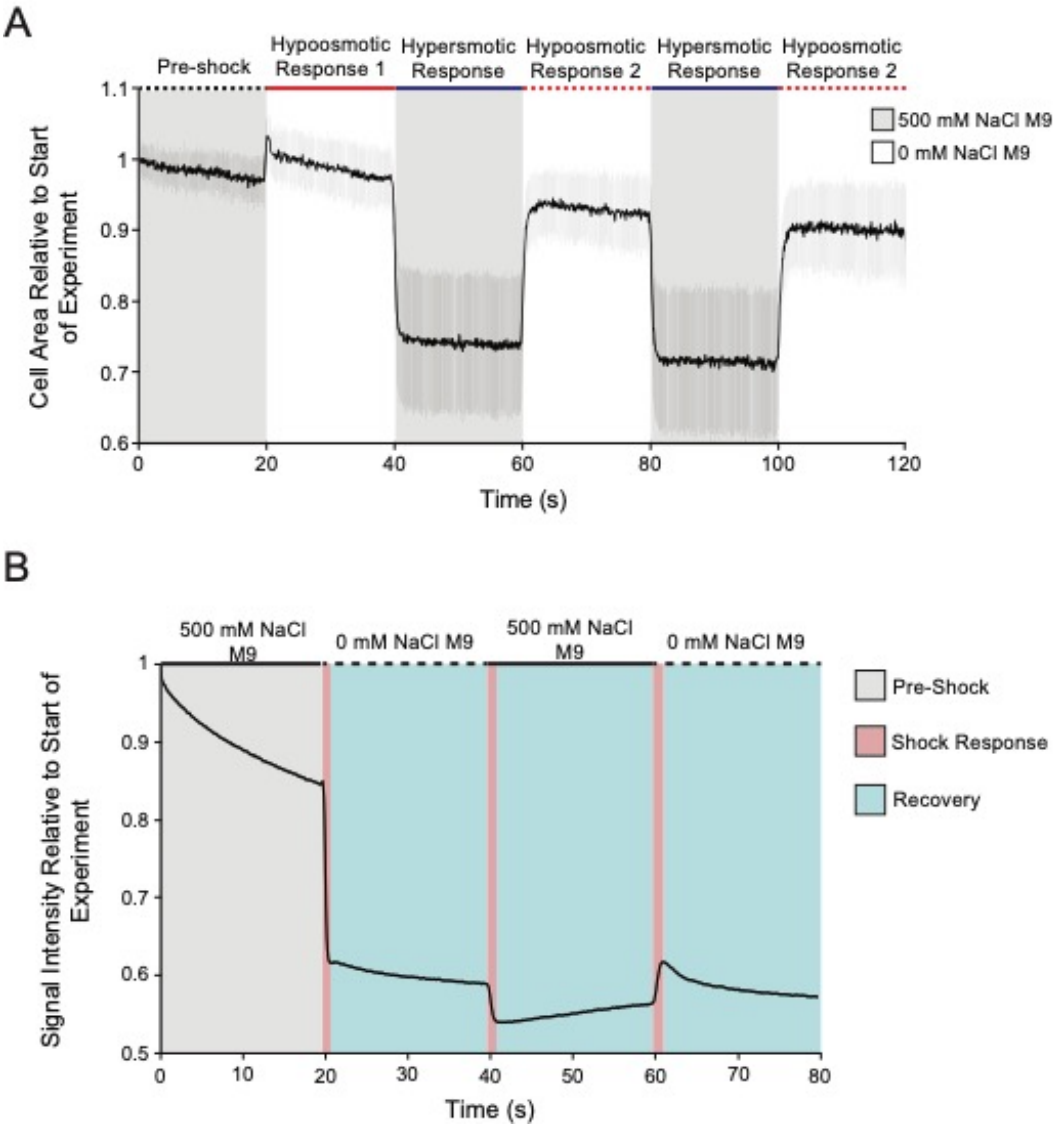

Figure 3.6: Cell area and MscS^{A286}-mcpGFP signal rapidly and reversibly change during alternating hypo- and hyperosmotic shock in *E. coli* FRAG-1 cells. (A) Average relative cell area of E. coli FRAG-1 cells expressing free GFP during alternating hypo- and hyperosmotic shocks. The changes in area during osmotic shock are classified as either hypoosmotic response 1 (red solid line), hypoosmotic response 2 (red dashed line), or hyperosmotic response (solid blue line), with pre-shock area indicated by a dashed black line. (B) Average relative signal intensity of MscS^{A286}-mcpGFP in FRAG-1 cells. Signal

intensity levels are classified as either pre-shock, shock response, or recovery depending on time and change.

The fluorescence intensity of MscS^{S58}-mcpGFP and MscS^{A286}-mcpGFP sharply decreases then gradually recovers in *E. coli* cells experiencing hypoosmotic shock. We next compared signal intensity changes of MscS^{A286}-mcpGFP during osmotic shock in *E. coli* strains FRAG-1 and MJF465. Signal intensity of MscS^{A286}-mcpGFP also immediately dropped upon hypoosmotic shock in FRAG-1 and MJF465 cells, after which the signal gradually recovered to pre-shock levels. The main difference in signal changes between cell types was the level of the initial signal drop (~17% vs ~25%, respectively; Figure 3.7A). This indicates that the loss of MS channels in MJF465 cells compared to FRAG-1 cells increases MscS^{A286}-mcpGFP signal change during the initial stage of hypoosmotic shock involving cell swelling, not shock recovery and cell shrinking. As MJF465 cells here lack MscK and MscL activity but possess MscS activity due to the channel function of MscS^{A286}-mcpGFP, the loss of MscK and MscL appear to cause a more extreme initial hypoosmotic shock response, perhaps due to increased swelling, or alterations to cellular conditions pre-shock.

We next examined signal intensity change of MscS^{S58}-mcpGFP in *E. coli* FRAG-1 and MJF465 strains during hypoosmotic shock (Figure 3.7B). In *E. coli* FRAG-1 cells, MscS^{S58}-mcpGFP showed an immediate drop in signal intensity of 30%, followed by a gradual recovery to 95% of pre-shock levels over the course of ~50 s (Figure 3.7A; black line). Like MscS^{A286}-mcpGFP, MscS^{S58}-mcpGFP signal thus decreases with cell swelling and increases to pre-shock levels during cell shrinking, based on the analysis

in Figure 3.5. While MscS^{S58}-mcpGFP signal in *E. coli* FRAG-1 and MJF465 cells showed similar patterns of signal change and degrees of initial signal drop, MscS^{S58}-mcpGFP in MJF465 cells showed a delay in signal recovery compared to in FRAG-1 cells (Figure 3.7A). This indicates decreased recovery of MJF465 cells expressing MscSS58-mcpGFP, potentially reflecting the decrease in cell shrinking observed for *E. coli* cells lacking MscS and MscL (Buda et al., 2016).

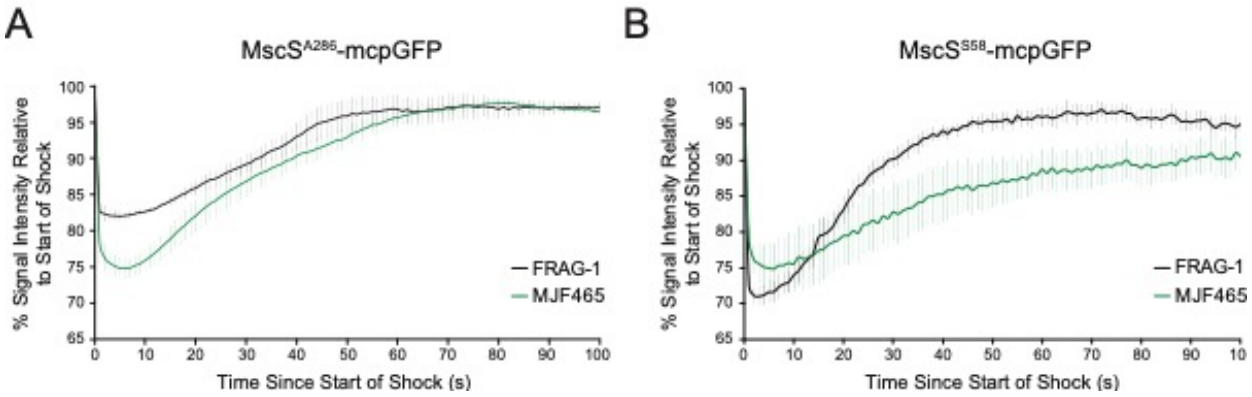

Figure 3.7. The signal intensity of cells expressing MscS^{S58}-mcpGFP and MscS^{A286}-mcpGFP changes in response to hypoosmotic shock. Signal intensity of MscS^{A286}-mcpGFP (A) and MscS^{S58}-mcpGFP (B) in *E. coli* FRAG-1 and MJF465 cells during hypoosmotic shock. Signal intensity is normalized to t = 0 s and is presented as the average ± standard error for all cells examined. Data obtained from 2-6 hypoosmotic shock assays involving 28-220 cells per strain/sensor candidate combination.

Multiple point mutations in transmembrane helices of MscS^{A286}-mcpGFP alter results of physiological assays in *E. coli*. After establishing that both MscS^{S58}-mcpGFP and MscS^{A286}-mcpGFP show transient drops in signal intensity during osmotic shock, we wanted to determine whether mutations to MscS would alter these signal changes. Point mutations to MscS that alter channel behavior likely alter tension-dependent conformational changes, which would be expected to alter tension-

dependent sensor candidate responses to osmotic shock. We therefore created a series of point mutations in both MscS^{S58}-mcpGFP and MscS^{A286}-mcpGFP that have been previously shown to alter channel behavior, described below.

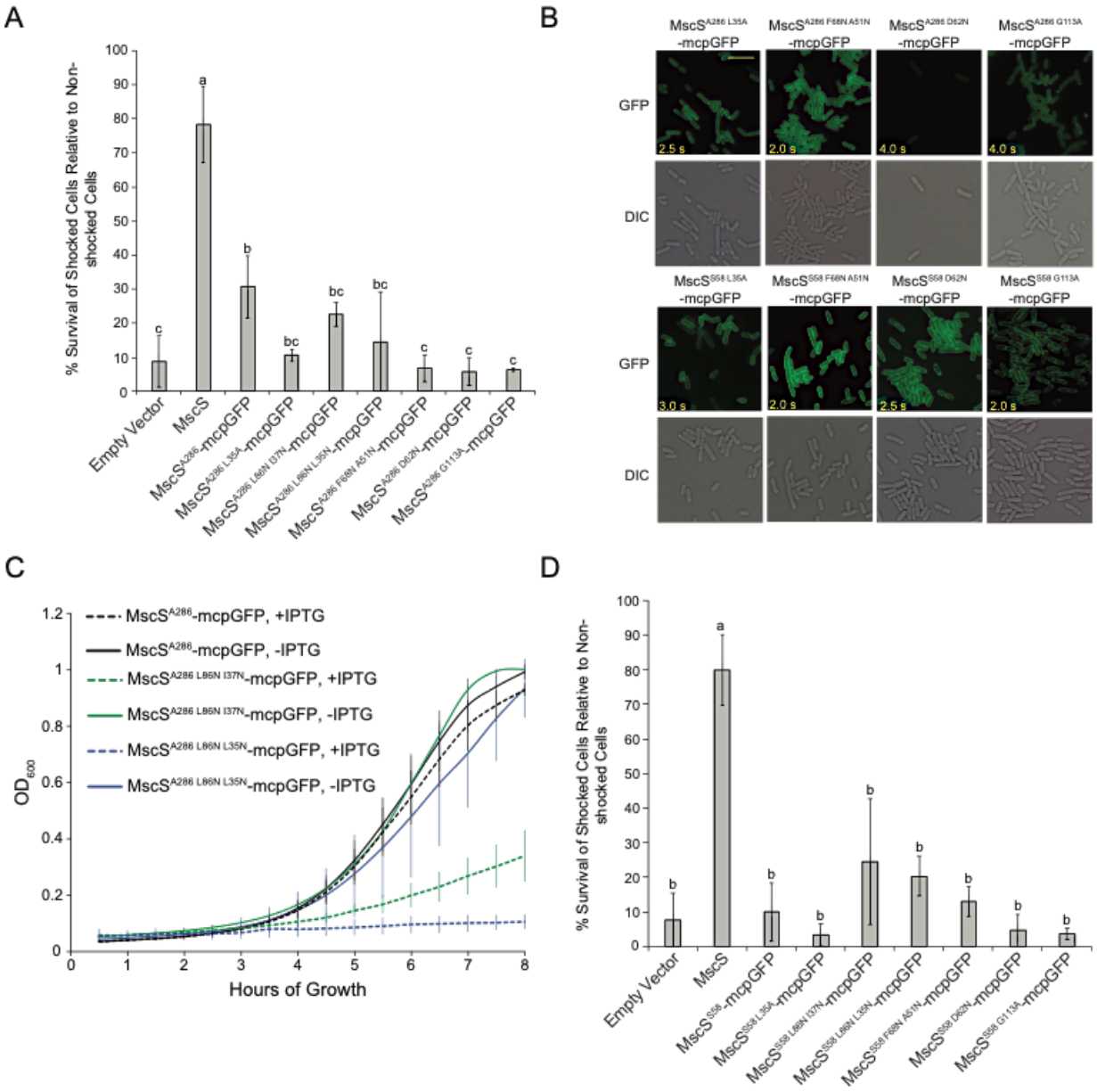

Figure 3.8. Multiple MscS^{A286}-mcpGFP variants show altered effects in *E. coli* compared to MscS^{A286}-mcpGFP. (A) Hypoosmotic shock survival rates of *E. coli* MJF465 cells expressing the indicated protein relative to unshocked controls. Data are shown as average survival rates ± standard deviation of either three assays for each MscS^{A286}-mcpGFP variant or eighteen assays for MscS^{A286}-mcpGFP, untagged MscS, or an empty vector. Statistical groups were generated using one-way ANOVA with post-hoc Scheffe's test, $p < 0.05$. (B) GFP fluorescence and bright field images of *E. coli* MJF465 cells expressing MscS^{A286}-mcpGFP variants or MscS^{S58}mcpGFP variants chosen for further analysis. Images were taken using fluorescence microscopy and exposure times used for each GFP fluorescence

image are shown. Scale bar is 5 μm. (C) Growth curves of *E. coli* MJF465 cells expressing the indicated protein in the presence or absence of 1 mM IPTG (dashed and solid lines, respectively). OD_{600} values of three technical replicates were measured then averaged every 30 min to generate the curves shown (± standard deviation). (D) Hypoosmotic shock survival rates of *E. coli* MJF465 cells expressing the indicated protein relative to unshocked controls. Data shown are average survival rates ± standard deviation of either three assays for cells expressing most $MscS^{S58}$-mcpGFP variants, two assays for cells expressing $MscS^{S58\ F86N\ A51N}$-mcpGFP, or seventeen assays for cells expressing $MscS^{S58}$-mcpGFP, untagged MscS, or an empty vector. Statistical groups were generated using one-way ANOVA with post-hoc Scheffe's test, $p < 0.05$.

We first evaluated the effect of $MscS^{A286}$-mcpGFP variant expression on growth and hypoosmotic shock survival of *E. coli* MJF465 cells (Figure 3.6). Since $MscS^{A286}$-mcpGFP is C-terminally tagged with mcpGFP and the addition of a C-terminal GFP tag has not been shown to affect MscS channel properties (Grigory Maksaev & Haswell, 2011), we expected MscS and $MscS^{A286}$-mcpGFP variants to behave similarly. $MscS^{L35A}$ (Malcolm et al., 2011), $MscS^{G113A}$ (Akitake et al., 2007; Belyy, Anishkin, et al., 2010; Boer et al., 2011b; Edwards et al., 2008), and $MscS^{D62N}$ (Boer et al., 2011b; Machiyama et al., 2009; Takeshi Nomura et al., 2008) all show reduced function during hypoosmotic shock compared to WT MscS without altering cell growth. Indeed, $MscS^{A286}$-mcpGFP variants containing these mutations did not show altered cell growth (data not shown). However, $MscS^{A286\ G113A}$-mcpGFP and $MscS^{A286\ D62N}$-mcpGFP showed no function during hypoosmotic shock (Figure 3.8A), a more severe defect than expected, though for MscSA286 D62N-mcpGFP this may have to do with relatively low expression (Figure 3.8B).

Both $MscS^{L86N\ I37N}$ (Machiyama et al., 2009; Takeshi Nomura et al., 2006) and $MscS^{F68N\ A51N}$ (Takeshi Nomura et al., 2006) lack detectable channel activity and

previously did not show function during hypoosmotic shock. Although the effects of MscS$^{L86N\ I37N}$ and MscS$^{F68N\ A51N}$ expression on cell growth was not previously evaluated, their comparable expression levels to WT MscS and higher gating thresholds of corresponding single mutants made us predict that neither mutant would impact *E. coli* growth. In addition, while the MscS$^{L86N\ L35N}$ variant has not previously been characterized, due to its similarity to MscS$^{L86N\ I37N}$, we predicted that both sets of mutations would have similar effects on MscSA286-mcpGFP behavior. Contrary to our predictions, both MscS$^{A286\ L86N\ I37N}$-mcpGFP and MscS$^{A286\ L86N\ L35N}$-mcpGFP functioned at comparable levels to MscSA286-mcpGFP during hypoosmotic shock (Figure 3.8A) and decreased cell growth (Figure 3.8C). However, in contrast to previous results (Figure 3.3B), in assays performed with MscS^{A286}-mcpGFP variants, MscS^{A286}-mcpGFP showed much lower function than MscS (30% vs 78%, respectively), potentially indicating lower expression levels, which may have played a role in the production of unexpected results.

In contrast to MscS^{A286}-mcpGFP, no MscS^{S58}-mcpGFP variants produced phenotypes in *E. coli* physiological assays that were significantly different from those of MscS^{S58}-mcpGFP (Figure 3.8D). This is not entirely unexpected, as S58 lies close to some of the point mutation sites and the insertion of mcpGFP in the small loop between TM1 and TM2 of MscS likely disrupts many normal interactions with the mutated residues. Based on these results in *E. coli*, we thus expected MscS^{S58}-mcpGFP variants to show similar signal changes during osmotic shock to MscS^{S58}-mcpGFP.

We next evaluated signal changes of select MscS^{S58}-mcpGFP and MscS^{A286}-mcpGFP variants during osmotic shock. This allowed us to test the idea that signal changes of sensor candidates during osmotic shock actually reflect channel dynamics, which should be altered by mutations to sensor candidates. We chose variants that had a range of effects on MscS^{A286}-mcpGFP behavior and that previously have been proposed to affect different stages of channel gating during osmotic shock: L35A, F68N A51N, G113A, and D62N. Both MscS$^{A286\ L35A}$-mcpGFP and MscS$^{A286\ F68N\ A51N}$-mcpGFP function similarly to MscS^{A286}-mcpGFP during osmotic shock, however, MscS$^{A286\ F68N\ A51N}$-mcpGFP also hinders cell growth. In contrast, both MscS$^{A286\ D62N}$-mcpGFP and MscS$^{A286\ G113A}$-mcpGFP fail to confer cell survival during hypoosmotic shock without affecting cell growth.

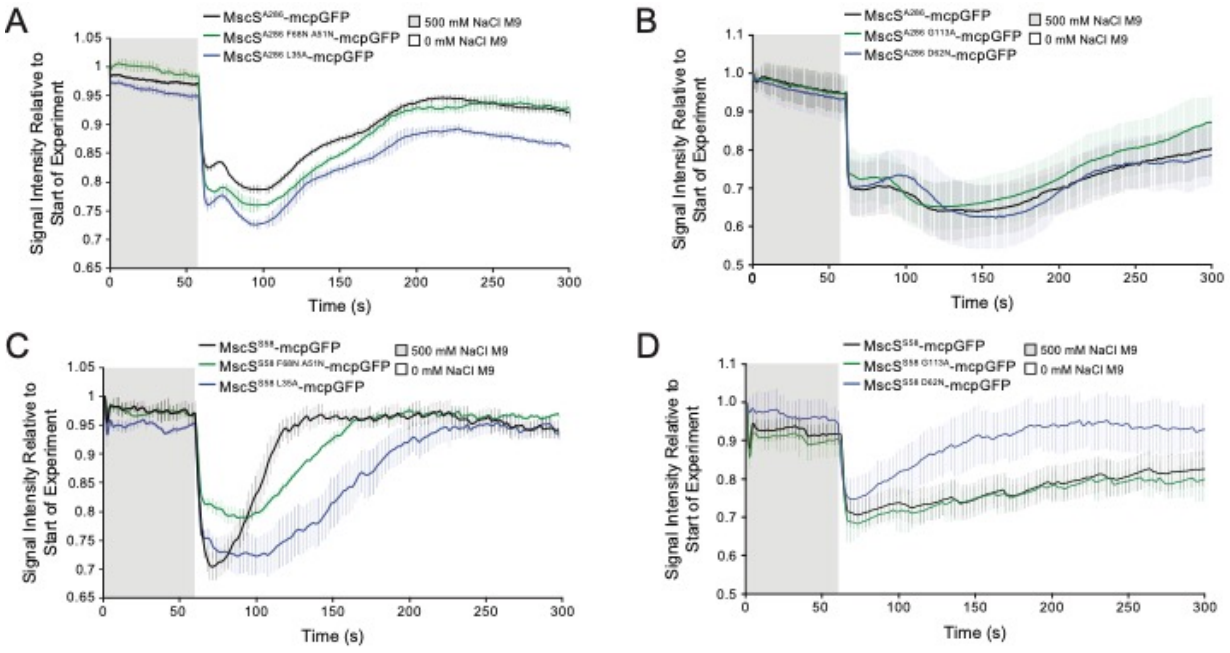

Figure 3.9. Dynamics of pre-shock signal recovery are altered for MscS^{S58}-mcpGFP variants, but not MscS^{A286}-mcpGFP variants. Media conditions for each time point are indicated by background color,

either gray for 500 mM NaCl M9 or white for 0 mM NaCl M9. Signal intensity is presented as relative to the start of each experiment and is the average ± standard deviation for measurements from multiple cells. (A) Signal intensity of FRAG-1 cells expressing either MscS^{A286}-mcpGFP, MscS$^{A286\ F68N\ A51N}$-mcpGFP, or MscS$^{A286\ L35A}$-mcpGFP in FRAG-1 cells during hypoosmotic shock. N = 122 cells, 112 cells, and 98 cells, respectively (B) Signal intensity of MscS^{A286}-mcpGFP, MscS$^{A286\ G113A}$-mcpGFP, or MscS$^{A286\ D62N}$-mcpGFP in FRAG-1 cells during hypoosmotic shock. N = 30 cells for each sensor candidate. (C) Signal intensity of MscS^{S58}-mcpGFP, MscS$^{S58\ F68N\ A51N}$-mcpGFP, or MscS$^{S58\ L35A}$-mcpGFP in FRAG-1 cells during hypoosmotic shock. N = 72 cells, 107 cells, and 34 cells, respectively. (D) Signal intensity of MscS^{S58}-mcpGFP, MscS$^{S58\ G113A}$-mcpGFP, or MscS$^{S58\ D62N}$-mcpGFP in MJF465 cells during hypoosmotic shock. N = 70 cells, 54 cells, and 39 cells, respectively.

MscS$^{S58\ F68N\ A51N}$-mcpGFP, MscS$^{S58\ L35A}$-mcpGFP, and MscS$^{S58\ D62N}$-mcpGFP show altered responses to hypoosmotic shock. We first examined the response of the MscS^{S58}-mcpGFP and MscS^{A286}-mcpGFP variant subset described above to single sustained hypoosmotic shocks (Figure 3.9). This allowed us to look for alterations in initial shock response and swelling by our sensor candidate variants, as well as later stages involving cell shrinking and recovery. We first examined responses of MscS^{A286}-mcpGFP variants in FRAG-1 cells, where expression of endogenous channels should prevent alterations in MscS^{A286}-mcpGFP activity from affecting osmotic shock response. Unexpectedly, despite the altered behavior displayed by MscS^{A286}-mcpGFP variants when hypoosmotic survival and cell growth were assessed, only minimal differences in signal change were observed. This suggests that MscS^{A286}-mcpGFP signal changes are not directly linked to channel dynamics or that changes in channel dynamics caused by mutations in MscS^{A286}-mcpGFP variants are not sufficient to alter sensor candidate response during hypoosmotic shock.

MscS$^{S58\ L35A}$-mcpGFP and MscS$^{S58\ F68N\ A51N}$-mcpGFP signal changes were examined in *E. coli* FRAG-1 cells during hypoosmotic shock. Both MscS$^{S58\ L35A}$-mcpGFP and MscS$^{S58\ F68N\ A51N}$-mcpGFP showed delayed signal recovery after shock while MscS$^{S58\ F68N\ A51N}$-mcpGFP also showed less signal change immediately upon shock compared to MscS^{S58}-mcpGFP (Figure 3.9C). These results thus suggest that mutations to MscS^{S58}-mcpGFP do alter sensor candidate response to osmotic shock, however, without any obvious effect on channel function in hypoosmotic shock plating assays and effect on cell growth it is unclear in what way MscSS58-mcpGFP function is altered in these variants. MscS$^{S58\ G113A}$-mcpGFP and MscS$^{S58\ D62N}$-mcpGFP signal changes during hypoosmotic shock were examined in MJF465 cells rather than FRAG-1 to attempt to create conditions in which inactivation of MscS was likely to occur, i.e. sustained, increased tension (Akitake et al., 2007; Buda et al., 2016). MscS^{S58}-mcpGFP and MscS$^{S58\ G113A}$-mcpGFP showed identical signal changes throughout hypoosmotic shock while MscS$^{S58\ D62N}$-mcpGFP showed faster recovery (Figure 3.9D), reversing the signal change caused immediate upon hypoosmotic shock. This may indicate rapid inactivation of MscS$^{S58\ D62N}$-mcpGFP, as expected for the D62N mutation, or other differences in MscS$^{S58\ D62N}$-mcpGFP and MscS^{S58} mcpGFP behavior not detected in hypoosmotic shock plating assays or cell growth measurements.

***E. coli* MJF465 cells expressing MscS$^{S58\ D62N}$-mcpGFP and MscS$^{A286\ D62N}$-mcpGFP show altered rates of signal recovery during cycling osmotic shocks.** We next tested the response of MscS^{S58}-mcpGFP, MscS^{A286}-mcpGFP, and variants to a series of alternating 20 s long hypoosmotic and hyperosmotic shocks (Figure 10). While

the immediate shock response did not vary between sensor candidates and variants (Figure 10), MscS$^{S58\ D62N}$-mcpGFP and MscS$^{A286\ D62N}$-mcpGFP showed altered signal recovery following shock. Signal from both MscS^{S58}-mcpGFP and MscS$^{S58\ D62N}$-mcpGFP shows the same amount of change immediately upon shock. However, after this MscS$^{S58\ D62N}$-mcpGFP signal recovers more slowly and to a lesser degree than signal of MscS^{S58}-mcpGFP (Figure 3.10B). MscS$^{A286\ D62N}$-mcpGFP also showed similar levels of signal change immediately upon each osmotic shock. However, MscS$^{A286\ D62N}$-mcpGFP signal recovery was more rapid and of larger magnitude than MscS^{A286}-mcpGFP signal recovery (Figure 3.10D). Thus, as with long hypoosmotic shocks, select sensor candidate variants deviate from parent sensor candidates in signal recovery rate rather than initial osmotic shock response. The D62N mutation is expected to cause rapid inactivation immediately upon tension application (Boer et al., 2011b), reversing the conformational change experienced during opening. The faster signal recovery of MscS$^{A286\ D62N}$-mcpGFP could be thus expected to result from rapid inactivation, if signal change during osmotic shock directly results from conformational changes of the channel. In contrast, MscS$^{S58\ D62N}$-mcpGFP shows a slower recovery rate than MscS^{S58}-mcpGFP, however, the presence of mcpGFP just four amino acids away from the D62N mutation site almost certainly would affect the impact of this mutation on channel behavior.

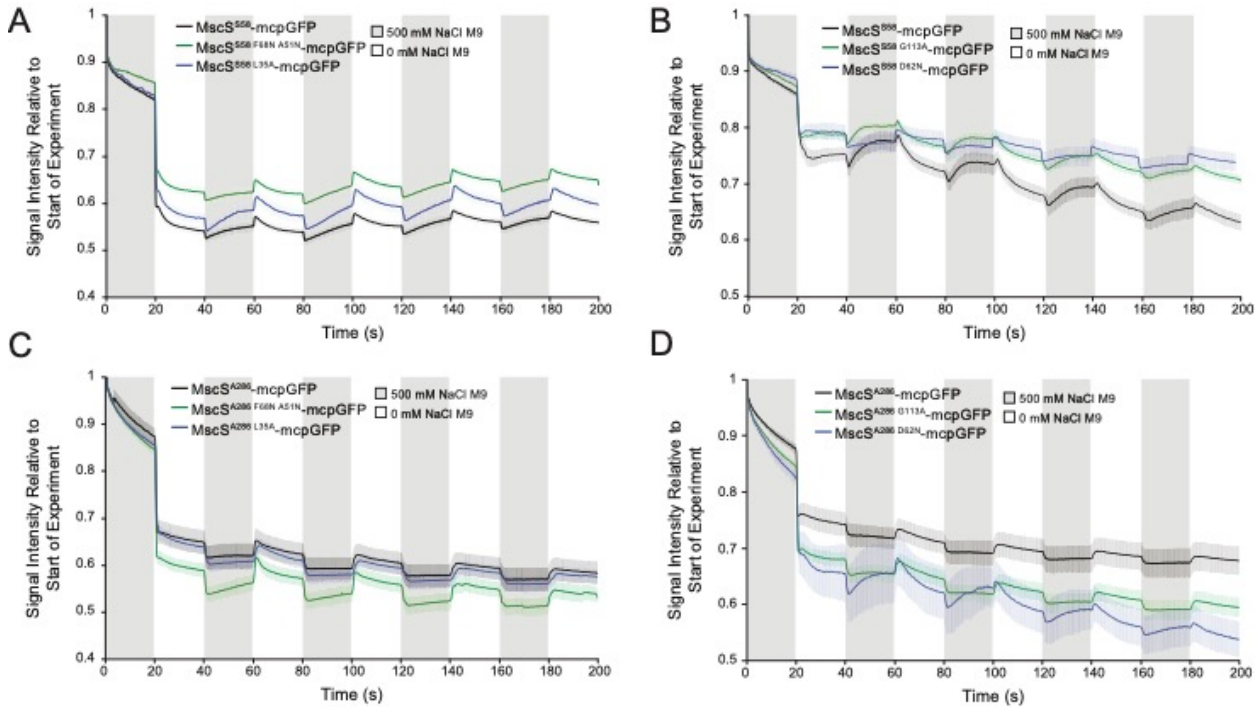

Figure 3.10. MscS$^{S58\ D62N}$-mcpGFP and MscS$^{A286\ D62N}$-mcpGFP show altered signal recovery during cycling osmotic shock. Media conditions for each time point are indicated by background color, either gray for 500 mM NaCl M9 or white for 0 mM NaCl M9. Signal intensity is presented as relative to the start of each experiment and is the average ± standard deviation for measurements from multiple cells. (A) Signal intensity of MscS^{S58}-mcpGFP, MscS$^{S58\ F68N\ A51N}$-mcpGFP, or MscS$^{S58\ L35A}$-mcpGFP in FRAG-1 cells during alternating 20 s hypoosmotic and hyperosmotic shocks. N = 88 cells, 52 cells, and 31 cells, respectively. (B) Signal intensity of MscS^{S58}-mcpGFP, MscS$^{S58\ G113A}$-mcpGFP, or MscS$^{S58\ D62N}$-mcpGFP in MJF465 cells during alternating 20 s hypoosmotic and hyperosmotic shocks. N = 88 cells, 65 cells, and 60 cells, respectively. (C) Signal intensity of MscS^{A286}-mcpGFP, MscS$^{A286\ F68N\ A51N}$-mcpGFP, or MscS$^{A286\ L35A}$-mcpGFP in FRAG-1 cells during alternating 20 s hypoosmotic and hyperosmotic shocks. N = 88 cells, 52 cells, and 31 cells, respectively. (D) Signal intensity of MJF465 cells expressing either MscS^{A286}-mcpGFP (85 cells), MscS$^{A286\ G113A}$-mcpGFP (63 cells), or MscS$^{A286\ D62N}$-mcpGFP (52 cells) during alternating 20 s hypoosmotic and hyperosmotic shocks.

TM1-mcpGFP and MscS^{S58}-mcpGFP show indistinguishable responses to cycling osmotic shock. We next created a control, TM1-mcpGFP, by fusing mcpGFP to the first TM helix of MscS after residue S58. We expected TM1-mcpGFP to be

minimally tension sensitive. MscS^{S58}-mcpGFP and TM1-mcpGFP in FRAG-1 cells subjected to 20 s cycling osmotic shocks showed similar signal intensity changes, both in terms of the degree of intensity change immediately upon shock and the pattern of signal recovery. This suggests that tension-driven conformational changes of MscS^{S58}-mcpGFP, which are likely very different than any that TM1-mcpGFP undergoes, are not likely the direct source of signal changes by MscS^{S58}-mcpGFP. Thus, it seems unlikely that signal intensity changes of our sensor candidates are directly due to changes in membrane tension, and may depend more on properties of mcpGFP than the MS channel portion of MscS^{S58}-mcpGFP and MscS^{A286}-mcpGFP.

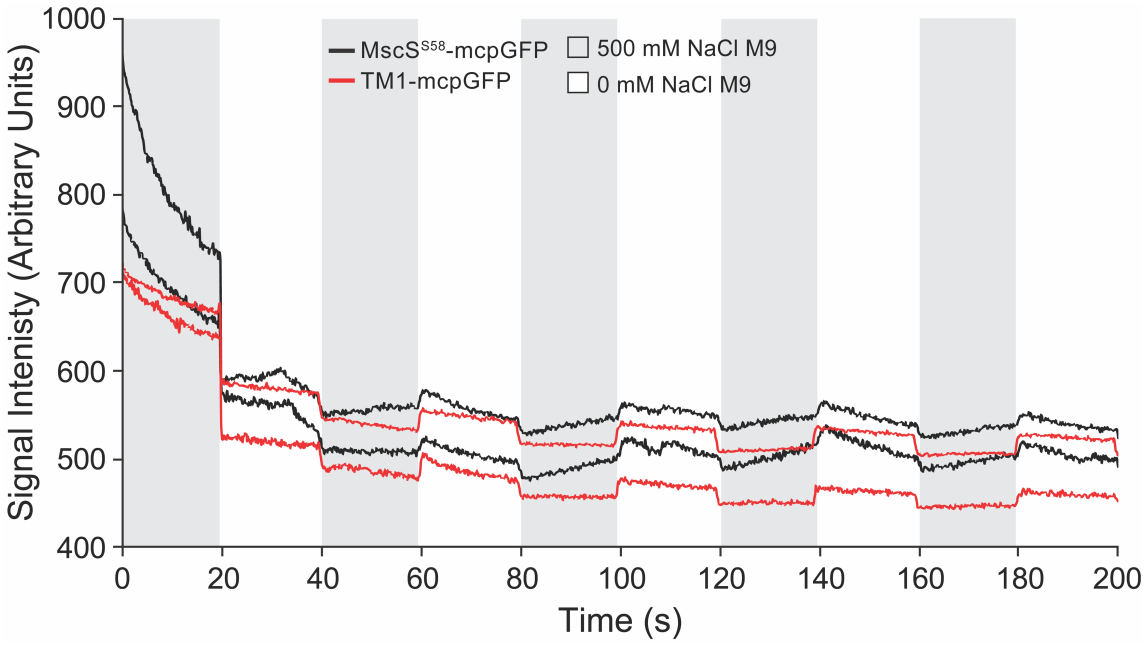

Figure 3.11. Signal intensities of *E. coli* FRAG-1 cells expressing MscS^{S58}-mcpGFP and TM1-mcpGFP show similar patterns and degrees of change during alternating osmotic shocks. Signal intensities, measured in arbitrary units, of cells expressing MscS^{S58}-mcpGFP (black) or TM1-mcpGFP (red) during alternating 20 s hypoosmotic and hyperosmotic shock. Each line represents the signal

intensity from a single cell. A gray background indicates when cells were exposed to 500 mM NaCl M9 media while a white background indicates when cells were exposed to 0 mM NaCl M9 media.

3.5 Discussion

Multiple lines of evidence suggest a potentially indirect or complex relationship between membrane tension and sensor candidate signal change. Our results suggest that MscS^{S58}-mcpGFP and MscS^{A286}-mcpGFP may indirectly report lateral membrane tension changes, as indicated by multiple lines of evidence. First and foremost, signal intensity changes of *E. coli* cells expressing TM1-mcpGFP and MscS^{S58}-mcpGFP undergoing alternating hypo- and hyperosmotic shocks were indistinguishable. While TM1-mcpGFP possesses a single TM helix and is thus predicted to be minimally tension sensitive, MscS^{S58}-mcpGFP clearly displays MS channel activity (Figure 3.4C) and thus tension-dependent conformational changes. Even if TM1 were to undergo some kind of tension-dependent conformational change, the drastically different structures of TM1-mcpGFP and MscS^{S58}-mcpGFP and the difference in mcpGFP attachment (one vs both sides) makes it seem unlikely that the two proteins would show identical signal changes during multiple types of osmotic shock. The lack of correlation between the level of tension sensitivity and signal intensity change during hypoosmotic shock thus argue against the ability of MscS^{S58}-mcpGFP to directly report membrane tension changes.

Second, the similarity in signal changes of cells expressing MscS^{S58}-mcpGFP and MscS^{A286}-mcpGFP during osmotic shock also suggests that these sensor candidates do not directly report membrane tension changes. MscS^{S58}-mcpGFP and MscS^{A286}-mcpGFP show very similar fluorescence intensity in cells undergoing osmotic

shock, with slight differences in the degree of signal intensity change immediately upon shock (Figure 3.7, 3.9-3.10). However, in physiological assays and electrophysiology, MscS^{S58}-mcpGFP and MscS^{A286}-mcpGFP show very different behavior, as MscS^{S58}-mcpGFP exhibits gain-of-function phenotypes (Figure 3.3A) and intermittent gating during electrophysiology experiments (Figure 3.4C) while MscS^{A286}-mcpGFP displays normal MscS behavior (Figure 3.3B, Figure 3.4A-B).

The different insertion locations of mcpGFP in MscS^{S58}-mcpGFP and MscS^{A286}-mcpGFP would also be expected to create dramatic differences in intensity changes during osmotic shock. In MscS^{S58}-mcpGFP, mcpGFP is located in the cytoplasmic loop between TM1 and TM2. Current models of MscS gating identify TM1-2 as the tension sensing paddle that directly responds to membrane tension (Vásquez et al., 2008), swinging out upon increasing tension increase to enable TM3 movement and removal of vapor lock residues L105 and L109 from the pore (Bass et al., 2002). In addition, TM1 and TM2 separately engage in multiple interactions with other MscS domains (Belyy, Anishkin, et al., 2010; Koprowski et al., 2011; Edwards et al., 2005) and the lipid bilayer (Malcolm et al., 2011; T. Rasmussen et al., 2019; Reddy et al., 2019), likely causing additional changes in forces affecting mcpGFP conformation. In contrast, in MscS^{A286}-mcpGFP, mcpGFP is only attached to the C-terminus of MscS and is anchored by a single point, eliminating many potential mechanisms for transferring conformational changes to mcpGFP.

Third, multiple MscS^{A286}-mcpGFP variants that alter channel behavior in osmotic shock assays and impact on cell growth do not show altered signal changes during

osmotic shock (Figure 3.8-3.10). While MscS^{A286}-mcpGFP shows normal MscS channel function, does not affect growth, and provides osmotic shock protection, MscS$^{A286\ L86N\ I37N}$-mcpGFP and MscS$^{A286\ L86N\ L35N}$-mcpGFP show gain-of-function phenotypes (Figure 3.8C) and MscS$^{A286\ F68N\ A51N}$-mcpGFP, MscS$^{A286\ D62N}$-mcpGFP, and MscS$^{A286\ G113A}$-mcpGFP show loss-of-function phenotypes (Figure 3.8A). Assuming that signal intensity is directly related to channel conformation, we expected that signal changes of each of these MscSA286-mcpGFP variants would differ from that of MscSA286-mcpGFP during osmotic shock. Unexpectedly, only signal changes of MscS$^{A286\ D62N}$-mcpGFP signal deviated from those of MscS^{A286}-mcpGFP and only during alternating hypo- and hyperosmotic shocks (Figure 3.10D). This suggests a lack of direct connection between MscSA286-mcpGFP channel activity and signal change. Alternatively, changes in MscSA286-mcpGFP channel behavior could be insufficient to alter signal response despite direct dependency. For MscS^{S58}-mcpGFP, *E. coli* physiological assays did not indicate additional mutations had any effect of gating characteristics, potentially because of the existing gain-of-function behavior or disruptions to the normal functions of the mutated residues. Thus, while MscS^{S58}-mcpGFP variants did exhibit differences in signal response during osmotic shock compared to MscS^{S58}-mcpGFP (Figure 3.9C-D, Figure 3.10A-B), it is difficult to draw conclusions about the source of such changes without further analysis of MscS^{S58}-mcpGFP variant channel behavior.

Based on the reasoning described above, it appears that mcpGFP signal responds to osmotic shock in *E. coli* independently of which specific protein it is attached to. Ultimately, mcpGFP signal intensity appears to be sensitive to changes in

cellular characteristics other than membrane tension that change during osmotic shock. Such changes may include concentrations of various ions and solutes, pH, membrane potential, and the level of macromolecular crowding, and are discussed further below.

Comparison size and signal changes during cycling osmotic shock enables predictions about possible drivers of sensor candidate response. In our experiments, to test sensor candidate responses to osmotic shock, transformed *E. coli* cells were grown in 500 mM NaCl M9 media for a period of hours. This allowed cells time to acclimate, during which they would accumulate intracellular solutes like potassium, glutamate, and, after longer periods of time, betaine, proline, and trehalose in order to maintain outward turgor pressure (Booth, 2014; Bremer & Krämer, 2019). This produces cells whose cytoplasms are highly concentrated with solutes, rendering them especially sensitive to hypoosmotic shock.

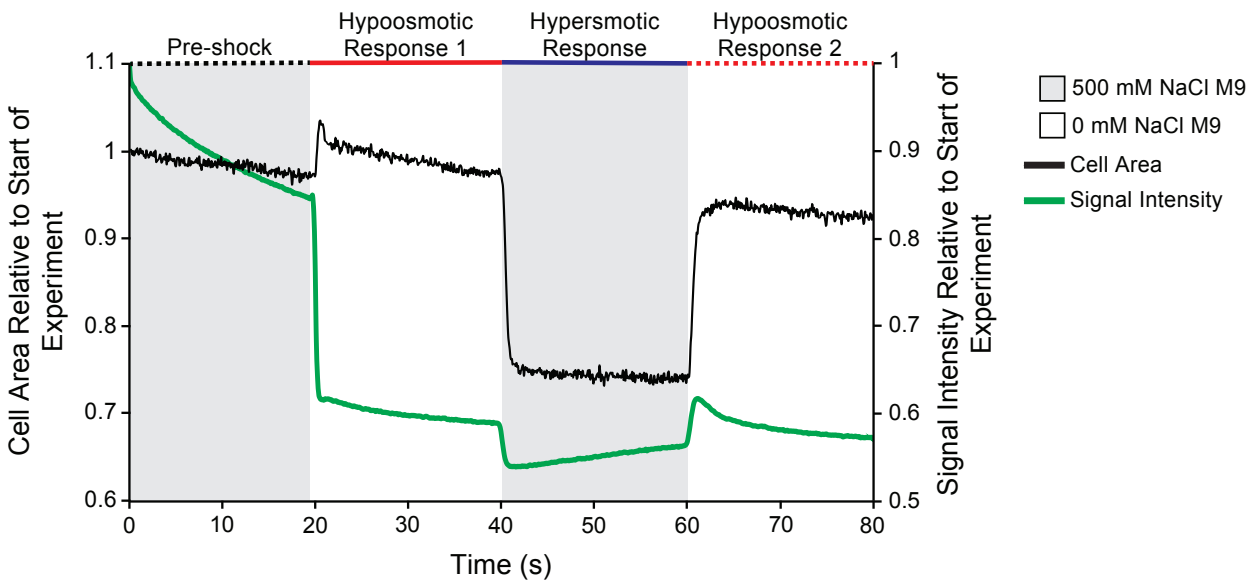

Figure 3.12. Comparison of cell size and MscSA286-mcpGFP signal changes in *E. coli* FRAG-1 cells during osmotic shock. Cell area (black line) and MscS^{A286}-mcpGFP signal intensity (green line) are shown relative to the start of the experiment as cells transition between 500 mM NaCl M9 (gray background) and 0 mM NaCl M9 media (white background). The three types of shock response and pre-shock values are indicated by lines at the top of the graph corresponding to time over which the response occurred: pre-shock (dashed black line), hypoosmotic response 1 (solid red line), hyperosmotic response (solid blue line), and hypoosmotic response 2 (dashed red line).

We can then speculate about what happens to these cells during alternating hypo- and hyperosmotic shocks in order to identify cellular conditions that are likely to change during shock, with guidance from our experiments (Figure 3.12) and previous work (Boer et al., 2011b; Rojas et al., 2014; Rowe et al., 2014; Wood, 2011; Buda et al., 2016). The initial hypoosmotic shock will cause minor cell swelling, activating MS ion channels and releasing solutes while slightly decreasing the amount of macromolecular crowding. Next, when a hyperosmotic shock is applied, these cells will dramatically shrink, greatly increasing the amount of macromolecular crowding and solute concentration, with some solute accumulation. The following hypoosmotic shock will

again cause cell swelling to a similar volume to that following the previous hypoosmotic shock, decreasing levels of cytoplasmic solutes, molecular crowding, and membrane curvature. The first hypoosmotic shock also may represent a unique case due to the high solute content of cells and high pre-shock volume, while subsequent hypoosmotic shocks act on small, shriveled cells. These additional osmotic shocks mainly involve water flux in and out of the cell due to the short interval between shocks (Rojas et al., 2014) and the use of minimal M9 media, reducing solute accumulation during hyperosmotic shock.

Based on the above description of alternating hypo- and hyperosmotic shocks, if membrane-tethered mcpGFP is sensitive to one particular element of its cellular environment, we would expect hypo- and hyperosmotic shocks to always produce opposing changes in mcpGFP fluorescence intensity. However, as shown in Figure 3.12, this is not the case. Upon the first hypoosmotic shock in a given experiment, the fluorescence intensity of cells expressing membrane-tethered mcpGFP plunges by up to 30%. Hyperosmotic shock then causes a more minor decrease in fluorescence intensity, which is reversed by the following hypoosmotic shock. In contrast, while the degree of size change between different osmotic shocks varies, hypoosmotic shock always increased cell size while hyperosmotic shock decreased cell size. This suggests that membrane-tethered mcpGFP may respond to multiple stimuli, one of which dominates fluorescence intensity changes upon the initial hypoosmotic shock and the others more greatly influencing subsequent shock responses.

Potential influences on sensor candidate response to osmotic shock include pH and macromolecular crowding. There are multiple potential influences in the cell on mcpGFP fluorescence. GFP and many of its circularly permuted GFP variants exhibit two excitation maxima depending on pH, ~395 nm and 475 nm (De Michele et al., 2013; Tsien, 1998), and cpGFP variants often exhibit enhanced sensitivity to environmental parameters such as pH and temperature (Kostyuk et al., 2019). In our experiments, we excited GFP using 470-510 nm of light in our experiments and therefore only looked at GFP emission resulting from one of two pH-dependent excitation maxima. It is therefore possible that some of the mcpGFP signal changes we saw during our experiments are due to pH-dependent shifts in the mcpGFP excitation maxima rather than conformation changes. Such pH changes during osmotic shock would potentially be larger near the membrane surface, rendering membrane-tethered mcpGFP especially sensitive to such changes. When signal of cytoplasmic non-circularly-permuted GFP was measured during osmotic shock, only minimal changes in intensity were observed (data not shown). This possibly supports the sensitivity of membrane-localized GFP or demonstrates differences in pH sensitivity between GFP variants and motivates examination of pH changes during osmotic shock and the testing of additional fluorescent reporters for our sensor candidates.

Changes in the solvent accessibility of the cpGFP fluorophores can also impact signal intensity (Akerboom et al., 2009), which can be independent of the cpGFP response to conformational changes in the stimulus-sensing scaffold it is attached to (Ast et al., 2015). For membrane-tethered mcpGFP in *E. coli* cells undergoing osmotic

shock, such changes could occur upon membrane curvature or movement of mcpGFP towards and away from the membrane bilayer. Macromolecular crowding, which likely dramatically varies during osmotic shock (Cuevas-Velazquez & Dinneny, 2018; Rowe et al., 2014), is another possible source of solvent access modulation and may also alter mcpGFP fluorescence through physically changing mcpGFP conformation.

Considerations for future tension sensor development include careful consideration of fluorescent reporter and assessment of non-tension influences. Addressing the shortcomings of our tension sensor design can focus on changing the fluorescent reporter, tension-sensing scaffold, or thinking beyond a genetically-encoded membrane tension sensor. Beyond the immediate issues described above, mcpGFP is intensiometric and is thus less than ideal for quantifying membrane tension. Replacement of mcpGFP with either mutagenized mcpGFP that produces ratiometric rather than intensiometric emission changes (Ast et al., 2015) or a dual-protein reporter like Matryoshka, in which one of the two fluorescent proteins acts as an insensitive reference (Ast et al., 2017), can both allow for quantification and help distinguish between artifacts that impact all fluorescence equally (for example, protein degradation) and stimulus-specific emission changes. As for alternative tension-sensing scaffolds, MS channels besides MscS are one potential choice and, depending on the specific MS channel, may offer advantages in terms of expression and trafficking in other cell types and organisms. Protein domains that respond to changes in membrane properties, such as curvature-sensing BAR domains (Stanishneva-Konovalova et al., 2016), are another potential scaffold as curvature is related to tension, although the relationship between

membrane tension, the exact membrane property measured, and the desired spatial scale of measurements must be considered. Alternatively, the recent successes with chemically synthesized FliptR (Colom et al., 2018), including the first steps of specific membrane targeting (Goujon et al., 2019), and nanoparticles (Lay et al., 2017) indicate the potential for non-protein based force sensors, though ease and specificity of integration into living organisms remains a challenge.

The importance of a membrane tension sensor that can be used to monitor membrane tension *in vivo* in real time is hard to overstate (Colom et al., 2018; W. Li et al., 2018). However, as demonstrated in the experiments presented above, creation of a genetically-encoded fluorescence-based sensor is fraught with potential pitfalls and complicating factors, especially during situations in which major cellular changes are occurring. Future efforts to develop a membrane tension sensor must take care to comprehensively evaluate sensor properties to dissect true tension reporting from influence of other factors and to do so in a variety of systems to qualify the conditions and situations ideal for sensor use.

3.6 Relative Contributions

Emma January assisted with creation of the initial set of sensor candidates. Dr. Grigory Maksaev contributed the majority of data for Figure 3.4. Ryan Richardson performed immunoblotting and Coomassie staining shown in Figure 3.2 and generated sensor candidate point mutants and all data used for Figure 3.8. Angela Schlegel performed the remainder of all experiments, created figures, and wrote this chapter.

Chapter 4: Analyzing plant mechanosensitive ion channels expressed in giant *E. coli* spheroplasts by single-channel patch-clamp electrophysiology

Published as:

A. M. Schlegel, E. S. Haswell (2020). Analyzing plant mechanosensitive ion channels expressed in giant *E. coli* spheroplasts by single-channel patch-clamp electrophysiology. *Methods in Cell Biology*. https://doi.org/10.1016/bs.mcb.2020.02.007

4.1 Abstract

Plants possess numerous ion channels that respond to a range of stimuli, including small molecules, transmembrane voltage, and mechanical force. Many in the latter category, known as mechanosensitive (MS) ion channels, open directly in response to increased lateral membrane tension. One of the most effective techniques for characterizing ion channel properties is patch-clamp electrophysiology, in which the current through a piece of membrane containing ion channels is measured. For MS channels, this technique enables the measurement of key channel properties such as

tension sensitivity, conductance, and ion selectivity. These characteristics, along with the phenotypes of genetic mutants, can help reveal the physiological roles of a particular MS channel. In this protocol, we provide detailed instructions on how to study MS ion channels using single-channel patch-clamp electrophysiology in giant *E. coli* spheroplasts. We first present an optimized method for preparing giant spheroplasts, then describe how to measure MS channel activity using patch-clamp electrophysiology and analyze the resulting data. We also provide recommended equipment lists, set-up schematics, and useful conventions.

4.2 Introduction

Plants possess a wide variety of ion channels that impact nearly all aspects of their lives, from development and reproduction to homeostasis and stress response (Hedrich, 2012). Ion channels are present in most, if not all, membranes of plant cells (Carraretto et al., 2016; Hedrich, 2012) and can be activated by stimuli including membrane potential (Jegla et al., 2018), chemical ligands (Dietrich et al., 2010), and mechanical force (Eric S. Hamilton et al., 2015). Channels activated by mechanical force, called stretch-activated or mechanosensitive (MS) channels, include those directly activated by increased lateral membrane tension and those activated indirectly via tethers to other cellular components (Charles D. Cox et al., 2019).

Multiple families of MS ion channels in plants have been identified, either through genetic screens (Mid1-Complementing Activity (MCA) (Nakagawa et al., 2007), reduced hyperosmolality-induced $[Ca^{2+}]_i$ increase (OSCA) (Yuan et al., 2014), Piezo (Z. Zhang et

al., 2019)), or based on homology to known bacterial or animal channels, (MscS-Like (MSL) (Pivetti et al., 2003) and two-pore K^+ (TPK) (Czempinski, 1997; Gobert et al., 2007)). To date, all known plant MS families except the Mid1-Complementing Activity (MCA) proteins show homology to proteins in other eukaryotes and/or prokaryotes, although no mechanosensitive domain in common between MS channel families has been identified.

OSCA, MCA, and a subset of MSL channels localize to the plasma membrane (E. S. Hamilton et al., 2015; Eric S. Hamilton & Haswell, 2017; Haswell et al., 2008; Yuan et al., 2014; M. Zhang et al., 2018; G. Maksaev & Haswell, 2012; Murthy et al., 2018), TPK channels localize to the vacuolar membrane (Maathuis, 2011), and some MSL channels localize to the inner mitochondrial membrane or inner chloroplast membrane (C. P. Lee et al., 2016; Haswell & Meyerowitz, 2006). In terms of function, plant MS ion channels and channel candidates participate in processes such as Ca^{2+} uptake, hypoosmotic shock response (Kurusu et al., 2012; Mori et al., 2018; Yamanaka et al., 2010), osmotic homeostasis (E. S. Hamilton et al., 2015; Yuan et al., 2014; Veley et al., 2012; Maathuis, 2011), pathogen response (Z. Zhang et al., 2019), redox regulation (C. P. Lee et al., 2016), and cell death signaling (Veley et al., 2014). However, confirmation of MS channel activity or information about physiological function is lacking for many candidate plant MS channels (Eric S. Hamilton et al., 2015).

One technique used to evaluate and characterize MS channel activity is patch-clamp electrophysiology. During this procedure, cells are placed in buffer and a section of membrane from one cell (a “patch”) is electrically and physically isolated using a thin,

pulled glass “patch pipette” (Figure 1). A piece of chlorinated silver wire inside the patch pipette, called the command electrode, controls (“clamps”) the electric potential of the patch, which is measured relative to the electric potential of the ground electrode, an Ag/AgCl pellet present in the bath buffer. This electric potential established by the command electrode is referred to as the pipette potential. Pressure applied to the membrane patch through the patch pipette using a pump will increase lateral membrane tension and open, or “gate”, any embedded MS ion channels. The resulting ion flow is detected by the command electrode and is measured in reference to the ground electrode. The resulting current “traces” allow channel activity to be identified and channel characteristics like conductance, selectivity, gating tension, and voltage sensitivity to be measured.

Multiple patch-clamp configurations are commonly used, but all involve the formation of a high-resistance Giga-Ohm seal between the patch pipette and the cell membrane. In the inside-out excised patch configuration, often preferred for MS ion channels, a seal is first formed between the patch pipette and an intact cell (Figure 1). The membrane outside the pipette is then removed, leaving a single patch of membrane inside the patch pipette. This configuration allows for complete control of the membrane environment, removes the influence of other cellular components, and enables dramatic alterations of membrane tension through small changes in applied pressure. However, if channel mechanosensitivity requires cellular components or if channel expression is low, the cell-attached or whole-cell patch configurations may be more appropriate.

A few plant MS ion channels from the families listed above have been characterized by patch-clamp electrophysiology in native membranes, including those localized to the plasma membrane (E. S. Hamilton et al., 2015; Haswell et al., 2008) and vacuolar membrane (Maathuis, 2011). However, MS channels of interest are often expressed in native membranes at relatively low levels, making precise analysis of single-channel activity difficult. Additionally, while enzymatic removal of the cell wall enables easy access to the plasma membrane, it is extremely technically challenging to isolate inner organellar membrane patches that remain stable enough for analysis, making analysis of organellar MS channels in native environments difficult. Analysis of chloroplast ion channels requires swollen thylakoids or, in most cases, the incorporation of thylakoid membranes in liposomes or artificial lipid bilayers (Pottosin & Dobrovinskaya, 2015). In contrast, patching of mitochondrial inner membranes has proven difficult due to the small size of many plant mitochondria (Carraretto et al., 2016; De Marchi et al., 2010).

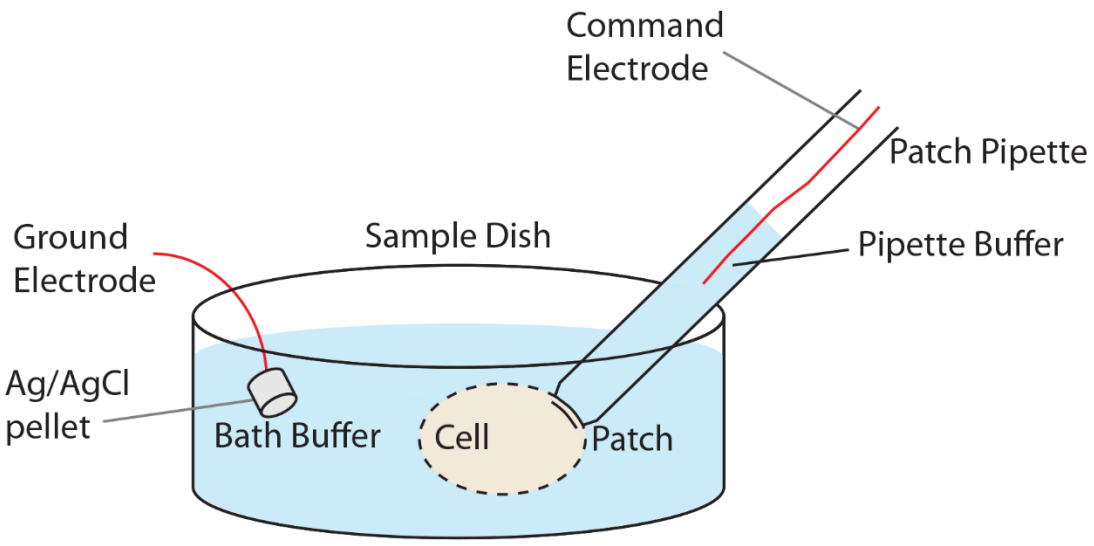

Figure 4.1. Overview of patch-clamp electrophysiology. A Giga-Ohm seal is formed between a glass patch pipette and a section of membrane (a "patch) from a cell or organelle. Application of stimuli such as pressure to the patch opens embedded ion channels, facilitating the flow of ions between the pipette buffer and either the cellular environment or bath buffer. This ion flow is measured by the command electrode (red line) relative to the ground electrode (gray cylinder) and is reported as current. To obtain the inside-out patch configuration, a seal is first made with an intact cell (dashed line). The portion of the cell outside the patch pipette is then removed, leaving just a patch of membrane inside the patch pipette (double line). The cytoplasmic face of this membrane patch faces the bath buffer while the extracellular face of the membrane patch faces the pipette buffer.

Heterologous expression systems for analyzing plant MS channels by patch-clamp electrophysiology are attractive alternatives to native membrane systems. Some heterologous expression systems lack MS channels, making identification of the channel of interest much easier than in native membranes. MS channels can often be expressed at high levels in heterologous systems, increasing the likelihood of obtaining reproducible, statistically meaningful data. For plant MS channels, useful heterologous systems include *Xenopus laevis* oocytes (Furuichi et al., 2012; G. Maksaev & Haswell, 2012), HEK cells (Murthy et al., 2018), and human 293F cells (M. Zhang et al., 2018). In

our hands, giant *E. coli* spheroplasts have proven to be an effective heterologous system for the analysis of plant mitochondrial MS channels.

While *E. coli* cells are too small to patch, giant *E. coli* spheroplasts are easily made, manipulated, and patched. Giant *E. coli* spheroplasts are produced by first preventing cell division while permitting cell growth, then destroying the outer membrane and cell wall (Birdsell & Cota-Robles, 1967; Martinac et al., 2013). Giant *E. coli* spheroplasts can be handily patched and offer multiple advantages as they enable tight control of expression levels, easy production, backgrounds lacking native MS channels, and can be stored for extended periods of time at -80°C. They also lack the maintenance requirements associated with *Xenopus* oocytes and mammalian cell lines.

This protocol describes our approach to characterizing plant MS ion channels expressed in giant *E. coli* spheroplasts using single channel patch-clamp electrophysiology. We first describe spheroplast preparation. Next, useful conventions for interpreting and presenting electrophysiology data are provided, followed by descriptions of equipment and procedures for patch-clamp electrophysiology and related data analysis. This protocol is intended to be a resource for cell biologists new to electrophysiology that are interested in studying MS ion channels in *E. coli* and other systems.

4.3 Methods

4.3.1. Spheroplast Preparation

Multiple protocols for the production of giant *E. coli* spheroplasts have been described (Dworsky, 1976; Kikuchi et al., 2015; Martinac et al., 2013; Renner & Weibel, 2011; Sun et al., 2014); the protocol below is modified from (Martinac et al., 2013). In this procedure, *E. coli* cells transformed with DNA constructs that encode a channel of interest are grown in the presence of cephalexin, which prevents cell division without affecting cell growth. Expression of the channel is induced during the latter part of cephalexin treatment. The resulting elongated *E. coli* cells ("snakes") are then treated with lysozyme and EDTA, which dissolve the cell wall and disrupt the outer membrane, resulting in giant, round *E. coli* spheroplasts.

When performing patch-clamp electrophysiology with giant *E. coli* spheroplasts, it is important to choose the *E. coli* strain and expression system that are optimal for your experimental goals. The *E. coli* strain MJF641 lacks all seven native MS ion channels genes (*mscL*, *mscS*, *mscK*, *ybdG*, *ynaI*, *ybiO*, and *yjeP* (Edwards et al., 2012)), providing a mechanically silent background for study and ensuring that any mechanically activated channel activities are from a heterologously expressed channel. This strain is thus ideal for studying MS channels whose channel properties are unknown. The MJF611 strain, which lacks all channels but MscL, is used for measuring MS ion channel tension sensitivity (Edwards et al., 2012) (*see* Note 1).

There can be multiple difficulties in analyzing plant MS channels in giant *E. coli* spheroplasts, including low expression levels and channel toxicity. The use of lysogenized *E. coli* cells helps address both of these issues. The genome of a λDE3 lysogenized cell contains an IPTG-inducible gene encoding T7 RNA polymerase, which in our hands enables these cells to express target genes driven by the T7 promoter at levels higher than target genes driven by IPTG-inducible promoters. In addition, this system tightly represses target gene transcription in the absence of inducer, which is especially useful for controlling toxic effects of channels and channel mutants.

The proper subcellular localization and folding of plant MS channels in *E. coli* is also a concern. The presence of eukaryotic targeting sequences can interfere with localization of channels to the *E. coli* plasma membrane, so expression of a channel both with and without targeting sequences should initially be tested. A GFP tag is a simple and effective way to check for expression and localization; however, protein tags can potentially interfere with channel function, so it is also useful to compare the activity of tagged and untagged channels.

Equipment

Shaking incubators capable of maintaining 37°C and 42°C with 250 rpm and 180 of shaking, respectively

Materials

Chemically competent λDE3 lysogenized *E. coli* cells, either strain MJF611 or MJF641 (Edwards et al., 2012)

DNA constructs in the pET300 vector, which confers carbenicillin resistance. For each batch of spheroplasts, you will need an empty vector control, constructs encoding the channel of interest, and a positive control (*see* Note 2).

14 mL culture tubes, sterile

250 mL flasks, autoclaved

Sterile LB-agar plates with 100 µg/mL carbenicillin

Liquid LB media, autoclaved

Cephalexin hydrate (Sigma #C4895), 10 mg/mL in water, 0.22 µm filter-sterilized

Lysozyme from chicken egg white (Sigma #L6876), 5 mg/mL in water

Deoxyribonuclease I (DNase I) from bovine pancreas (Sigma #DN25), 5 mg/mL in water (*see* Note 3)

1 M $MgCl_2$, autoclaved

1 M Tris-HCl, pH 7.2, autoclaved

0.125 M EDTA, pH 8.0, autoclaved

0.8 M sucrose, 0.22 µm filter-sterilized

Stop solution: 0.68 M sucrose, 19 mM $MgCl_2$, 9.5 mM Tris-HCl pH 7.2, 0.22 µm filter-sterilized

Dilution solution: 0.78 M sucrose, 1 mM $MgCl_2$, 1 mM Tris-HCl pH 7.2, 0.22 µm filter-sterilized

Procedure

Day 1

1. Transform cell strains with DNA constructs. Grow on LB-agar plates with 100 µg/mL carbenicillin overnight at 37°C.

Day 2

2. Add 10 colonies to 3 mL LB with 100 µg/mL carbenicillin in a 14 mL culture tube. Shake overnight at 37°C, 250 rpm.

Day 3

3. Add 125 µL overnight culture to 5 mL LB + 100 µg/mL carbenicillin in a 14 mL culture tube and shake at 37°C, 250 rpm until it reaches an OD_{600} of 0.4-0.5, about 1.5 h.
    - Meanwhile:
        - Make fresh cephalexin solution by dissolving cephalexin powder in ultrapure H_2O and filtering using a 0.22 µm filter. For ease of filtration, the initial volume of cephalexin solution should be at least 2 mL.

- Warm one 250 mL flask containing 27 mL sterile LB to 37°C for each sample.

4. Once an OD of 0.4-0.5 is reached, add 3 mL of the culture to the pre-warmed flask, then add 180 µL cephalexin (final concentration 60 µg/mL cephalexin). Shake cultures at 42°C, 180 rpm until *E. coli* cells have reached 50-75 µm long. Next, add IPTG to a final concentration of 1 mM and shake at 42°C, 180 rpm for an additional hour (*see* Notes 4-5). Cell size should be estimated during shaking by examining cells every 15 min starting at the moment of cephalexin addition. Place a 2-3 µL aliquot of culture on a microscope slide, cover with a coverslip, then examine cells on a light microscope with a 100x objective.
5. Decant each culture into a 50 mL conical tube and store overnight at 4°C (optional). This overnight incubation can also be skipped and the protocol continued starting from step 6 below.

Day 4

6. Prepare fresh DNase I, lysozyme, stop solution, and dilution solution and store all on ice.
7. Remove cultures from 4°C, spin at 3000 x g for 5 min at room temperature, and decant the supernatant, taking care not to lose the pellet.
8. Gently resuspend the pellet by pipetting 2.5 mL 0.8 M sucrose down the side of the tube and gently swirling the tube.

9. Add the following components to each sample in the order listed below, swirling after each addition. Incubate the reaction at room temperature for the desired reaction time. Start with 5 and 7.5 minute reaction incubation times, then optimize (*see* Note 6).
    - 150 µL 1 M Tris-HCl, pH 7.2
    - 120 µL 5 mg/mL lysozyme
    - 50 µL 5 mg/mL DNase I
    - 150 µL 0.125 M EDTA, pH 8.0
10. Add 1 mL stop solution to each reaction and swirl to mix, then place on ice.
11. Add 3.5 mL dilution solution to each sample and swirl to mix. Place 350 µL aliquots of sample into chilled tubes then store at -80°C. Spheroplasts cannot be re-frozen after thawing, so any unused thawed spheroplasts will have to be discarded (*see* Note 7).

Notes

1. During patching, membrane tension is increased by the application of suction to the membrane. The exact relationship between suction and tension depends on patch geometry and is directly proportional to patch radius, which is technically difficult to measure and varies between patch pipettes. Thus, the tension sensitivity of MS channels expressed in giant *E. coli* spheroplasts is often described relative to an internal control to enable patch-to-patch comparisons

(Blount et al., 1996). MscL exhibits a large conductance and high, near-lytic gating tensions, making it an ideal internal control (S. I. Sukharev et al., 1994).

2. A strain expressing *E. coli* MscS or *A. thaliana* MSL1 (Edwards et al., 2005, 2008; C. P. Lee et al., 2016; Levina, 1999), will serve as an excellent positive control. An empty vector (negative control) should be included.
3. For the most efficient production of giant spheroplasts, cephalexin, DNase I, and lysozyme solutions should be made just prior to use.
4. As growth progresses in the presence of cephalexin, cells will eventually reach lengths at which they become fragile and appear to break apart or dissolve. If this occurs, immediately initiate induction by adding IPTG.
5. The ideal length and starting point of induction must be empirically determined for each channel/strain combination. Induction for 30 min or 1 h with 1 mM IPTG (final concentration) are recommended starting conditions.
6. To establish an optimal reaction time for the samples, perform the spheroplasting reaction with a single sample, stop the reaction, and place 2-3 µL sample on a microscope slide, laying a cover slip on top. Examine on a microscope equipped with a 100x objective; multiple spheroplasts with intact membranes should be visible on the microscope slide. The presence of very few or no spheroplasts indicates an insufficient reaction time, while the lack of intact spheroplasts and the presence of many broken cells and spheroplasts indicates that the reaction has proceeded for too long.

7. While concentrated spheroplast preparations can be useful for patching, they also contain increased amounts of debris that can clog the patch pipette. The optimal balance between the relative concentrations of spheroplasts and debris (and therefore the amount of dilution solution used) must be empirically determined for each spheroplast preparation.

4.3.2. Patching MS channels in giant *E. coli* spheroplasts

This protocol is divided into the four major tasks involved in analyzing MS channel activity by patch-clamp electrophysiology: equipment preparation (setting up an electrophysiology rig and preparing patch pipettes), patch acquisition, data acquisition, and data analysis. First, we describe conventions and equations that are useful to know for analyzing, reporting, and understanding patch-clamp electrophysiology data. For a more comprehensive overview of patch-clamp electrophysiology, see (Molecular Devices, 2012).

Membrane potential is defined as the electrical potential inside the cell relative to the outside of the cell and is usually reported in millivolts (mV). This is shown in the following equation in which $V_{membrane}$ represents membrane potential, $V_{outside}$ represents the electric potential outside of the cell, and V_{inside} represents the electric potential inside the cell:

$$V_{membrane} = V_{outside} - V_{inside}$$

In patch-clamp electrophysiology, this convention still holds. However, the particular patch configuration used will dictate whether the pipette or bath side of the membrane corresponds to the outside of the cell and, thus, whether the pipette potential is the opposite or the same sign (positive or negative) as the potential of the membrane under study.

For the inside-out patch configuration, the cytoplasmic leaflet of the membrane faces the bath buffer and the ground electrode while the extracellular leaflet faces the pipette buffer and the command electrode (Figure 1). This means that the reference point for electric potential measurements is reversed when comparing the membrane and pipette potentials, therefore the pipette potential and the membrane potential have equal magnitudes but opposite signs.

Measurements of single channel current at specific membrane potentials can be used to calculate other channel properties like conductance. Conductance (C), current (I), potential (V), and resistance (R) are all related simply using Ohm's law, $V = IR = I/C$ or $C = I/V$. The unit of conductance is the siemen (S). MS channel conductances are typically reported in picosiemens (pS) and calculated using membrane potential in millivolts (mV) and current (I) in picoamps (pA).

Equipment

Anti-vibration table with Faraday cage: Technical Manufacturing Corporation, system 63-533

Inverted light microscope with 60x and 100x lenses: Olympus CKX41 and an Olympus IX71

Power strip (noise filter/surge suppressor): Isobar 12 Ultra, Tripp-Lite

Amplifier: Axon Axopatch 200B (V-clamp mode, V_m headstage, low pass Bessel filter at 5 kHz, gain adjusted as needed)

Digitizer: Axon CNS Digidata 1440A or 1550A (Molecular Devices)

Pressure control: HSPC-1 High Speed Pressure Clamp and PV-Pump (ALA Scientific Instruments)

Small fan (to cool PV-Pump)

Headstage: Axon Instruments Cellular Neuroscience CV 203B (Molecular Devices)

Micromanipulator: Patchstar, Scientifica

Command electrode

- This is Ag wire that has been chlorinated by immersion in 6% bleach for 15-25 min

Ground electrode: Ag/AgCl pellet either directly placed in the bath buffer or connected to the bath buffer by an agar bridge

Bunsen burner and striker or other flame source

Desktop computer with Clampex 10.6 and Clampfit 10.6 (or newer) software installed

Pipette puller: Sutter Instruments Flaming/Brown Micropipette Puller, Model P-97

Materials

Pipette buffer: 200 mM KCl, 90 mM $MgCl_2$, 5 mM $CaCl_2$, 5 mM HEPES, pH 7.4 with KOH, 0.22 µm filter-sterilized

Bath buffer: Same as pipette buffer with an additional 400 mM sucrose, 0.22 µm filtered. Store at 4°C (*see* Note 1).

Capillary tubes for creating patch pipettes

Borosilicate glass capillaries with an outer diameter of 1.8 mm, an inner diameter of 1.5 mm, and a length of 100 mm

5 mL disposable syringes

For backfilling pipettes: MicroFil 26 gauge, 96 mm long, #MF28G-5, World Precision Instruments

Glass bottom dishes: Fluorodish, FD35-100

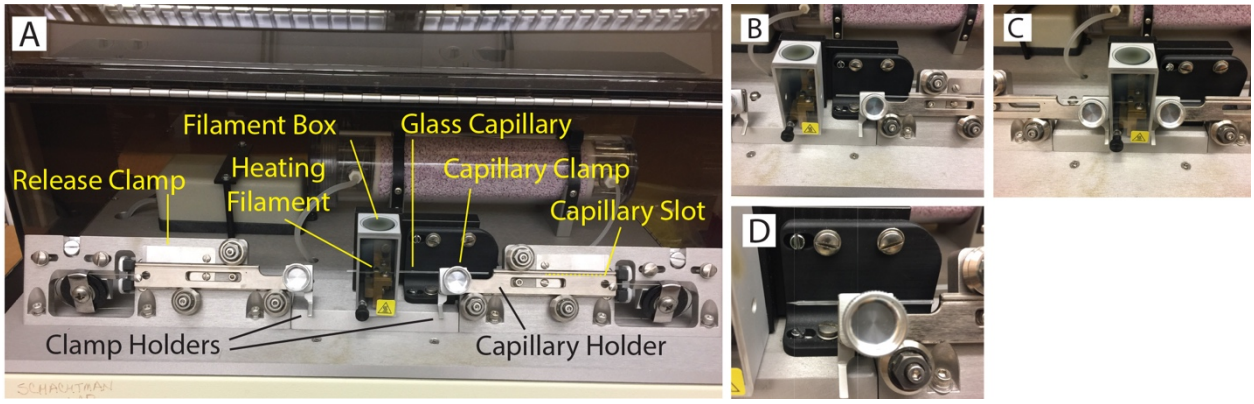

Figure 4.2. Overview of pipette pulling procedure and equipment. (A) Image of a Sutter Instruments P-97 pipette puller. (B) Image of intact, fire-polished glass capillary in capillary slot prior to centering. (C) Intact fire-polished glass capillary clamped and centered in capillary slot relative to heating filament. (D) Freshly pulled pipette still held in capillary slot by capillary clamp. In (B)-(D), both ends of the capillary are indicated with yellow arrowheads.

Procedures

Preparing patch-clamp pipettes

1. Fire-polish the ends of a borosilicate glass capillary tube by rotating them in the flame of a Bunsen burner until they are slightly rounded. This will prevent internal scratching of the headstage (*see* Note 2).
2. Pull patch pipettes from the fire-polished capillary using the micropipette puller (Figure 2). For a Sutter P-97 (Figure 2A), use the following program (*see* Note 3):
    1. Heat = 545, Velocity = 40, Time = 200
    2. Heat = 545, Velocity = 40, Time = 200

3. Heat = 560, Pull = 100, Velocity = 90, Time = 200

3. Loosen the capillary clamp and place the pipette in the capillary slot, then tighten the capillary clamp so that the pipette is held in place but can be moved horizontally (Figure 2B). Slide the capillary through the chamber containing the heating filament until it emerges on the other side. Be careful to not bump or move the delicate heating filament, as an off-center heating filament will create uneven pipettes that cannot be used.
4. Press each release clamp to free both capillary holders and push and hold the clamp holders against the filament box. Move the capillary along the horizontal metal slot so that it is centered relative to the heating filament, then tighten both clamps so the capillary is firmly held in place (Figure 2C). Do not overtighten the clamps, as this can break the capillary.
5. With the pipette pulling program loaded and displayed, shut the top cover of the P-97 and press the green “PULL” button.
6. Once the program has finished running and pipettes are ready (Figure 2D), remove pipettes by unscrewing the clamps while holding onto the polished end of each pipette.

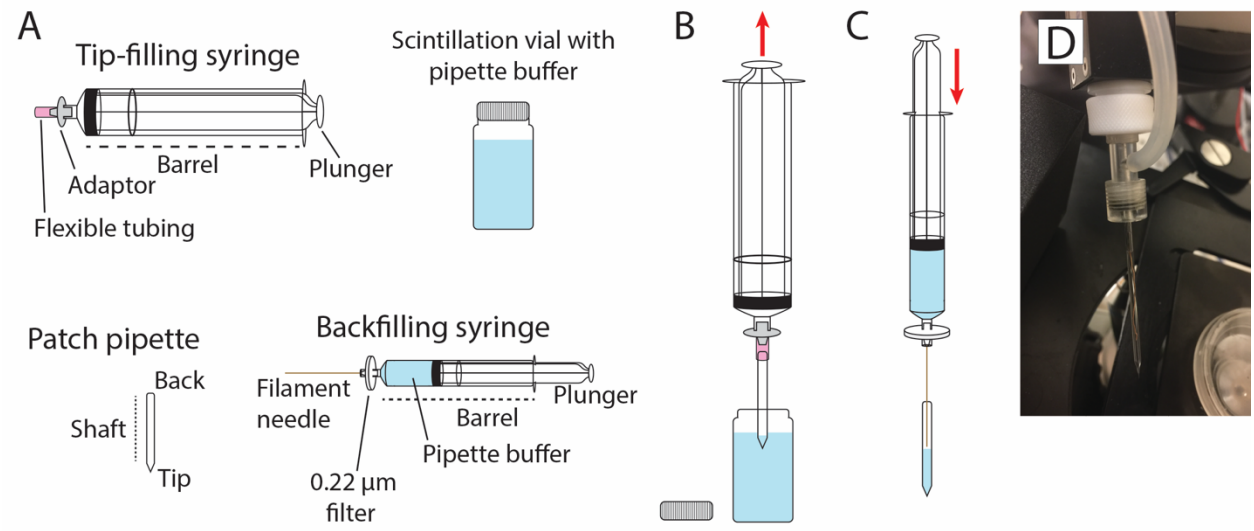

Figure 4.3. Filling a patch pipette with pipette buffer. (A) The two adapted syringes needed to fill the tip (top image) and shaft (bottom image) of a patch pipette. (B) Procedure for filling the patch pipette tip with pipette buffer using the tip-filling syringe. (C) Procedure for filling the patch pipette shaft with pipette buffer using the backfilling syringe. (D) A filled patch pipette inside the headstage chamber.

7. To fill the tips of pulled patch pipettes, prepare a tip-filling syringe (Figure 3A, top left) and prepare a clean scintillation vial. Being careful not to touch the pipette tip, insert the back of the pipette into the flexible tubing of the tip-filling syringe. Place the tip of the patch pipette in the pipette buffer of the scintillation vial and pull up on the tip-filling syringe plunger as far as resistance will allow (Figure 3B). Release the plunger and remove the patch pipette tip from the buffer. You should see a small amount of buffer in the patch pipette tip.
8. To backfill patch pipettes, prepare a back-filling syringe (Figure 3A, bottom right). Insert the filament needle into the patch pipette through the back of the patch pipette. Place the filament needle just above the pipette tip and

press down on the backfill syringe plunger until pipette buffer reaches halfway up the patch pipette (Figure 3C). Pull up slightly on the backfill syringe plunger to stop the flow of pipette buffer and remove the filament needle from the patch pipette.

9. Partially unscrew the plastic washer at the tip of the headstage, thread the patch pipette onto the command electrode filament, and *gently* push it to the back of the pipette chamber in the headstage, stopping before the pipette encounters the tube leading to the pressure clamp (Figure 3D). Tighten the plastic washer so that the patch pipette is snugly held, but do not overtighten.

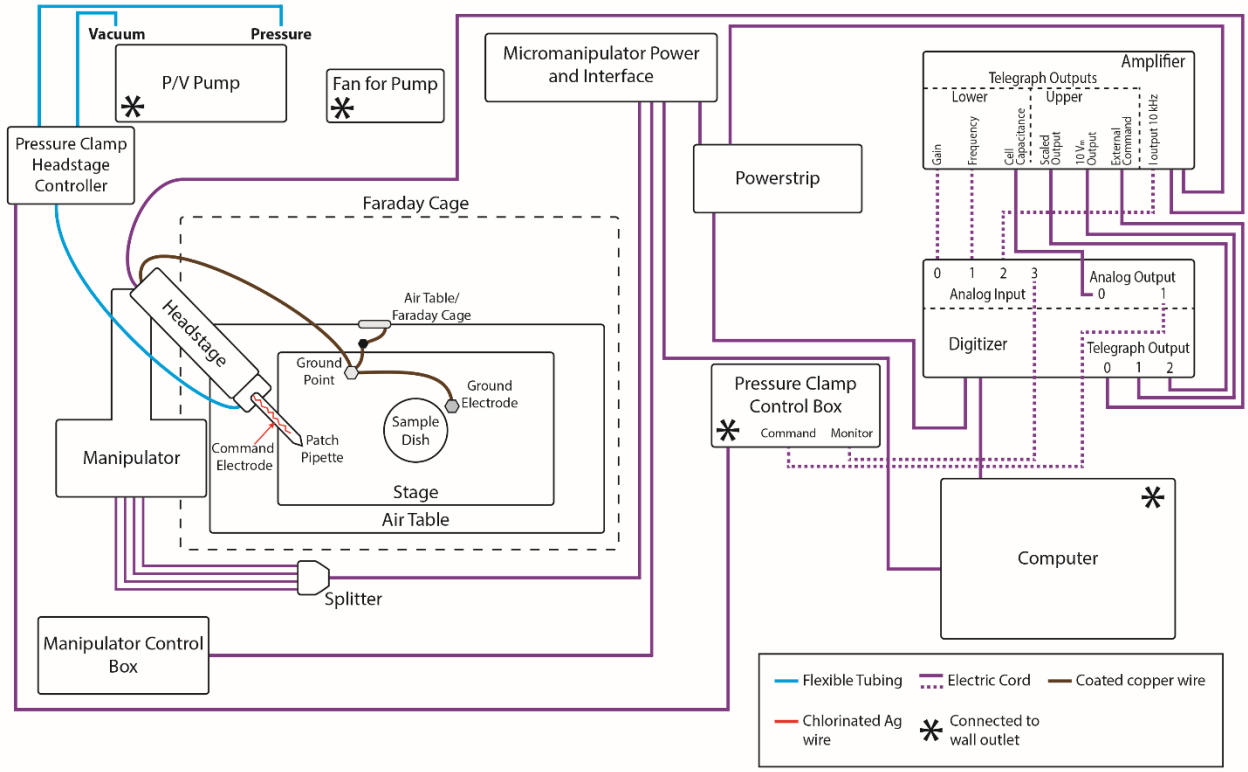

Figure 4.4. Diagram of all equipment and connections in a patch-clamp electrophysiology rig. Connections between equipment made of electric cords are shown in either pink or dashed pink lines, connections made using plastic-coated copper wire shown in brown, and connections made using flexible, hollow tubing shown in blue. Equipment powered by wall outlets are indicated by asterisks.

Obtaining an inside-out configuration patch

1. Ensure that all electrophysiology equipment is set up and the necessary connections are in place (Figures 4 and 5).
2. Bring buffers to room temperature before use to prevent condensation once buffer is added to a glass-bottom dish. Remove an aliquot of spheroplasts from the freezer and allow to thaw, then store on ice.

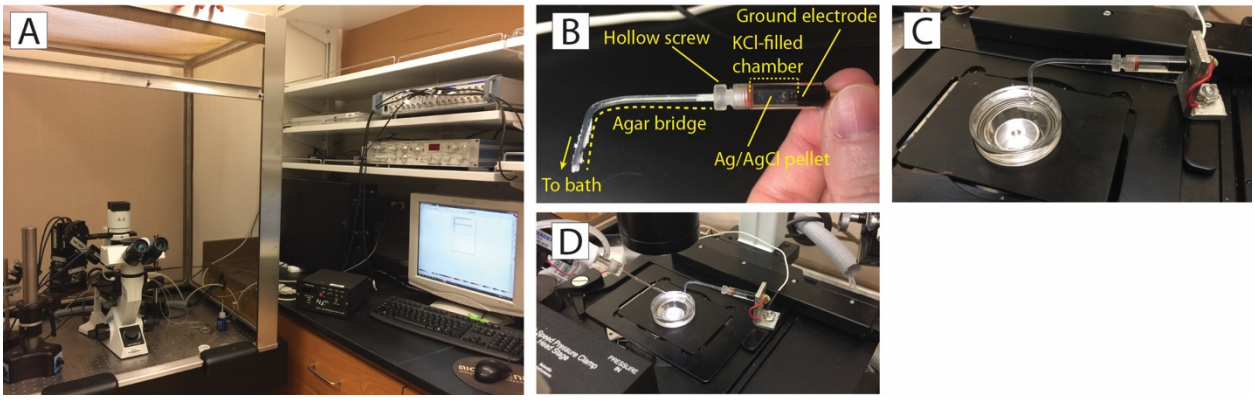

Figure 4.5. Key components of a patch-clamp electrophysiology rig. (A) View of rig with microscope on air table covered by Faraday cage, desktop computer, pressure clamp, and shelf containing micromanipulator power box, power strip, amplifier, and digitizer. The P/V pump is to the left of the Faraday cage and out of view. (B) Ground electrode with agar bridge connection showing position of electrode, KCl-filled chamber, hollow screw, and agar bridge with exposed end. (C) Close-up of sample dish connected to ground electrode via agar bridge. (D) Close-up of the microscope stage in patch-clamp set-up with pressure clamp/headstage interface, headstage holding the command electrode covered by the patch pipette, sample dish, and agar bridge connected to ground electrode.

3. Turn all equipment: PV pump, fan, pressure clamp, microscope, digitizer, amplifier, micromanipulator, and computer (Figure 5A). Ensure that all equipment is on and connected to the computer prior, then start the patching program Clampex 10.6.
4. Set up the ground electrode and/or agar bridge (*see* Note 4). In an agar bridge, the Ag/AgCl pellet is contained in a plastic chamber filled with 1 M KCl and connected to an agar bridge with a screw (Figure 5B).
5. Add ~3 mL of bath buffer to a clean glass-bottom dish. Place the dish on the microscope stage, and the ground electrode in the bath buffer. The ground electrode or agar bridge (*see* Note 5) should be submerged in the buffer (Figure 5C).

6. Add 10-40 µL spheroplasts to the dish right before analysis (most spheroplasts will lyse within ~30 min). Wait approximately 5 min for spheroplasts to settle to the bottom of the dish.
7. Meanwhile, fill a pulled patch pipette with buffer (see section *Preparing patch-clamp pipettes* above). Insert it into the headstage and position the headstage to hold the pipette tip above the sample dish (Figure 5D). While not in use, the pressure clamp should be set to maintain positive pressure in order to prevent debris from entering the headstage and patch pipette.

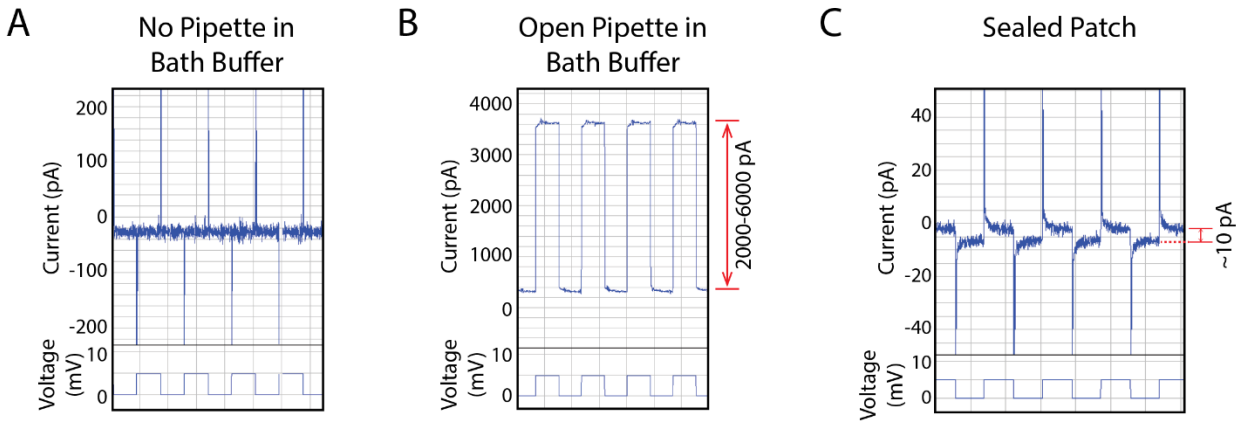

Figure 4.6. Current measurements during formation of an inside-out excised patch. (A) Current and pipette potential readings during the test pulse protocol before insertion of patch pipette into bath buffer. Application of 5 mV by the command electrode does not change current detected. (B) Current and pipette potential readings during the test pulse protocol from a patch pipette placed into bath buffer. Depending on the size of the tip opening, open currents of 2000-6000 pA at 5 mV are typical when using the buffers listed here. The current at 0 mV may deviate from 0 pA and can be adjusted using the "pipette offset" control on an Axopatch amplifier. (C) Current and pipette potential readings for a fully sealed patch during the test pulse protocol. A good seal results in the reduction of current from 2000-6000 pA to 10 pA in response to a 5 mV test pulse.

8. In Clampex, run a Gap-free program while the amplifier is set to "seal test" mode. This involves the continuous application of a two-part cycle

consisting of a 10 ms, 5 mV test pulse followed by 10 ms of no potential applied via the command electrode. This seal test mode is maintained until the inside-out patch configuration is obtained. Prior to insertion of the patch pipette into the buffer, application of the 5 mV test pulse should produce no changes in current (Figure 6A)

9. Looking through the microscope, locate an intact spheroplast of medium size that has settled at the bottom of the dish and place it in the center of the field of view. Set the pressure clamp to +25 mmHg and lower the pipette into the buffer.
10. Note the current increase through the open pipette in response to the 5 mV test pulse (Figure 6B). This current will be used to monitor and evaluate patch sealing (*see* Note 6).
11. Reduce the pressure to +10 mmHg to prevent debris from entering the patch pipette, then bring the pipette into focus. Reduce pressure to +2 mmHg to prevent rupture of target spheroplast.
12. Move the pipette tip towards the spheroplast. Just before it reaches the spheroplast, quickly reduce the pressure -40 mmHg to attach the spheroplast to the patch pipette tip. Immediately pull the pipette up from the bottom of the dish to unstick the spheroplast from the glass and allow the membrane to start sealing.
13. Spheroplast attachment and membrane sealing are indicated by a sudden decline in current during the seal test. Sealing produces a continual

decline in test pulse response current, and a complete seal is indicated by a current of 10 pA at 5 mV (Figure 6C). It can take 30 s to 5 min for a seal to form, but complete sealing becomes unlikely beyond this timeframe. Maintain pressure at -20 mmHg with brief increases to -40 mmHg as needed to ensure sealing progression (*see* Note 7).

14. At this point, the cell-attached patch configuration is achieved. To obtain an inside-out excised patch, ensure that the pipette is well above the bottom of the dish, focus on the pipette tip and the attached spheroplast, and gently tap the top of the micromanipulator with a knuckle (DO NOT flick the headstage itself) until the spheroplast dislodges from the pipette. Check that the current at 5 mV during the seal test has not changed. If the current at 5 mV increases dramatically, the seal has been lost and the procedure must be restarted from step 4 and a new pipette prepared.

Measuring MS channel activity in inside-out patches

1. Once an inside-out excised patch has been created, switch the Axopatch to external control. Change from Gap-free mode to a pressure ramp program. Check the baseline current by applying a pipette potential of +40 mV for 5 s without applied pressure, which should produce current of less than 100 pA (*see* Notes 8-9).
2. Next, begin attempting to elicit mechanosensitive currents. At a pipette potential of +40 mV, use the pressure ramp program to apply 5 s symmetric pressure ramp consisting of a 2.5 s increase to a maximum

suction of -20 mmHg, followed by 2.5 s release of suction (*see* Note 10). Increase the amount of suction applied ramp by -20 mmHg until you observe channel activity, indicated by stepwise increases in current upon increases in applied suction. Flickery increases in current may indicate that the applied pressure is approaching the activation pressure for an MS channel; in this case use smaller steps of -10 mmHg between ramps.

3. If activity is brief, increasing the maximum suction by -10 mmHg or increase the pipette potential by +20 mV to try and produce longer lived channel activity. If current increases too quickly to allow for accurate measurements of individual channel activities, reduce the suction by at least +10 mmHg or double the total ramp length.
4. Patch rupture is indicated by a sudden spike in current to levels beyond the detection limit of the amplifier. When this occurs, increase the pressure to +25 mmHg to prevent entry of debris to the headstage once the patch pipette is removed and bring the pipette to its highest position outside of the dish. Remove the pipette from the headstage and either clean the command electrode with distilled water (if not using immediately) or replace dish contents with fresh buffer and spheroplasts, prepare a new patch pipette, and begin at step 4 of the “Obtaining an inside-out configuration patch” protocol above.

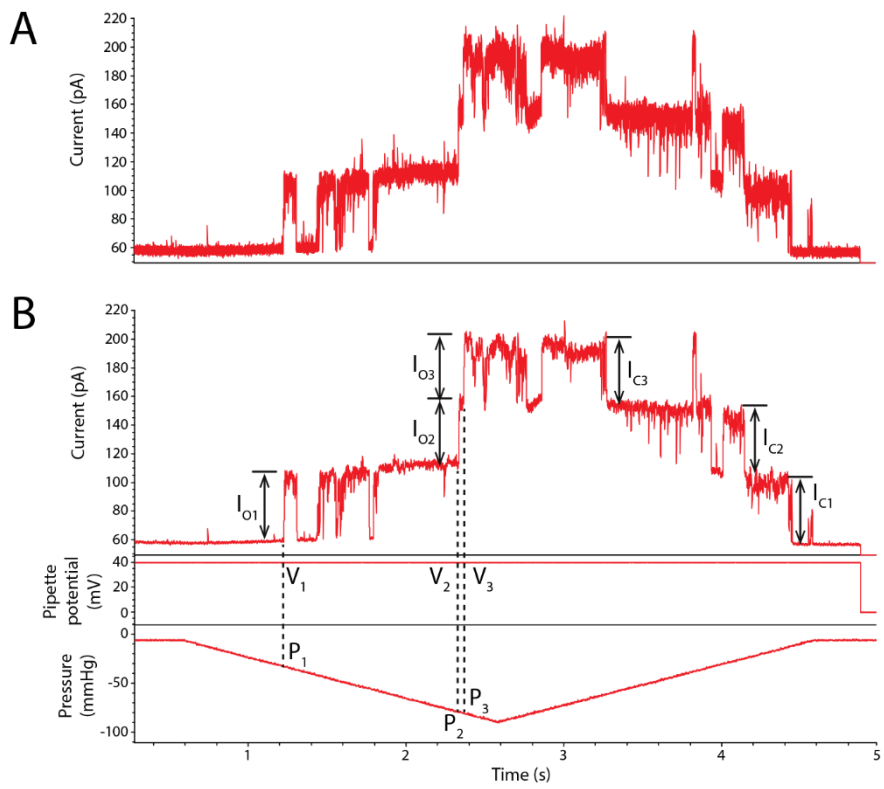

Figure 4.7 Analyzing patch-clamp electrophysiology of an MS ion channel. Current trace from an inside-out excised patch from a giant spheroplast from E. coli strain MJF641 expressing MSL1-GFP from the pET300 vector. The MSL1 sequence lacks the predicted mitochondrial targeting sequence *(C. P. Lee et al., 2016)* and has been codon-optimized for translation in E. coli. The pipette buffer contains 200 mM KCl, 90 mM $MgCl_2$, 5 mM $CaCl_2$, 5 mM HEPES, pH 7.4 and the bath buffer is identical to the pipette buffer with an additional 400 mM sucrose. Current traces before (A) and after (B) low-pass filtration at 300 Hz are shown. Corresponding voltage and pressure traces are presented below the current trace in (B). Three MS ion channel activities can be observed for which opening current change (I_O), closing current change (I_C), pipette potential (V), and applied pressure (P) are indicated.

Analyzing patch-clamp electrophysiology data for MS channels

1. Open a file to be analyzed in ClampFit 10.6. Three panels containing data for current, potential, and pressure detected by the headstage and

pressure clamp will appear. Zoom in on each trace by highlighting relevant portions of the y-axes of each panel.

2. Determine if a low-pass filter should be applied by examining the amount of high frequency noise present in the current trace. High frequency noise can obscure current levels and make exact measurements of channel activity difficult. To enable accurate measurement of single channel currents, a low pass Bessel filter can be applied to the data. The same trace before and after application of a 300 Hz low pass Bessel filter is shown in Figures 7A and B, respectively.
3. Keep a record (for example, in an electronic spreadsheet) of basic information about the trace, such as date, strain, construct, pipette potential (V_1-V_3 in Figure 7B), and ramp length.
4. To calculate conductance, measure the amount of current increase created by the first few channel openings and closing using the ClampFit software cursors, as indicated by stepwise increases (I_{O1}-I_{O3} in Figure 7B) and decreases ($I_{C1\text{-}C3}$ in Figure 7B) in current, respectively. Record in a spreadsheet the suction at which these openings occur (P_1-P_3 in Figure 7B). If tension sensitivity measurements are being made, record the current and suction for the first and second gating event observed for the experimental channel and for MscL.

Notes

1. Patching solutions are stored at 4°C in order to minimize contamination. Only completely clear solutions should be used for patching.
2. Fire-polished capillaries can be produced days, weeks, or even months in advance and stored at room temperature in a closed container free from dust. However, once a patch pipette has been pulled, it should be used the same day or discarded. Pulled pipettes can be stored in a covered, dust-free container by placing multiple narrow, thick strips of parafilm on the bottom of a large petri plate. Lay the pipettes in parallel across these parafilm strips such that they are suspended in air and separated from each other.
3. Sutter Instrument Company produces “pipette cookbooks” with recommended protocols and modifications for different types of glass and applications (Oesterle, 2018).
4. An agar bridge is an L-shaped capillary made from the same capillaries pulled to produce patch pipettes. This capillary is filled with a hot solution of 2-3% agar in 1 M KCl and allowed to cool. The opening of the longer end is connected to an Ag/AgCl pellet by a 1 M KCl solution and the opening of the shorter end placed in the bath solution. Both ends of the agar bridge should always be kept moist and, when not in use, the agar bridge should be stored in a container of 1 M KCl at 4°C to prevent dehydration and contamination.
5. After use, the ground electrode should be thoroughly rinsed with distilled water and allowed to air-dry to prevent the formation of crystals on the Ag/Cl pellet.

6. The test pulse records the current passing through the command electrode (and therefore the patch pipette in the headstage), and the magnitude of this current is determined by the size of the pipette tip opening. The “open conductance” of a buffer-filled pipette can thus be used to estimate the relative size of its tip opening to provide information on pipette geometry.
7. If after 5-10 minutes there is no further decrease in pipette current during test pulses, try either briefly applying very high (-70 to -100 mmHg) suction or strongly negative membrane potential (using a switch on the front of the Axopatch) to the patch. If successful, this will trigger continued patch sealing and decreases in current. If the pipette current is not altered, a seal is unlikely to form and a new sample aliquot and pipette must be prepared.
8. For an inside-out excised patch, the baseline current for a given membrane potential will not be zero due to imperfections in patch sealing. This baseline current should increase with higher membrane potential. If it does not, it is likely that two patches of membrane have formed a bubble at the tip, making detection of any MS channel activities unlikely. Change from the pressure ramp program to the Gap-free program and from external control to seal test mode. Briefly raise the pipette tip out of the bath buffer then submerge it and use the seal test to determine if the patch remains sealed. If the seal is still present, continue data collection at step 1 of the *Measuring MS channel activity in inside-out patches* protocol. If the seal ruptures, the patch pipette should be removed, a new patch

pipette prepared, and the *Obtaining an inside-out configuration patch* protocol begun from step 4.

9. Depending on the exact membrane potential used, baseline current may range from 10-200 pA (positive or negative). Baseline currents higher than this will likely render the signal-to-noise ratio too small to detect MS channel activity. In this case, the patch pipette should be discarded, a new patch pipette prepared, and the *Obtaining an inside-out configuration patch* protocol begun from step 4.
10. In cases in which multiple channel activities become difficult to separate, the ramp length should be increased in order to reduce the rate of suction application and changes in channel open probabilities. This is done by modifying both the total length of your patch program within the Clampex software.

Chapter 5: Conclusions and Future Directions

5.1. Summary

My thesis work progresses the study of plant mechanobiology and mechanosensitive (MS) ion channels in three main ways. First, my work with the mitochondrial MS ion channel MSL1 from *Arabidopsis thaliana* helps provide insight into the structural basis for controlling gating kinetics, insights which may be applicable to the broader MscS family. Second, though not successful in itself, my attempt to build a genetically-encoded fluorescence-based membrane tension sensor provides a cautionary tale describing a potential approach for tension sensor design and important controls to ensure utility and specificity. Finally, my protocol for studying plant MS channels using patch-clamp electrophysiology in giant *E. coli* spheroplasts provides a valuable resource for the field and highlights a need for similar detailed protocols to enable efficient analysis of MS channel behavior in less common systems.

5.2. Exploring the Mechanism, Regulation, and Physiological Relevance of MSL1 Activity

In Chapter 2 of my thesis, I show that two charged residues in the pore-lining helix of the MS channel MSL1 control gating kinetics by regulating transitions between the closed and open state and open state stability. These results were used to propose

the “sweet spot” model, which states that interactions between the opposing charges of R326 and D327 govern the relative stability of closed and open states. However, a limited number of MSL1 variants were used in this study with only one mutation made to R326. In addition, the sweet spot model proposed does not easily describe certain results observed, including the increased gating tension of MSL1$^{R326Q\ D327G}$-GFP, MSL1^{D327N}-GFP, and MSL1$^{R326Q\ D327N}$-GFP and the counterintuitive combination of flickery gating and extended channel activity duration of MSL1^{D327G}-GFP and MSL1$^{R326Q\ D327G}$-GFP. The inclusion of additional MSL1 variants, such as those in which the R326 and D327 residues are swapped or those involving mutations of surrounding residues, along with molecular dynamics simulations of interactions present during MSL1 gating transitions would be an immediate next step to improving and expanding my model of MSL1 gating.

Given its location in the inner mitochondrial membrane and role during redox stress (C. P. Lee et al., 2016), it is not an unreasonable prediction that MSL1 is redox regulated. MSL1 possesses three cysteine residues, one of which, C303, is located in the intermembrane space and two, C440 and C456, that sit in the matrix. Preliminary experiments by Dr. Grigory Maksaev indicate that application of the reducing agent ß-ME to the matrix side of MSL1 increases gating pressure variability while addition of the oxidizing agent $KMnO_4$ to the matrix side non-reversibly eliminates MSL1 activity. In addition, preliminary hypoosmotic shock plating assays with MSL1 variants containing single, double, and triple cysteine-to-serine mutations of the residues above indicated that none of these MSL1 variants show normal MSL1 function in *E. coli*, suggesting a

loss of channel function. Under normal conditions, the intermembrane space of mitochondria is an oxidizing environment while the matrix space is a reducing environment (Depuydt et al., 2011). To what degree these redox states could change during stresses that trigger MSL1 responses, especially in regions surrounding MSL1, and possible significance of this is uncertain. Additional insight into distances between cysteine residues in the closed and open states of MSL1 from recent structures will also provide valuable information regarding this possibility (Deng et al., 2020; Y. Li et al., 2020).

A broader question emerging from my work with MSL1 is whether the MS channel activity of MSL1 is physiologically relevant. As noted above, MSL1 is mechanically activated and appears to create membrane dimples to enhance this sensitivity (Deng et al., 2020; Y. Li et al., 2020; C. P. Lee et al., 2016), thus one would expect either local swelling or straightening of the inner mitochondrial membrane to activate MSL1. MSL1 also seems required for normal responses to mitochondrial stress in *Arabidopsis* (C. P. Lee et al., 2016), including cadmium, excess heat, and the oxidative phosphorylation inhibitors oligomycin A and antimycin A. Mitochondrial swelling occurs in response to many different types of stress in animals and plants, including heavy metals, excess Ca^{2+}, anoxia, and oxidation (Anastacio et al., 2013; Halestrap, 2006; Virolainen et al., 2002; Zancani et al., 2015). Thus in the event of extreme stress, matrix swelling could create the tension necessary for MSL1 activation. To test this, mitochondria with and without MSL1 could be stained with TMRM while expressing mitochondria-localized GFP or while expressing roGFP and imaged before

and after introduction of stressors associated with MSL1 function. This would enable simultaneous quantification of mitochondria size, redox state, and potential to see if mitochondria swelling during stress is a likely trigger of MSL1 activity. Additionally, performing the above assays with *msl1-1* plants complemented with either my MSL1 variants or WT MSL1 would test the role of channel kinetics in MSL1 function.

More dramatic phenotypes than those of *msl1-1* emerge in the *msl1-1 msl2-3 msl3-1* mutant. Major phenotypes of the *msl2-3 msl3-1* mutant include rumpled and variegated leaves, partially exacerbated by addition of the *msl1-1* lesion, as well as reduced primary root length, a lower density of lateral roots, and ROS accumulation and callus production at the shoot apical meristem (SAM), all of which are partially or fully suppressed in *msl1-1 msl2-3 msl3-1* plants (J. Lee et al., 2018). These more dramatic phenotypes may provide a better environment for evaluating the subtle phenotypes of my MSL1 variants, as well as others created in the future.

5.3. Tension Sensor Results Suggest Systematic Testing Approach for Future Sensor Development.

One valuable piece of information in solving the mystery of the physiological function of MSL1 would be the levels of membrane tension present during stress responses involving MSL1. For these and other potential applications, I attempted to create a genetically-encoded fluorescence-based membrane tension sensor. I ultimately showed that mcpGFP signal changes in my tension sensor candidates arise

independently of protein to which mcpGFP is inserted (Figure 3.11), indicating that mcpGFP is likely sensitive to cellular conditions besides membrane tension. What these conditions are is currently unknown, however, many possibilities can be identified based on known sensitivities of GFP-derived proteins and changes that occur in *E. coli* during osmotic shock. Hypoosmotic shock in *E. coli* triggers transient changes in cytoplasmic levels of Ca^{2+} (C. D. Cox et al., 2013), K^{+} (Levina, 1999), and cytoplasmic crowding (based on changes in cellular optical density) (Boer et al., 2011b), with additional changes in cellular contents possible depending on the ionic composition of the bacterial environment. GFP and GFP derivatives are often pH sensitive, with many GFP derivatives exhibiting multiple excitation peaks depending on pH (Tsien, 1998). It is therefore possible that mcpGFP or related fluorescent reporters are sensitive to cellular conditions beyond tension that may change in a given assay and it is important that future tension sensor development focuses on eliminating potential nonspecific responses. At minimum, depending on the desired application, careful characterization of any nonspecific responses is required.

I also showed that normal MscS function does not tolerate mcpGFP insertion within the MscS cytoplasmic domain (Figure 3.3). In contrast, MscS containing mcpGFP in either the cytoplasmic loop connecting TM1 and TM2 shows altered channel activity and MscS C-terminally tagged with mcpGFP behaves normally (Figures 3.3-3.4). Since monomeric expression levels of these nonfunctional candidates are comparable to that of C-terminally tagged $MscS^{A286}$-mcpGFP, it is unclear if these nonfunctional candidates form normal heptamers or otherwise. In light of this, alternative tension-sensing

scaffolds, especially with extensive soluble domains or regions otherwise amenable to insertion, should be tested. To this end, our group and Wolf Frommer's group have worked briefly on tension sensors involving MSL10, however, no work has yielded a functional sensor to this point.

5.4. Patch-Clamp Electrophysiology With Multiple Expression Systems Provides a Platform for the Identification of Plant MS Channels

In addition to attempting to create novel tools for studying mechanobiology, I also created a detailed protocol for single channel analysis of plant MS channel behavior using patch-clamp electrophysiology in giant *E. coli* spheroplasts, building on previous protocols for electrophysiological analysis of MS channels in *E. coli* spheroplasts (Grigory Maksaev & Haswell, 2015; Martinac et al., 2013) and *Xenopus* oocytes. Patch-clamp electrophysiology is useful for studying plant MS ion channels because it allows for control of environment surrounding the membrane, precise application of mechanical stimulation, and unambiguous quantification of channel properties. In addition, the multiple systems available for expression of these channels, ranging from (in some cases) native membranes to heterologous systems, provides many options that range in technical difficulty and advantages, depending on the native environment of a channel of study, to allow for successful patching. *E. coli* in particular offer fast growth and expression and the ability to tightly control expression levels, representing a useful

system for initial evaluation of novel channels (including those listed in (Eric S. Hamilton et al., 2015)) prior to evaluation of channel activity.

In closing, my dissertation progresses the field of mechanobiology through expanding our knowledge of MS ion channels function, how they might be applied as tools to fuel future research, and how researcher might go about studying single MS channel properties. The steps I have proposed extending forward will provide details underlying mechanobiological phenomena that allow for mechanistic descriptions of phenomena that otherwise may remain otherwise qualitative or predicted rather than certain.

Appendix: MSL1^{A320V} has enhanced open state stability compared to MSL1

Adapted from work published as:

Z. Deng, G. Maksaev*, A.M. Schlegel*, J. Zhang, M. Rau, J. A. J. Fitzpatrick, E. S. Haswell, P. Yuan. (2020). Structural mechanism for gating of a eukaryotic mechanosensitive channel of small conductance. *Nature Communications* (11). https://doi.org/10.1038/s41467-020-17538-1

6.1. Background and Motivation

Mechanosensitive (MS) ion channels are mechanotransductory systems present throughout all domains of life (Eric S. Hamilton et al., 2015; Anna Kloda & Martinac, 2001; Kung et al., 2010; Ranade et al., 2015) and include channels gated directly and indirectly by force transmitted through the membrane (Charles D. Cox et al., 2019). Determining the structures of these MS ion channels is critical for understanding the exact mechanisms by which this gating occurs, including the specific role(s) played by the membrane in which the channel is embedded.

Cryogenic electron microscopy (cryoEM) has been used to generate structures of multiple MS ion channels in the past decade, including *E. coli* YnaI (Böttcher et al., 2015; Yu et al., 2018), *Drosophila* NOMPC (Jin et al., 2017), mPiezo1 (Guo & MacKinnon, 2017; Saotome et al., 2018), *E. coli* MscS (T. Rasmussen et al., 2019; Reddy et al., 2019), and *A. thaliana* MSL1 (Y. Li et al., 2020). X-ray crystallography has also been used to generate structures of multiple MS channels, including MscS (Bass et

al., 2002; Lai et al., 2013; Pliotas et al., 2015; Steinbacher et al., 2007; Wang et al., 2008; X. Zhang et al., 2012) and MscL (Chang et al., 1998; Herrera et al., 2018; Liu et al., 2009; Walton & Rees, 2013) homologs from multiple species and TRAAK (Brohawn et al., 2012, 2014; Lolicato et al., 2014). However, different factors present during sample preparation, such as detergent choice and temperature, can dramatically alter structures generated by x-ray crystallography (Reading et al., 2015). In addition, the ability to generate structures of proteins in membranes of varying composition using cryoEM can provide useful insights into MS channel interactions with both individual lipids and the bilayer at large (Haselwandter & MacKinnon, 2018; Tim Rasmussen et al., 2019). With greatly improved resolution in recent years (Lau et al., 2018), cryoEM has thus become a viable technique for generating MS channel structures.

The first published MscS crystal structure (Bass et al., 2002) represents a nonconducting state based on experimental studies of residue accessibility and models of likely conformational changes during gating (Andriy Anishkin & Sukharev, 2004; Vásquez et al., 2008). Later generation of the MscS^{A106V} crystal structure revealed a likely open state MscS structure based on factors including increased pore size and rotated pore-lining helices (Wang et al., 2008). Inspired by these contrasting results, (Deng et al., 2020) produced cryoEM structures of *A. thaliana* MSL1 and the MSL1^{A320V} variant, corresponding to MscS^{A106V}. Initial examination of both structures suggested that, like the initial structures of MscS, the MSL1 cryoEM structure represents a nonconducting state while the MSL1^{A320V} structure represents a conducting state due to

its increased pore size and in-plane membrane area generated through dramatic flattening of the TM domain.

6.2. Results and Discussion

To test whether or not MSL1^{A320V} likely represents a conducting state, single-channel patch-clamp electrophysiology in giant *E. coli* spheroplasts was performed with GFP-tagged versions of MSL1, MSL1^{A320V}, and *E. coli* MscS (Table 1). This was both to compare MSL1 and MSL1^{A320V} behavior. First, conductance and gating pressure relative to endogenously expressed MscL were determined for MSL1-GFP, MSL1^{A320V}-GFP, and MscS-GFP. Conductance for MSL1-GFP and MscS-GFP were 1.02 ± 0.17 nS and 0.98 ± 0.12 nS, similar to previously reported values (S. Sukharev, 2002; C. P. Lee et al., 2016) and indistinguishable from the 1.12 ± 0.16 nS conductance of MSL1^{A320V}-GFP. In addition, relative gating pressures of all three channels were also statistically identical, thus neither supporting nor refuting the assertion that MSL1^{A320V}-GFP likely represents an open state conformation.

	MSL1-GFP	**MSL1^{A320V}-GFP**	**MscS-GFP**
Conductance (nS)	1.02 ± 0.17	1.12 ± 0.16	0.98 ± 0.12
Relative gating pressure (P_x/P_{MscL})	0.49 ± 0.16	0.63 ± 0.14	0.55 ± 0.15

Table A1. MSL1-GFP, MSL1^{A320V}-GFP, and MscS-GFP have similar conductances and relative gating pressures. Channel activities were triggered by application of 2.5 s symmetric pressure ramps at membrane potentials of -70 mV. Values are averages ± standard deviation. No difference in conductance or gating pressure relative to endogenous MscL was observed between MSL-GFP and MSL1^{A320V}-GFP using one-way ANOVA followed by post-hoc Tukey's test, $p < 0.05$. N = 10 patches per variant.

We also looked at the gating kinetics of MSL1-GFP and MSL1^{A320V}-GFP by quantifying channel activity duration, subconducting state prevalence (Figure A1, Table A2) and proportion of channel opening observed prior to pressure application (Table A2). Channel activity was stimulated using a symmetric 1-2 s pressure ramp at a membrane potential of -70 mV, after which membrane potential was maintained at -70 mV for 100 s total and channel activity monitored. Pressure-triggered MSL1^{A320V} activity often lasted for 80 s or more (44.1%), in many cases not closing prior to the end of the trace, while most MSL1 activity lasted less than 20 s (90.3%; Figure A1). In addition, MSL1^{A320V} showed a higher prevalence of subconducting states (50% vs 29%, respectively) and channels open at prior to pressure application compared to MSL1 (57% vs 25%, respectively; Table A2). Overall, these results indicate that the MSL1^{A320V} variant likely has a stabilized open state or impeded closure, supporting the assertion that the MSL1^{A320V} cryoEM structure represents the open state of MSL1.

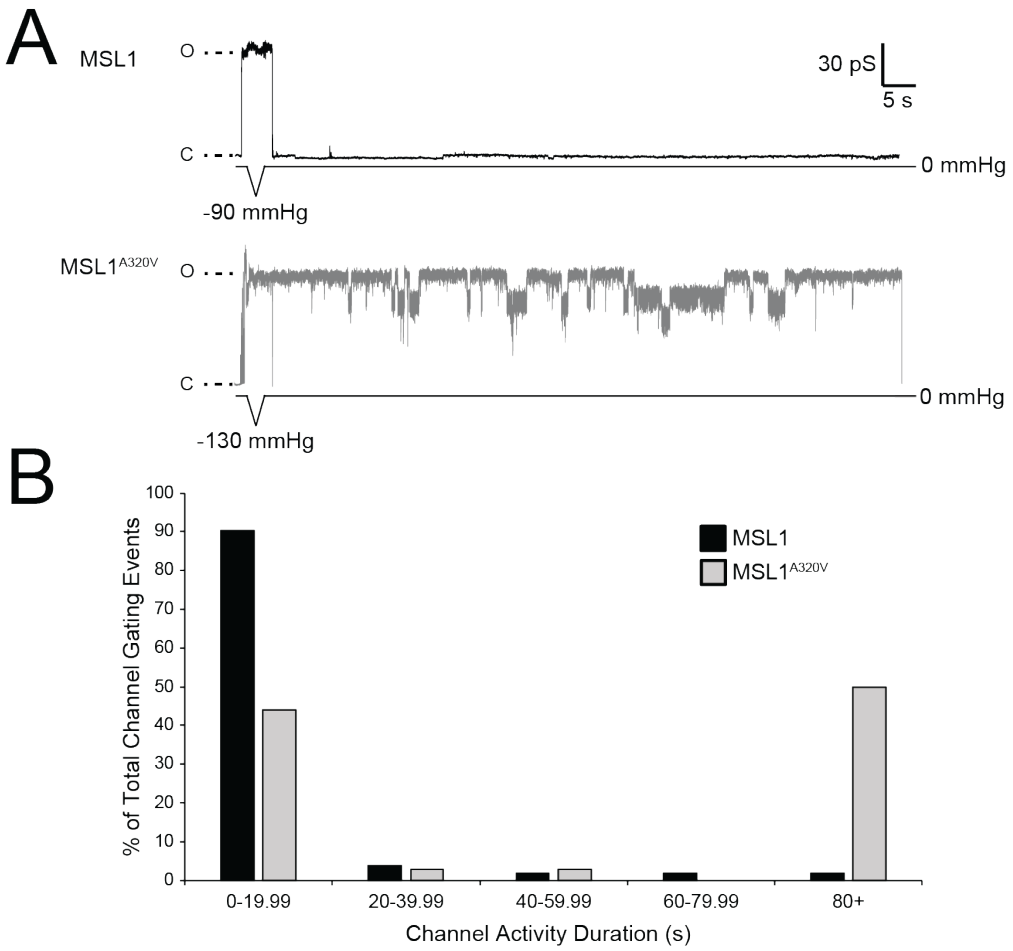

Figure A1. Representative traces for single MSL1 and MSL1^{A320V} channel activities in response to a brief 1 s pressure ramp followed by 90 s without pressure. (A) Closed state (baseline) current is indicated by "C" while open states are indicated by "O". The maximum negative pressure used is indicated. Membrane potential was clamped at -70 mV. Multiple subconducting states were observed with the MSL1^{A320V} mutant, while the peak unitary current of MSL1^{A320V} was indistinguishable from that of the wild type (Table A1). (B) Percentages of MSL1 (black) and MSL1^{A320V} (grey) gating events with open dwell times of 0-19.99 s, 20-39.99 s, 40-59.99 s, 60-79.99 s, or 80+ s. Data represents traces obtained from 10 patches per variant channel with only the first gating event analyzed per trace (103 traces for MSL1, 34 for MSL1^{A320V}).

	MSL1-GFP	**MSL1^{A320V}-GFP**
Channel(s) open before pressure ramp	25% (3/12 traces)	57% (8/14 traces)

Channel exhibits subconducting state	29% (30/102 traces)	50% (17/34 traces)
Subconducting state follows full opening	17% (5/30 traces)	82% (14/17 traces)

Table A2. Spontaneous opening and subconducting states for MSL1-GFP and MSL1^{A320V}-GFP. Channel activity prior to pressure ramp application for all patches obtained from spheroplasts expressing *At*MSL1 or *At*MSL1 A320V is shown. Channel activity was measured by measuring current while clamping membrane potential at -70 mV for 5 s without pressure application immediately after a patch was obtained; N = 12 and 14 patches for *At*MSL1 and *At*MSL1 A320V. The presence of subconducting states, and if they followed a full channel opening, in lifetime traces of pressure-gated channels only is shown; N = 10 patches for each variant.

References

Akerboom, J., Rivera, J. D. V., Guilbe, M. M. R., Malavé, E. C. A., Hernandez, H. H., Tian, L., Hires, S. A., Marvin, J. S., Looger, L. L., & Schreiter, E. R. (2009). Crystal Structures of the GCaMP Calcium Sensor Reveal the Mechanism of Fluorescence Signal Change and Aid Rational Design. *Journal of Biological Chemistry*, *284*(10), 6455–6464. https://doi.org/10.1074/jbc.M807657200

Akitake, B., Anishkin, A., Liu, N., & Sukharev, S. (2007). Straightening and sequential buckling of the pore-lining helices define the gating cycle of MscS. *Nat Struct Mol Biol*, *14*(12), 1141–1149. https://doi.org/10.1038/nsmb1341

Akitake, B., Anishkin, A., & Sukharev, S. (2005). The "Dashpot" Mechanism of Stretch-dependent Gating in MscS. *Journal of General Physiology*, *125*(2), 143–154. https://doi.org/10.1085/jgp.200409198

Aller, I., Rouhier, N., & Meyer, A. J. (2013). Development of roGFP2-derived redox probes for measurement of the glutathione redox potential in the cytosol of severely glutathione-deficient rml1 seedlings. *Frontiers in Plant Science*, *4*. https://doi.org/10.3389/fpls.2013.00506

Alsharif, G., Ahmad, S., Islam, M. S., Shah, R., Busby, S. J., & Krachler, A. M. (2015). Host attachment and fluid shear are integrated into a mechanical signal regulating virulence in Escherichia coli O157:H7. *Proceedings of the National Academy of Sciences*, *112*(17), 5503–5508. https://doi.org/10.1073/pnas.1422986112

Anastacio, M. M., Kanter Evelyn M., Makepeace Carol M., Keith Angela D., Zhang Haixia, Schuessler Richard B., Nichols Colin G., & Lawton Jennifer S. (2013). Relationship Between Mitochondrial Matrix Volume and Cellular Volume in Response to Stress and the Role of ATP-Sensitive Potassium Channel. *Circulation*, *128*(11_suppl_1), S130–S135. https://doi.org/10.1161/CIRCULATIONAHA.112.000128

Anishkin, A, Akitake, B., Kamaraju, K., Chiang, C.-S., & Sukharev, S. (2010). Hydration properties of mechanosensitive channel pores define the energetics of gating. *J Phys Condens Matter*, *22*(45), 454120. https://doi.org/10.1088/0953-8984/22/45/454120

Anishkin, Andriy, & Sukharev, S. (2004). Water Dynamics and Dewetting Transitions in the Small Mechanosensitive Channel MscS. *Biophysical Journal*, *86*(5), 2883–2895. https://doi.org/10.1016/S0006-3495(04)74340-4

Ast, C., De Michele, R., Kumke, M. U., & Frommer, W. B. (2015). Single-fluorophore membrane transport activity sensors with dual-emission read-out. *ELife*, *4*, e07113. https://doi.org/10.7554/eLife.07113

Ast, C., Foret, J., Oltrogge, L. M., De Michele, R., Kleist, T. J., Ho, C.-H., & Frommer, W. B. (2017). Ratiometric Matryoshka biosensors from a nested cassette of green- and orange-emitting fluorescent proteins. *Nature Communications*, *8*(1), 1–13. https://doi.org/10.1038/s41467-017-00400-2

Austen, K., Ringer, P., Mehlich, A., Chrostek-Grashoff, A., Kluger, C., Klingner, C., Sabass, B., Zent, R., Rief, M., & Grashoff, C. (2015). Extracellular rigidity sensing by talin isoform-specific mechanical linkages. *Nature Cell Biology*, *17*(12), 1597–1606. https://doi.org/10.1038/ncb3268

Bartlett, J. L., Levin, G., & Blount, P. (2004). An in vivo assay identifies changes in residue accessibility on mechanosensitive channel gating. *PNAS*, *101*(27), 10161–10165. https://doi.org/10.1073/pnas.0402040101

Bass, R. B., Strop, P., Barclay, M., & Rees, D. C. (2002). Crystal Structure of Escherichia coli MscS, a Voltage-Modulated and Mechanosensitive Channel. *Science*, *298*(5598), 1582–1587. https://doi.org/10.1126/science.1077945

Basu, D., & Haswell, E. S. (2017). Plant mechanosensitive ion channels: An ocean of possibilities. *Curr Opin Plant Biol*, *40*, 43–48. https://doi.org/10.1016/j.pbi.2017.07.002

Battle, A. R., Petrov, E., Pal, P., & Martinac, B. (2009). Rapid and improved reconstitution of bacterial mechanosensitive ion channel proteins MscS and MscL into liposomes using a modified sucrose method. *FEBS Letters*, *583*(2), 407–412. https://doi.org/10.1016/j.febslet.2008.12.033

Belas, R. (2014). Biofilms, flagella, and mechanosensing of surfaces by bacteria. *Trends in Microbiology*, *22*(9), 517–527. https://doi.org/10.1016/j.tim.2014.05.002

Belyy, V., Anishkin, A., Kamaraju, K., Liu, N., & Sukharev, S. (2010). The tension-transmitting “clutch” in the mechanosensitive channel MscS. *Nat Struct Mol Biol*, *17*(4), 451–458. https://doi.org/10.1038/nsmb.1775

Belyy, V., Kamaraju, K., Akitake, B., Anishkin, A., & Sukharev, S. (2010). Adaptive behavior of bacterial mechanosensitive channels is coupled to membrane mechanics. *The Journal of General Physiology*, *135*(6), 641–652. https://doi.org/10.1085/jgp.200910371

Bialecka-Fornal, M., Lee, H. J., & Phillips, R. (2015). The Rate of Osmotic Downshock Determines the Survival Probability of Bacterial Mechanosensitive Channel Mutants. *J Bacteriol*, *197*(1), 231–237. https://doi.org/10.1128/JB.02175-14

Bidhendi, A. J., Zamil, M. S., & Geitmann, A. (2020). Assembly of a simple scalable device for micromechanical testing of plant tissues. In *Methods in Cell Biology*. Academic Press. https://doi.org/10.1016/bs.mcb.2020.04.003

Birdsell, D. C., & Cota-Robles, E. H. (1967). Production and ultrastructure of lysozyme and ethylenediaminetetraacetate-lysozyme spheroplasts of Escherichia coli. *J Bacteriol*, *93*(1), 427–437.

Blount, P., Schroeder, M. J., & Kung, C. (1997). Mutations in a Bacterial Mechanosensitive Channel Change the Cellular Response to Osmotic Stress. *Journal of Biological Chemistry*, *272*(51), 32150–32157. https://doi.org/10.1074/jbc.272.51.32150

Blount, P., Sukharev, S. I., Schroeder, M. J., Nagle, S. K., & Kung, C. (1996). Single residue substitutions that change the gating properties of a mechanosensitive channel in Escherichia coli. *PNAS*, *93*(21), 11652–11657. https://doi.org/10.1073/pnas.93.21.11652

Boer, M., Anishkin, A., & Sukharev, S. (2011a). Adaptive MscS gating in the osmotic permeability response in E. coli: The question of time. *Biochemistry*, *50*(19), 4087–4096. https://doi.org/10.1021/bi1019435.Adaptive

Boer, M., Anishkin, A., & Sukharev, S. (2011b). Adaptive MscS Gating in the Osmotic Permeability Response in E. coli: The Question of Time. *Biochemistry*, *50*(19), 4087–4096. https://doi.org/10.1021/bi1019435

Booth, I. R. (2014). Bacterial mechanosensitive channels: Progress towards an understanding of their roles in cell physiology. *Current Opinion in Microbiology*, *18*, 16–22. https://doi.org/10.1016/j.mib.2014.01.005

Börngen, K., Battle, A. R., Möker, N., Morbach, S., Marin, K., Martinac, B., & Krämer, R. (2010). The properties and contribution of the Corynebacterium glutamicum MscS variant to fine-tuning of osmotic adaptation.

Biochimica et Biophysica Acta (BBA) - Biomembranes, *1798*(11), 2141–2149. https://doi.org/10.1016/j.bbamem.2010.06.022

Böttcher, B., Prazak, V., Rasmussen, A., Black, S. S., & Rasmussen, T. (2015). The Structure of YnaI Implies Structural and Mechanistic Conservation in the MscS Family of Mechanosensitive Channels. *Structure*, *23*(9), 1705–1714. https://doi.org/10.1016/j.str.2015.06.023

Braybrook, S. A. (2015). Chapter 13—Measuring the elasticity of plant cells with atomic force microscopy. In E. K. Paluch (Ed.), *Methods in Cell Biology* (Vol. 125, pp. 237–254). Academic Press. https://doi.org/10.1016/bs.mcb.2014.10.006

Bremer, E., & Krämer, R. (2019). Responses of Microorganisms to Osmotic Stress. *Annual Review of Microbiology*, *73*, 313–334. https://doi.org/10.1146/annurev-micro-020518-115504

Brenner, M. D., Zhou, R., & Ha, T. (2011). Forcing a connection: Impacts of single-molecule force spectroscopy on in vivo tension sensing. *Biopolymers*, *95*(5), 332–344. https://doi.org/10.1002/bip.21587

Brohawn, S. G., Campbell, E. B., & MacKinnon, R. (2014). Physical mechanism for gating and mechanosensitivity of the human TRAAK K + channel. *Nature*, *516*(7529), 126–130. https://doi.org/10.1038/nature14013

Brohawn, S. G., Mármol, J. del, & MacKinnon, R. (2012). Crystal Structure of the Human K2P TRAAK, a Lipid- and Mechano-Sensitive K+ Ion Channel. *Science*, *335*(6067), 436–441. https://doi.org/10.1126/science.1213808

Buda, R., Liu, Y., Yang, J., Hegde, S., Stevenson, K., Bai, F., & Pilizota, T. (2016). Dynamics of Escherichia coli's passive response to a sudden decrease in external osmolarity. *PNAS*, *113*(40), E5838–E5846. https://doi.org/10.1073/pnas.1522185113

Campàs, O., Mammoto, T., Hasso, S., Sperling, R. A., O'Connell, D., Bischof, A. G., Maas, R., Weitz, D. A., Mahadevan, L., & Ingber, D. E. (2014). Quantifying cell-generated mechanical forces within living embryonic tissues. *Nature Methods*, *11*(2), 183–189. https://doi.org/10.1038/nmeth.2761

Carraretto, L., Teardo, E., Checchetto, V., Finazzi, G., Uozumi, N., & Szabo, I. (2016). Ion channels in plant bioenergetic organelles, chloroplasts and mitochondria: From molecular identification to function. *Mol Plant*, *9*(3), 371–395. https://doi.org/10.1016/j.molp.2015.12.004

Çetiner, U., Anishkin, A., & Sukharev, S. (2018). Spatiotemporal relationships defining the adaptive gating of the bacterial mechanosensitive channel MscS. *European Biophysics Journal*, *47*(6), 663–677. https://doi.org/10.1007/s00249-018-1303-5

Chang, G., Spencer, R. H., Lee, A. T., Barclay, M. T., & Rees, D. C. (1998). Structure of the MscL Homolog from Mycobacterium tuberculosis: A Gated Mechanosensitive Ion Channel. *Science*, *282*(5397), 2220–2226. https://doi.org/10.1126/science.282.5397.2220

Chen, C., Brock, R., Luh, F., Chou, P.-J., Larrick, J. W., Huang, R.-F., & Huang, T. (1995). The solution structure of the active domain of CAP18—A lipopolysaccharide binding protein from rabbit leukocytes. *FEBS Letters*, *370*(1), 46–52. https://doi.org/10.1016/0014-5793(95)00792-8

Cheng, Y.-R., Jiang, B.-Y., & Chen, C.-C. (2018). Acid-sensing ion channels: Dual function proteins for chemo-sensing and mechano-sensing. *Journal of Biomedical Science*, *25*(1), 46. https://doi.org/10.1186/s12929-018-0448-y

Chure, G., Lee, H. J., Rasmussen, A., & Phillips, R. (2018). Connecting the Dots between Mechanosensitive Channel Abundance, Osmotic Shock, and Survival at Single-Cell Resolution. *Journal of Bacteriology*, *200*(23). https://doi.org/10.1128/JB.00460-18

Colom, A., Derivery, E., Soleimanpour, S., Tomba, C., Molin, M. D., Sakai, N., González-Gaitán, M., Matile, S., & Roux, A. (2018). A fluorescent membrane tension probe. *Nature Chemistry*, *10*(11), 1118–1125. https://doi.org/10.1038/s41557-018-0127-3

Coste, B., Mathur, J., Schmidt, M., Earley, T. J., Ranade, S., Petrus, M. J., Dubin, A. E., & Patapoutian, A. (2010). Piezo1 and Piezo2 Are Essential Components of Distinct Mechanically Activated Cation Channels. *Science*, *330*(6000), 55–60. https://doi.org/10.1126/science.1193270

Coste, Bertrand, Xiao, B., Santos, J. S., Syeda, R., Grandl, J., Spencer, K. S., Kim, S. E., Schmidt, M., Mathur, J., Dubin, A. E., Montal, M., & Patapoutian, A. (2012). Piezo proteins are pore-forming subunits of mechanically activated channels. *Nature*, *483*(7388), 176–181. https://doi.org/10.1038/nature10812

Cox, C. D., Nomura, T., Ziegler, C. S., Campbell, A. K., Wann, K. T., & Martinac, B. (2013). Selectivity mechanism of the mechanosensitive channel MscS revealed by probing channel subconducting states. *Nature Communications*, *4*(1), 2137. https://doi.org/10.1038/ncomms3137

Cox, Charles D., Bae, C., Ziegler, L., Hartley, S., Nikolova-Krstevski, V., Rohde, P. R., Ng, C.-A., Sachs, F., Gottlieb, P. A., & Martinac, B. (2016). Removal of the mechanoprotective influence of the cytoskeleton reveals PIEZO1 is gated by bilayer tension. *Nature Communications*, *7*(1), 10366. https://doi.org/10.1038/ncomms10366

Cox, Charles D., Bavi, N., & Martinac, B. (2019). Biophysical Principles of Ion-Channel-Mediated Mechanosensory Transduction. *Cell Reports*, *29*(1), 1–12. https://doi.org/10.1016/j.celrep.2019.08.075

Cuevas-Velazquez, C. L., & Dinneny, J. R. (2018). Organization out of disorder: Liquid–liquid phase separation in plants. *Current Opinion in Plant Biology*, *45*, 68–74. https://doi.org/10.1016/j.pbi.2018.05.005

Czempinski, K. (1997). New structure and function in plant K+ channels: KCO1, an outward rectifier with a steep Ca2+ dependency. *The EMBO Journal*, *16*(10), 2565–2575. https://doi.org/10.1093/emboj/16.10.2565

De Marchi, U., Checchetto, V., Zanetti, M., Teardo, E., Soccio, M., Formentin, E., Giacometti, G. M., Pastore, D., Zoratti, M., & Szabò, I. (2010). ATP-sensitive cation-channel in wheat (triticum durum Desf.): Identification and characterization of a plant mitochondrial channel by patch-clamp. *Cell Physiol Biochem*, *26*(6), 975–982. https://doi.org/10.1159/000324010

De Michele, R., Ast, C., Loqué, D., Ho, C.-H., Andrade, S. L., Lanquar, V., Grossmann, G., Gehne, S., Kumke, M. U., & Frommer, W. B. (2013). Fluorescent sensors reporting the activity of ammonium transceptors in live cells. *ELife*, *2*, e00800. https://doi.org/10.7554/eLife.00800

Deng, Z., Maksaev, G., Schlegel, A. M., Zhang, J., Rau, M., Fitzpatrick, J. A. J., Haswell, E. S., & Yuan, P. (2020). Structural mechanism for gating of a eukaryotic mechanosensitive channel of small conductance. *Nat Commun*, *11*(1), 3690. https://doi.org/10.1038/s41467-020-17538-1

Depuydt, M., Messens, J., & Collet, J.-F. (2011). How Proteins Form Disulfide Bonds. *Antioxidants & Redox Signaling*, *15*(1), 49–66. https://doi.org/10.1089/ars.2010.3575

Dietrich, P., Anschütz, U., Kugler, A., & Becker, D. (2010). Physiology and biophysics of plant ligand-gated ion channels. *Plant Biol (Stuttg)*, *12 Suppl 1*, 80–93. https://doi.org/10.1111/j.1438-8677.2010.00362.x

Dworsky, P. (1976). Comparative studies on membrane-associated, folded chromosomes from Escherichia coli. *J Bacteriol*, *126*(1), 64–71.

Edwards, M. D., Bartlett, W., & Booth, I. R. (2008). Pore Mutations of the Escherichia coli MscS Channel Affect Desensitization but Not Ionic Preference. *Biophysical Journal*, *94*(8), 3003–3013. https://doi.org/10.1529/biophysj.107.123448

Edwards, M. D., Black, S., Rasmussen, T., Rasmussen, A., Stokes, N. R., Stephen, T.-L., Miller, S., & Booth, I. R. (2012). Characterization of three novel mechanosensitive channel activities in Escherichia coli. *Channels*, *6*(4), 272–281. https://doi.org/10.4161/chan.20998

Edwards, M. D., Li, Y., Kim, S., Miller, S., Bartlett, W., Black, S., Dennison, S., Iscla, I., Blount, P., Bowie, J. U., & Booth, I. R. (2005). Pivotal role of the glycine-rich TM3 helix in gating the MscS mechanosensitive channel. *Nature Structural & Molecular Biology*, *12*(2), 113–119. https://doi.org/10.1038/nsmb895

Eng, R. C., & Sampathkumar, A. (2018). Getting into shape: The mechanics behind plant morphogenesis. *Current Opinion in Plant Biology*, *46*, 25–31. https://doi.org/10.1016/j.pbi.2018.07.002

Epstein, W., & Kim, B. S. (1971). Potassium Transport Loci in Escherichia coli K-12. *J Bacteriol*, *108*(2), 639–644.

Fischer, T., Stöttinger, S., Hinze, G., Bottin, A., Hu, N., & Basché, T. (2017). Single Semiconductor Nanocrystals under Compressive Stress: Reversible Tuning of the Emission Energy. *Nano Letters*, *17*(3), 1559–1563. https://doi.org/10.1021/acs.nanolett.6b04689

Freikamp, A., Mehlich, A., Klingner, C., & Grashoff, C. (2017). Investigating piconewton forces in cells by FRET-based molecular force microscopy. *Journal of Structural Biology*, *197*(1), 37–42. https://doi.org/10.1016/j.jsb.2016.03.011

Fruleux, A., Verger, S., & Boudaoud, A. (2019). Feeling Stressed or Strained? A Biophysical Model for Cell Wall Mechanosensing in Plants. *Front Plant Sci*, *10*. https://doi.org/10.3389/fpls.2019.00757

Furuichi, T., Iida, H., Sokabe, M., & Tatsumi, H. (2012). Expression of Arabidopsis MCA1 enhanced mechanosensitive channel activity in the Xenopus laevis oocyte plasma membrane. *Plant Signal Behav*, *7*(8), 1022–1026. https://doi.org/10.4161/psb.20783

Gerencser, A. A., Chinopoulos, C., Birket, M. J., Jastroch, M., Vitelli, C., Nicholls, D. G., & Brand, M. D. (2012). Quantitative measurement of mitochondrial membrane potential in cultured cells: Calcium-induced de- and hyperpolarization of neuronal mitochondria. *J Physiol (Lond.)*, *590*(12), 2845–2871. https://doi.org/10.1113/jphysiol.2012.228387

Ghanbari, M., Packirisamy, M., & Geitmann, A. (2018). Measuring the growth force of invasive plant cells using Flexure integrated Lab-on-a-Chip (FiLoC). *TECHNOLOGY*, *06*(03n04), 101–109. https://doi.org/10.1142/S2339547818500061

Gobert, A., Isayenkov, S., Voelker, C., Czempinski, K., & Maathuis, F. J. M. (2007). The two-pore channel TPK1 gene encodes the vacuolar K+ conductance and plays a role in K+ homeostasis. *Proceedings of the National Academy of Sciences*, *104*(25), 10726–10731. https://doi.org/10.1073/pnas.0702595104

Gode-Potratz, C. J., Kustusch, R. J., Breheny, P. J., Weiss, D. S., & McCarter, L. L. (2011). Surface sensing in Vibrio parahaemolyticus triggers a programme of gene expression that promotes colonization and virulence. *Molecular Microbiology*, *79*(1), 240–263. https://doi.org/10.1111/j.1365-2958.2010.07445.x

Goujon, A., Colom, A., Straková, K., Mercier, V., Mahecic, D., Manley, S., Sakai, N., Roux, A., & Matile, S. (2019). Mechanosensitive Fluorescent Probes to Image Membrane Tension in Mitochondria, Endoplasmic Reticulum, and Lysosomes. *Journal of the American Chemical Society*, *141*(8), 3380–3384. https://doi.org/10.1021/jacs.8b13189

Grashoff, C., Hoffman, B. D., Brenner, M. D., Zhou, R., Parsons, M., Yang, M. T., McLean, M. A., Sligar, S. G., Chen, C. S., Ha, T., & Schwartz, M. A. (2010). Measuring mechanical tension across vinculin reveals regulation of focal adhesion dynamics. *Nature*, *466*(7303), 263–266. https://doi.org/10.1038/nature09198

Guo, Y. R., & MacKinnon, R. (2017). Structure-based membrane dome mechanism for Piezo mechanosensitivity. *ELife*, *6*, e33660. https://doi.org/10.7554/eLife.33660

Halestrap, A. P. (2006). Calcium, mitochondria and reperfusion injury: A pore way to die. *Biochemical Society Transactions*, *34*(2), 232–237. https://doi.org/10.1042/BST0340232

Hamant, O., & Haswell, E. S. (2017). Life behind the wall: Sensing mechanical cues in plants. *BMC Biology*, *15*(1), 1–9. https://doi.org/10.1186/s12915-017-0403-5

Hamant, O., & Moulia, B. (2016). How do plants read their own shapes? *New Phytologist*, *212*(2), 333–337. https://doi.org/10.1111/nph.14143

Hamilton, E. S., Jensen, G. S., Maksaev, G., Katims, A., Sherp, A. M., & Haswell, E. S. (2015). Mechanosensitive channel MSL8 regulates osmotic forces during pollen hydration and germination. *Science*, *350*(6259), 438–441. https://doi.org/10.1126/science.aac6014

Hamilton, Eric S., & Haswell, E. S. (2017). The Tension-sensitive Ion Transport Activity of MSL8 is Critical for its Function in Pollen Hydration and Germination. *Plant and Cell Physiology*, *58*(7), 1222–1237. https://doi.org/10.1093/pcp/pcw230

Hamilton, Eric S., Schlegel, A. M., & Haswell, E. S. (2015). United in Diversity: Mechanosensitive Ion Channels in Plants. *Annual Review of Plant Biology*, *66*(1), 113–137. https://doi.org/10.1146/annurev-arplant-043014-114700

Haselwandter, C. A., & MacKinnon, R. (2018). Piezo's membrane footprint and its contribution to mechanosensitivity. *ELife*, *7*, e41968. https://doi.org/10.7554/eLife.41968

Haswell, E. S. (2007). MscS-Like Proteins in Plants. In *Current Topics in Membranes* (Vol. 58, pp. 329–359). Elsevier. https://doi.org/10.1016/S1063-5823(06)58013-5

Haswell, E. S., & Meyerowitz, E. M. (2006). MscS-like Proteins Control Plastid Size and Shape in Arabidopsis thaliana. *Curr Biol*, *16*(1), 1–11. https://doi.org/10.1016/j.cub.2005.11.044

Haswell, E. S., Peyronnet, R., Barbier-Brygoo, H., Meyerowitz, E. M., & Frachisse, J.-M. (2008). Two MscS Homologs Provide Mechanosensitive Channel Activities in the Arabidopsis Root. *Current Biology*, *18*(10), 730–734. https://doi.org/10.1016/j.cub.2008.04.039

Hedrich, R. (2012). Ion channels in plants. *Physiol Rev*, *92*(4), 1777–1811. https://doi.org/10.1152/physrev.00038.2011

Hernández-Hernández, V., Rueda, D., Caballero, L., Alvarez-Buylla, E. R., & Benítez, M. (2014). Mechanical forces as information: An integrated approach to plant and animal development. *Frontiers in Plant Science*, *5*. https://doi.org/10.3389/fpls.2014.00265

Herrera, N., Maksaev, G., Haswell, E. S., & Rees, D. C. (2018). Elucidating a role for the cytoplasmic domain in the Mycobacterium tuberculosis mechanosensitive channel of large conductance. *Scientific Reports*, *8*(1), 14566. https://doi.org/10.1038/s41598-018-32536-6

Huse, M. (2017). Mechanical forces in the immune system. *Nature Reviews Immunology*, *17*(11), 679–690. https://doi.org/10.1038/nri.2017.74

Iwai, S., & Uyeda, T. Q. P. (2008). Visualizing myosin–actin interaction with a genetically-encoded fluorescent strain sensor. *Proceedings of the National Academy of Sciences*, *105*(44), 16882–16887. https://doi.org/10.1073/pnas.0805513105

Jegla, T., Busey, G., & Assmann, S. M. (2018). Evolution and structural characteristics of plant voltage-gated K+ channels. *Plant Cell*, *30*(12), 2898–2909. https://doi.org/10.1105/tpc.18.00523

Jensen, G. S., Fal, K., Hamant, O., & Haswell, E. S. (2017). The RNA Polymerase-Associated Factor 1 Complex Is Required for Plant Touch Responses. *Journal of Experimental Botany*, *68*(3), 499–511. https://doi.org/10.1093/jxb/erw439

Jin, P., Bulkley, D., Guo, Y., Zhang, W., Guo, Z., Huynh, W., Wu, S., Meltzer, S., Cheng, T., Jan, L. Y., Jan, Y.-N., & Cheng, Y. (2017). Electron cryo-microscopy structure of the mechanotransduction channel NOMPC. *Nature*, *547*(7661), 118–122. https://doi.org/10.1038/nature22981

Jones, A. M., Grossmann, G., Danielson, J. Å., Sosso, D., Chen, L.-Q., Ho, C.-H., & Frommer, W. B. (2013). In vivo biochemistry: Applications for small molecule biosensors in plant biology. *Current Opinion in Plant Biology*, *16*(3), 389–395. https://doi.org/10.1016/j.pbi.2013.02.010

Kamaraju, K., Belyy, V., Rowe, I., Anishkin, A., & Sukharev, S. (2011). The pathway and spatial scale for MscS inactivation. *The Journal of General Physiology*, *138*(1), 49–57. https://doi.org/10.1085/jgp.201110606

Kasas, S., Stupar, P., & Dietler, G. (2018). AFM contribution to unveil pro- and eukaryotic cell mechanical properties. *Seminars in Cell & Developmental Biology*, *73*, 177–187. https://doi.org/10.1016/j.semcdb.2017.08.032

Kikuchi, K., Sugiura, M., Nishizawa-Harada, C., & Kimura, T. (2015). The application of the Escherichia coli giant spheroplast for drug screening with automated planar patch clamp system. *Biotechnol Rep (Amst)*, *7*, 17–23. https://doi.org/10.1016/j.btre.2015.04.007

Kloda, A, & Martinac, B. (2001). Structural and functional differences between two homologous mechanosensitive channels of Methanococcus jannaschii. *The EMBO Journal*, *20*(8), 1888–1896. https://doi.org/10.1093/emboj/20.8.1888

Kloda, Anna, & Martinac, B. (2001). Molecular Identification of a Mechanosensitive Channel in Archaea. *Biophys J*, *80*(1), 229–240. https://doi.org/10.1016/S0006-3495(01)76009-2

Koprowski, P., Grajkowski, W., Balcerzak, M., Filipiuk, I., Fabczak, H., & Kubalski, A. (2015). Cytoplasmic Domain of MscS Interacts with Cell Division Protein FtsZ: A Possible Non-Channel Function of the Mechanosensitive Channel in Escherichia Coli. *PLOS ONE*, *10*(5), e0127029. https://doi.org/10.1371/journal.pone.0127029

Koprowski, P., Grajkowski, W., Isacoff, E. Y., & Kubalski, A. (2011). Genetic Screen for Potassium Leaky Small Mechanosensitive Channels (MscS) in Escherichia coli RECOGNITION OF CYTOPLASMIC β DOMAIN AS A NEW GATING ELEMENT. *Journal of Biological Chemistry*, *286*(1), 877–888. https://doi.org/10.1074/jbc.M110.176131

Kostyuk, A. I., Demidovich, A. D., Kotova, D. A., Belousov, V. V., & Bilan, D. S. (2019). Circularly Permuted Fluorescent Protein-Based Indicators: History, Principles, and Classification. *International Journal of Molecular Sciences*, *20*(17), 4200. https://doi.org/10.3390/ijms20174200

Kung, C. (2005). A possible unifying principle for mechanosensation. *Nature*, *436*(7051), 647–654. https://doi.org/10.1038/nature03896

Kung, C., Martinac, B., & Sukharev, S. (2010). Mechanosensitive Channels in Microbes. *Annu Rev Microbiol*, *64*(1), 313–329. https://doi.org/10.1146/annurev.micro.112408.134106

Kurusu, T., Nishikawa, D., Yamazaki, Y., Gotoh, M., Nakano, M., Hamada, H., Yamanaka, T., Iida, K., Nakagawa, Y., Saji, H., Shinozaki, K., Iida, H., & Kuchitsu, K. (2012). Plasma membrane protein OsMCA1 is involved in regulation of hypo-osmotic shock-induced Ca2+ influx and modulates generation of reactive oxygen species in cultured rice cells. *BMC Plant Biol*, *12*, 11. https://doi.org/10.1186/1471-2229-12-11

Lai, J. Y., Poon, Y. S., Kaiser, J. T., & Rees, D. C. (2013). Open and shut: Crystal structures of the dodecylmaltoside solubilized mechanosensitive channel of small conductance from Escherichia coli and Helicobacter pylori at 4.4 Å and 4.1 Å resolutions. *Protein Sci*, *22*(4), 502–509. https://doi.org/10.1002/pro.2222

Lau, C., Hunter, M. J., Stewart, A., Perozo, E., & Vandenberg, J. I. (2018). Never at rest: Insights into the conformational dynamics of ion channels from cryo-electron microscopy. *The Journal of Physiology*, *596*(7), 1107–1119. https://doi.org/10.1113/JP274888

Lay, A., Sheppard, O. H., Siefe, C., McLellan, C. A., Mehlenbacher, R. D., Fischer, S., Goodman, M. B., & Dionne, J. A. (2019). Optically Robust and Biocompatible Mechanosensitive Upconverting Nanoparticles. *ACS Central Science*, *5*(7), 1211–1222. https://doi.org/10.1021/acscentsci.9b00300

Lay, A., Siefe, C., Fischer, S., Mehlenbacher, R. D., Ke, F., Mao, W. L., Alivisatos, A. P., Goodman, M. B., & Dionne, J. A. (2018). Bright, Mechanosensitive Upconversion with Cubic-Phase Heteroepitaxial Core–Shell Nanoparticles. *Nano Letters*, *18*(7), 4454–4459. https://doi.org/10.1021/acs.nanolett.8b01535

Lay, A., Wang, D. S., Wisser, M. D., Mehlenbacher, R. D., Lin, Y., Goodman, M. B., Mao, W. L., & Dionne, J. A. (2017). Upconverting Nanoparticles as Optical Sensors of Nano- to Micro-Newton Forces. *Nano Letters*, *17*(7), 4172–4177. https://doi.org/10.1021/acs.nanolett.7b00963

Lee, C. P., Maksaev, G., Jensen, G. S., Murcha, M. W., Wilson, M. E., Fricker, M., Hell, R., Haswell, E. S., Millar, A. H., & Sweetlove, L. J. (2016). MSL1 is a mechanosensitive ion channel that dissipates mitochondrial membrane potential and maintains redox homeostasis in mitochondria during abiotic stress. *The Plant Journal*, *88*(5), 809–825. https://doi.org/10.1111/tpj.13301

Lee, J., Wilson, M., Richardson, R., & Haswell, E. (2018). *Genetic and physical interactions between the organellar mechanosensitive ion channel homologs MSL1, MSL2, and MSL3 reveal a role for inter-organellar communication in plant development* [Preprint]. Plant Biology. https://doi.org/10.1101/487694

Levina, N. (1999). Protection of Escherichia coli cells against extreme turgor by activation of MscS and MscL mechanosensitive channels: Identification of genes required for MscS activity. *EMBO J*, *18*(7), 1730–1737. https://doi.org/10.1093/emboj/18.7.1730

Li, L., Liu, K., Hu, Y., Li, D., & Luan, S. (2008). Single mutations convert an outward K+ channel into an inward K+ channel. *Proceedings of the National Academy of Sciences*, *105*(8), 2871–2876. https://doi.org/10.1073/pnas.0712349105

Li, W., Yu, X., Xie, F., Zhang, B., Shao, S., Geng, C., Aziz, A. ur R., Liao, X., & Liu, B. (2018). A Membrane-Bound Biosensor Visualizes Shear Stress-Induced Inhomogeneous Alteration of Cell Membrane Tension. *IScience*, *7*, 180–190. https://doi.org/10.1016/j.isci.2018.09.002

Li, Y., Hu, Y., Wang, J., Liu, X., Zhang, W., & Sun, L. (2020). Structural Insights into a Plant Mechanosensitive Ion Channel MSL1. *Cell Rep*, *30*(13), 4518-4527.e3. https://doi.org/10.1016/j.celrep.2020.03.026

Lim, C.-G., Jang, J., & Kim, and C. (2018). Cellular machinery for sensing mechanical force. *BMB Reports*, *51*(12), 623–629. https://doi.org/10.5483/BMBRep.2018.51.12.237

Liu, Z., Gandhi, C. S., & Rees, D. C. (2009). Structure of a tetrameric MscL in an expanded intermediate state. *Nature*, *461*(7260), 120–124. https://doi.org/10.1038/nature08277

Lolicato, M., Riegelhaupt, P. M., Arrigoni, C., Clark, K. A., & Minor, D. L. (2014). Transmembrane Helix Straightening and Buckling Underlies Activation of Mechanosensitive and Thermosensitive K2P Channels. *Neuron*, *84*(6), 1198–1212. https://doi.org/10.1016/j.neuron.2014.11.017

Lopez-Bellido, R., Puig, S., Huang, P. J., Tsai, C.-R., Turner, H. N., Galko, M. J., & Gutstein, H. B. (2019). Growth Factor Signaling Regulates Mechanical Nociception in Flies and Vertebrates. *Journal of Neuroscience*, *39*(30), 6012–6030. https://doi.org/10.1523/JNEUROSCI.2950-18.2019

Ludewig, U., Wirén, N. von, & Frommer, W. B. (2002). Uniport of NH by the Root Hair Plasma Membrane Ammonium Transporter LeAMT1;1. *Journal of Biological Chemistry*, *277*(16), 13548–13555. https://doi.org/10.1074/jbc.M200739200

Maathuis, F. J. M. (2011). Vacuolar two-pore K+ channels act as vacuolar osmosensors. *New Phytologist*, *191*(1), 84–91. https://doi.org/10.1111/j.1469-8137.2011.03664.x

Machiyama, H., Tatsumi, H., & Sokabe, M. (2009). Structural Changes in the Cytoplasmic Domain of the Mechanosensitive Channel MscS During Opening. *Biophys J*, *97*(4), 1048–1057. https://doi.org/10.1016/j.bpj.2009.05.021

Majda, M., Sapala, A., Routier-Kierzkowska, A.-L., & Smith, R. S. (2019). Cellular Force Microscopy to Measure Mechanical Forces in Plant Cells. In F. Cvrčková & V. Žárský (Eds.), *Plant Cell Morphogenesis: Methods and Protocols* (pp. 215–230). Springer. https://doi.org/10.1007/978-1-4939-9469-4_14

Maksaev, G., & Haswell, E. S. (2012). MscS-Like10 is a stretch-activated ion channel from Arabidopsis thaliana with a preference for anions. *Proceedings of the National Academy of Sciences*, *109*(46), 19015–19020. https://doi.org/10.1073/pnas.1213931109

Maksaev, Grigory, & Haswell, E. S. (2011). Expression and characterization of the bacterial mechanosensitive channel MscS in Xenopus laevis oocytes. *The Journal of General Physiology*, *138*(6), 641–649. https://doi.org/10.1085/jgp.201110723

Maksaev, Grigory, & Haswell, E. S. (2015). Expressing and Characterizing Mechanosensitive Channels in Xenopus Oocytes. In E. B. Blancaflor (Ed.), *Plant Gravitropism* (Vol. 1309, pp. 151–169). Springer New York. https://doi.org/10.1007/978-1-4939-2697-8_13

Maksaev, Grigory, Shoots, J. M., Ohri, S., & Haswell, E. S. (2018). Nonpolar residues in the presumptive pore-lining helix of mechanosensitive channel MSL10 influence channel behavior and establish a nonconducting function. *Plant Direct*, *2*(6), e00059. https://doi.org/10.1002/pld3.59

Malcolm, H. R., & Blount, P. (2015). Mutations in a Conserved Domain of E. coli MscS to the Most Conserved Superfamily Residue Leads to Kinetic Changes. *PLoS ONE*, *10*(9), e0136756. https://doi.org/10.1371/journal.pone.0136756

Malcolm, H. R., Heo, Y.-Y., Elmore, D. E., & Maurer, J. A. (2011). Defining the Role of the Tension Sensor in the Mechanosensitive Channel of Small Conductance. *Biophysical Journal*, *101*(2), 345–352. https://doi.org/10.1016/j.bpj.2011.05.058

Malcolm, H. R., & Maurer, J. A. (2012). The Mechanosensitive Channel of Small Conductance (MscS) Superfamily: Not Just Mechanosensitive Channels Anymore. *ChemBioChem*, *13*(14), 2037–2043. https://doi.org/10.1002/cbic.201200410

Martinac, B., Buechner, M., Delcour, A. H., Adler, J., & Kung, C. (1987). Pressure-sensitive ion channel in Escherichia coli. *Proceedings of the National Academy of Sciences*, *84*(8), 2297–2301. https://doi.org/10.1073/pnas.84.8.2297

Martinac, B., Rohde, P. R., Cranfield, C. G., & Nomura, T. (2013). Patch clamp electrophysiology for the study of bacterial ion channels in giant spheroplasts of E. coli. *Methods Mol Biol*, *966*, 367–380. https://doi.org/10.1007/978-1-62703-245-2_23

Meng, F., & Sachs, F. (2012). Orientation-based FRET sensor for real-time imaging of cellular forces. *Journal of Cell Science*, *125*(3), 743–750. https://doi.org/10.1242/jcs.093104

Meng, F., Suchyna, T. M., Lazakovitch, E., Gronostajski, R. M., & Sachs, F. (2011). Real Time FRET Based Detection of Mechanical Stress in Cytoskeletal and Extracellular Matrix Proteins. *Cellular and Molecular Bioengineering*, *4*(2), 148–159. https://doi.org/10.1007/s12195-010-0140-0

Meng, F., Suchyna, T. M., & Sachs, F. (2008). A fluorescence energy transfer-based mechanical stress sensor for specific proteins in situ. *The FEBS Journal*, *275*(12), 3072–3087. https://doi.org/10.1111/j.1742-4658.2008.06461.x

Meyer, A. J., & Dick, T. P. (2010). Fluorescent Protein-Based Redox Probes. *Antioxidants & Redox Signaling*, *13*(5), 621–650. https://doi.org/10.1089/ars.2009.2948

Miller, S. (2003). Domain organization of the MscS mechanosensitive channel of Escherichia coli. *The EMBO Journal*, *22*(1), 36–46. https://doi.org/10.1093/emboj/cdg011

Molecular Devices. (2012). *The Axon ™ Guide A guide to Electrophysiology and*.

Mori, K., Renhu, N., Naito, M., Nakamura, A., Shiba, H., Yamamoto, T., Suzaki, T., Iida, H., & Miura, K. (2018). Ca2+-permeable mechanosensitive channels MCA1 and MCA2 mediate cold-induced cytosolic Ca2+ increase and cold tolerance in Arabidopsis. *Sci Rep*, *8*(1), 550. https://doi.org/10.1038/s41598-017-17483-y

Moseyko, N., & Feldman, L. J. (2001). Expression of pH-sensitive green fluorescent protein in Arabidopsis thaliana. *Plant, Cell & Environment*, *24*(5), 557–563. https://doi.org/10.1046/j.1365-3040.2001.00703.x

Mousavi, S. A. R., Chauvin, A., Pascaud, F., Kellenberger, S., & Farmer, E. E. (2013). GLUTAMATE RECEPTOR-LIKE genes mediate leaf-to-leaf wound signalling. *Nature*, *500*(7463), 422–426. https://doi.org/10.1038/nature12478

Murthy, S. E., Dubin, A. E., Whitwam, T., Jojoa-Cruz, S., Cahalan, S. M., Mousavi, S. A. R., Ward, A. B., & Patapoutian, A. (2018). OSCA/TMEM63 are an evolutionarily conserved family of mechanically activated ion channels. *ELife*, *7*, e41844. https://doi.org/10.7554/eLife.41844

Nakagawa, Y., Katagiri, T., Shinozaki, K., Qi, Z., Tatsumi, H., Furuichi, T., Kishigami, A., Sokabe, M., Kojima, I., Sato, S., Kato, T., Tabata, S., Iida, K., Terashima, A., Nakano, M., Ikeda, M., Yamanaka, T., & Iida, H. (2007).

Arabidopsis plasma membrane protein crucial for Ca2+ influx and touch sensing in roots. *PNAS*, *104*(9), 3639–3644. https://doi.org/10.1073/pnas.0607703104

Nakayama, Y., Fujiu, K., Sokabe, M., & Yoshimura, K. (2007). Molecular and electrophysiological characterization of a mechanosensitive channel expressed in the chloroplasts of Chlamydomonas. *PNAS*, *104*(14), 5883–5888. https://doi.org/10.1073/pnas.0609996104

Nakayama, Yoshitaka, Yoshimura, K., & Iida, H. (2013). Electrophysiological Characterization of the Mechanosensitive Channel MscCG in Corynebacterium glutamicum. *Biophys J*, *105*(6), 1366–1375. https://doi.org/10.1016/j.bpj.2013.06.054

Nomura, T., Cranfield, C. G., Deplazes, E., Owen, D. M., Macmillan, A., Battle, A. R., Constantine, M., Sokabe, M., & Martinac, B. (2012). Differential effects of lipids and lyso-lipids on the mechanosensitivity of the mechanosensitive channels MscL and MscS. *Proceedings of the National Academy of Sciences*, *109*(22), 8770–8775. https://doi.org/10.1073/pnas.1200051109

Nomura, Takeshi, Sokabe, M., & Yoshimura, K. (2006). Lipid-Protein Interaction of the MscS Mechanosensitive Channel Examined by Scanning Mutagenesis. *Biophysical Journal*, *91*(8), 2874–2881. https://doi.org/10.1529/biophysj.106.084541

Nomura, Takeshi, Sokabe, M., & Yoshimura, K. (2008). Interaction between the Cytoplasmic and Transmembrane Domains of the Mechanosensitive Channel MscS. *Biophys J*, *94*(5), 1638–1645. https://doi.org/10.1529/biophysj.107.114785

Nourse, J. L., & Pathak, M. M. (2017). How cells channel their stress: Interplay between Piezo1 and the cytoskeleton. *Seminars in Cell & Developmental Biology*, *71*, 3–12. https://doi.org/10.1016/j.semcdb.2017.06.018

Oesterle, A. (2018). *Sutter Instrument Company Pipette Cookbook*. https://doi.org/10.1002/ejoc.201200111

Okada, K., Moe, P. C., & Blount, P. (2002). Functional Design of Bacterial Mechanosensitive Channels COMPARISONS AND CONTRASTS ILLUMINATED BY RANDOM MUTAGENESIS. *J Biol Chem*, *277*(31), 27682–27688. https://doi.org/10.1074/jbc.M202497200

Perozo, E., Kloda, A., Cortes, D. M., & Martinac, B. (2002). Physical principles underlying the transduction of bilayer deformation forces during mechanosensitive channel gating. *Nature Structural Biology*, *9*(9), 696–703. https://doi.org/10.1038/nsb827

Persat, A. (2017). Bacterial mechanotransduction. *Current Opinion in Microbiology*, *36*, 1–6. https://doi.org/10.1016/j.mib.2016.12.002

Persat, A., Nadell, C. D., Kim, M. K., Ingremeau, F., Siryaporn, A., Drescher, K., Wingreen, N. S., Bassler, B. L., Gitai, Z., & Stone, H. A. (2015). The Mechanical World of Bacteria. *Cell*, *161*(5), 988–997. https://doi.org/10.1016/j.cell.2015.05.005

Petrov, E., Palanivelu, D., Constantine, M., Rohde, P. R., Cox, C. D., Nomura, T., Minor, D. L., & Martinac, B. (2013). Patch-Clamp Characterization of the MscS-like Mechanosensitive Channel from Silicibacter pomeroyi. *Biophys J*, *104*(7), 1426–1434. https://doi.org/10.1016/j.bpj.2013.01.055

Phillips, R., Ursell, T., Wiggins, P., & Sens, P. (2009). Emerging roles for lipids in shaping membrane-protein function. *Nature*, *459*(7245), 379–385. https://doi.org/10.1038/nature08147

Pivetti, C. D., Yen, M.-R., Miller, S., Busch, W., Tseng, Y.-H., Booth, I. R., & Saier, M. H. (2003). Two Families of Mechanosensitive Channel Proteins. *MMBR*, *67*(1), 66–85. https://doi.org/10.1128/MMBR.67.1.66-85.2003

Pliotas, C., Dahl, A. C. E., Rasmussen, T., Mahendran, K. R., Smith, T. K., Marius, P., Gault, J., Banda, T., Rasmussen, A., Miller, S., Robinson, C. V., Bayley, H., Sansom, M. S. P., Booth, I. R., & Naismith, J. H. (2015). The role of lipids in mechanosensation. *Nat Struct Mol Biol*, *22*(12), 991–998. https://doi.org/10.1038/nsmb.3120

Pottosin, I., & Dobrovinskaya, O. (2015). Ion channels in native chloroplast membranes: Challenges and potential for direct patch-clamp studies. *Front Physiol*, *6*, 396. https://doi.org/10.3389/fphys.2015.00396

Ranade, S. S., Syeda, R., & Patapoutian, A. (2015). Mechanically Activated Ion Channels. *Neuron*, *87*(6), 1162–1179. https://doi.org/10.1016/j.neuron.2015.08.032

Rasmussen, A., Rasmussen, T., Edwards, M. D., Schauer, D., Schumann, U., Miller, S., & Booth, I. R. (2007). The Role of Tryptophan Residues in the Function and Stability of the Mechanosensitive Channel MscS from Escherichia coli. *Biochemistry*, *46*(38), 10899–10908. https://doi.org/10.1021/bi701056k

Rasmussen, T., Flegler, V. J., Rasmussen, A., & Böttcher, B. (2019). Structure of the Mechanosensitive Channel MscS Embedded in the Membrane Bilayer. *Journal of Molecular Biology*, *431*(17), 3081–3090. https://doi.org/10.1016/j.jmb.2019.07.006

Rasmussen, Tim, Rasmussen, A., Yang, L., Kaul, C., Black, S., Galbiati, H., Conway, S. J., Miller, S., Blount, P., & Booth, I. R. (2019). Interaction of the Mechanosensitive Channel, MscS, with the Membrane Bilayer through Lipid Intercalation into Grooves and Pockets. *Journal of Molecular Biology*, *431*(17), 3339–3352. https://doi.org/10.1016/j.jmb.2019.05.043

Reading, E., Walton, T. A., Liko, I., Marty, M. T., Laganowsky, A., Rees, D. C., & Robinson, C. V. (2015). The Effect of Detergent, Temperature, and Lipid on the Oligomeric State of MscL Constructs: Insights from Mass Spectrometry. *Chemistry & Biology*, *22*(5), 593–603. https://doi.org/10.1016/j.chembiol.2015.04.016

Reddy, B., Bavi, N., Lu, A., Park, Y., & Perozo, E. (2019). Molecular basis of force-from-lipids gating in the mechanosensitive channel MscS. *ELife*, *8*, e50486. https://doi.org/10.7554/eLife.50486

Reimann, R., Kah, D., Mark, C., Dettmer, J., Reimann, T. M., Gerum, R. C., Geitmann, A., Fabry, B., Dietrich, P., & Kost, B. (2020). Durotropic Growth of Pollen Tubes. *Plant Physiology*, *183*(2), 558–569. https://doi.org/10.1104/pp.19.01505

Renner, L. D., & Weibel, D. B. (2011). Cardiolipin microdomains localize to negatively curved regions of Escherichia coli membranes. *PNAS*, *108*(15), 6264–6269. https://doi.org/10.1073/pnas.1015757108

Ridone, P., Grage, S. L., Patkunarajah, A., Battle, A. R., Ulrich, A. S., & Martinac, B. (2018). “Force-from-lipids” gating of mechanosensitive channels modulated by PUFAs. *Journal of the Mechanical Behavior of Biomedical Materials*, *79*, 158–167. https://doi.org/10.1016/j.jmbbm.2017.12.026

Ridone, P., Nakayama, Y., Martinac, B., & Battle, A. R. (2015). Patch clamp characterization of the effect of cardiolipin on MscS of E. coli. *European Biophysics Journal*, *44*(7), 567–576. https://doi.org/10.1007/s00249-015-1020-2

Roca-Cusachs, P., Conte, V., & Trepat, X. (2017). Quantifying forces in cell biology. *Nature Cell Biology*, *19*(7), 742–751. https://doi.org/10.1038/ncb3564

Roignant, J., Badel, É., Leblanc-Fournier, N., Brunel-Michac, N., Ruelle, J., Moulia, B., & Decourteix, M. (2018). Feeling stretched or compressed? The multiple mechanosensitive responses of wood formation to bending. *Annals of Botany*, *121*(6), 1151–1161. https://doi.org/10.1093/aob/mcx211

Rojas, E., Theriot, J. A., & Huang, K. C. (2014). Response of Escherichia coli growth rate to osmotic shock. *PNAS*, *111*(21), 7807–7812. https://doi.org/10.1073/pnas.1402591111

Romantsov, T., Battle, A. R., Hendel, J. L., Martinac, B., & Wood, J. M. (2010). Protein localization in Escherichia coli cells: Comparison of the cytoplasmic membrane proteins ProP, LacY, ProW, AqpZ, MscS, and MscL. *J Bacteriol*, *192*(4), 912–924. https://doi.org/10.1128/JB.00967-09

Rowe, I., Anishkin, A., Kamaraju, K., Yoshimura, K., & Sukharev, S. (2014). The cytoplasmic cage domain of the mechanosensitive channel MscS is a sensor of macromolecular crowding. *J Gen Physiol*, *143*(5), 543–557. https://doi.org/10.1085/jgp.201311114

Rowe, I., Elahi, M., Huq, A., & Sukharev, S. (2013). The mechanoelectrical response of the cytoplasmic membrane of Vibrio cholerae. *The Journal of General Physiology*, *142*(1), 75–85. https://doi.org/10.1085/jgp.201310985

Salvador-Recatalà, V. (2016). New roles for the GLUTAMATE RECEPTOR-LIKE 3.3, 3.5, and 3.6 genes as on/off switches of wound-induced systemic electrical signals. *Plant Signaling & Behavior*, *11*(4), e1161879. https://doi.org/10.1080/15592324.2016.1161879

Saotome, K., Murthy, S. E., Kefauver, J. M., Whitwam, T., Patapoutian, A., & Ward, A. B. (2018). Structure of the mechanically activated ion channel Piezo1. *Nature*, *554*(7693), 481–486. https://doi.org/10.1038/nature25453

Scherzer, S., Federle, W., Al-Rasheid, K. a. S., & Hedrich, R. (2019). Venus flytrap trigger hairs are micronewton mechano-sensors that can detect small insect prey. *Nature Plants*, *5*(7), 670–675. https://doi.org/10.1038/s41477-019-0465-1

Scherzer, Sönke, Shabala, L., Hedrich, B., Fromm, J., Bauer, H., Munz, E., Jakob, P., Al-Rascheid, K. A. S., Kreuzer, I., Becker, D., Eiblmeier, M., Rennenberg, H., Shabala, S., Bennett, M., Neher, E., & Hedrich, R. (2017). Insect haptoelectrical stimulation of Venus flytrap triggers exocytosis in gland cells. *Proceedings of the National Academy of Sciences*, *114*(18), 4822–4827. https://doi.org/10.1073/pnas.1701860114

Schindelin, J., Arganda-Carreras, I., Frise, E., Kaynig, V., Longair, M., Pietzsch, T., Preibisch, S., Rueden, C., Saalfeld, S., Schmid, B., Tinevez, J.-Y., White, D. J., Hartenstein, V., Eliceiri, K., Tomancak, P., & Cardona, A. (2012). Fiji: An open-source platform for biological-image analysis. *Nature Methods*, *9*(7), 676–682. https://doi.org/10.1038/nmeth.2019

Schlegel, A. M., & Haswell, E. S. (2020). Analyzing plant mechanosensitive ion channels expressed in giant E. coli spheroplasts by single-channel patch-clamp electrophysiology. In *Methods in Cell Biology* (p. S0091679X20300133). Elsevier. https://doi.org/10.1016/bs.mcb.2020.02.007

Schwarzländer, M., Logan, D. C., Johnston, I. G., Jones, N. S., Meyer, A. J., Fricker, M. D., & Sweetlove, L. J. (2012). Pulsing of Membrane Potential in Individual Mitochondria: A Stress-Induced Mechanism to Regulate Respiratory Bioenergetics in *Arabidopsis*. *Plant Cell*, *24*(3), 1188–1201. https://doi.org/10.1105/tpc.112.096438

Sen, S., & Kumar, S. (2010). Combining mechanical and optical approaches to dissect cellular mechanobiology. *Journal of Biomechanics*, *43*(1), 45–54. https://doi.org/10.1016/j.jbiomech.2009.09.008

Siedlik, M. J., Varner, V. D., & Nelson, C. M. (2016). Pushing, pulling, and squeezing our way to understanding mechanotransduction. *Methods*, *94*, 4–12. https://doi.org/10.1016/j.ymeth.2015.08.019

Stanishneva-Konovalova, T. B., Derkacheva, N. I., Polevova, S. V., & Sokolova, O. S. (2016). The Role of BAR Domain Proteins in the Regulation of Membrane Dynamics. *Acta Naturae*, *8*(4), 60–69.

Steinbacher, S., Bass, R., Strop, P., & Rees, D. C. (2007). Structures of the Prokaryotic Mechanosensitive Channels MscL and MscS. In *Current Topics in Membranes* (Vol. 58, pp. 1–24). Elsevier. https://doi.org/10.1016/S1063-5823(06)58001-9

Sukharev, S. (2002). Purification of the Small Mechanosensitive Channel of Escherichia coli (MscS): The Subunit Structure, Conduction, and Gating Characteristics in Liposomes. *Biophysical Journal*, *83*(1), 290–298. https://doi.org/10.1016/S0006-3495(02)75169-2

Sukharev, S., Akitake, B., & Anishkin, A. (2007). The Bacterial Mechanosensitive Channel MscS: Emerging Principles of Gating and Modulation. In *Current Topics in Membranes* (Vol. 58, pp. 235–267). Academic Press. https://doi.org/10.1016/S1063-5823(06)58009-3

Sukharev, S. I., Blount, P., Martinac, B., Blattnert, F. R., & Kung, C. (1994). A large-conductance mechanosensitive ion channel in E. coli encoded by mscL alone. *Nature*, *368*(6468), 265–268.

Sun, Y., Sun, T.-L., & Huang, H. W. (2014). Physical properties of Escherichia coli spheroplast membranes. *Biophys J*, *107*(9), 2082–2090. https://doi.org/10.1016/j.bpj.2014.09.034

Syeda, R., Florendo, M. N., Cox, C. D., Kefauver, J. M., Santos, J. S., Martinac, B., & Patapoutian, A. (2016). Piezo1 Channels Are Inherently Mechanosensitive. *Cell Reports*, *17*(7), 1739–1746. https://doi.org/10.1016/j.celrep.2016.10.033

Teng, J., Loukin, S., Anishkin, A., & Kung, C. (2015). The force-from-lipid (FFL) principle of mechanosensitivity, at large and in elements. *Pflügers Archiv - European Journal of Physiology*, *467*(1), 27–37. https://doi.org/10.1007/s00424-014-1530-2

Tsien, R. Y. (1998). THE GREEN FLUORESCENT PROTEIN. *Annual Review of Biochemistry*, *67*(1), 509–544. https://doi.org/10.1146/annurev.biochem.67.1.509

Vaahtera, L., Schulz, J., & Hamann, T. (2019). Cell wall integrity maintenance during plant development and interaction with the environment. *Nature Plants*, *5*(9), 924–932. https://doi.org/10.1038/s41477-019-0502-0

van den Berg, J., Galbiati, H., Rasmussen, A., Miller, S., & Poolman, B. (2016). On the mobility, membrane location and functionality of mechanosensitive channels in Escherichia coli. *Sci Rep*, *6*(1), 1–11. https://doi.org/10.1038/srep32709

Vásquez, V. (2013). MscS Inactivation: An Exception rather than the Rule. An Extremophilic MscS Reveals Diversity within the Family. *Biophysical Journal*, *104*(7), 1391–1393. https://doi.org/10.1016/j.bpj.2013.02.010

Vásquez, V., Sotomayor, M., Cordero-Morales, J., Schulten, K., & Perozo, E. (2008). A Structural Mechanism for MscS Gating in Lipid Bilayers. *Science*, *321*(5893), 1210–1214. https://doi.org/10.1126/science.1159674

Veley, K. M., Maksaev, G., Frick, E. M., January, E., Kloepper, S. C., & Haswell, E. S. (2014). Arabidopsis MSL10 Has a Regulated Cell Death Signaling Activity That Is Separable from Its Mechanosensitive Ion Channel Activity. *The Plant Cell*, *26*(7), 3115–3131. https://doi.org/10.1105/tpc.114.128082

Veley, K. M., Marshburn, S., Clure, C. E., & Haswell, E. S. (2012). Mechanosensitive Channels Protect Plastids from Hypoosmotic Stress During Normal Plant Growth. *Current Biology*, *22*(5), 408–413. https://doi.org/10.1016/j.cub.2012.01.027

Vining, K. H., & Mooney, D. J. (2017). Mechanical forces direct stem cell behaviour in development and regeneration. *Nature Reviews Molecular Cell Biology*, *18*(12), 728–742. https://doi.org/10.1038/nrm.2017.108

Virolainen, E., Blokhina, O., & Fagerstedt, K. (2002). Ca2+-induced High Amplitude Swelling and Cytochrome c Release From Wheat (Triticum aestivum L.) Mitochondria Under Anoxic Stress. *Annals of Botany*, *90*(4), 509–516. https://doi.org/10.1093/aob/mcf221

Vogler, H., Felekis, D., Nelson, B. J., & Grossniklaus, U. (2015). Measuring the Mechanical Properties of Plant Cell Walls. *Plants*, *4*(2), 167–182. https://doi.org/10.3390/plants4020167

Volkov, A. G., Harris, S. L., Vilfranc, C. L., Murphy, V. A., Wooten, J. D., Paulicin, H., Volkova, M. I., & Markin, V. S. (2013). Venus flytrap biomechanics: Forces in the Dionaea muscipula trap. *Journal of Plant Physiology*, *170*(1), 25–32. https://doi.org/10.1016/j.jplph.2012.08.009

Walton, T. A., & Rees, D. C. (2013). Structure and stability of the C-terminal helical bundle of the E. coli mechanosensitive channel of large conductance. *Protein Science*, *22*(11), 1592–1601. https://doi.org/10.1002/pro.2360

Wang, W., Black, S. S., Edwards, M. D., Miller, S., Morrison, E. L., Bartlett, W., Dong, C., Naismith, J. H., & Booth, I. R. (2008). The Structure of an Open Form of an E. coli Mechanosensitive Channel at 3.45 A Resolution. *Science*, *321*(5893), 1179–1183. https://doi.org/10.1126/science.1159262

Wiggins, P., & Phillips, R. (2005). Membrane-Protein Interactions in Mechanosensitive Channels. *Biophysical Journal*, *88*(2), 880–902. https://doi.org/10.1529/biophysj.104.047431

Wood, J. M. (2011). Bacterial Osmoregulation: A Paradigm for the Study of Cellular Homeostasis. *Annual Review of Microbiology*, *65*(1), 215–238. https://doi.org/10.1146/annurev-micro-090110-102815

Wu, J., Goyal, R., & Grandl, J. (2016). Localized force application reveals mechanically sensitive domains of Piezo1. *Nature Communications*, *7*(1), 12939. https://doi.org/10.1038/ncomms12939

Xue, F., Cox, C. D., Bavi, N., Rohde, P. R., Nakayama, Y., & Martinac, B. (2020). Membrane stiffness is one of the key determinants of E. coli MscS channel mechanosensitivity. *Biochimica et Biophysica Acta (BBA) - Biomembranes*, *1862*(5), 183203. https://doi.org/10.1016/j.bbamem.2020.183203

Yamanaka, T., Nakagawa, Y., Mori, K., Nakano, M., Imamura, T., Kataoka, H., Terashima, A., Iida, K., Kojima, I., Katagiri, T., Shinozaki, K., & Iida, H. (2010). MCA1 and MCA2 that mediate Ca2+ uptake have distinct and overlapping roles in Arabidopsis. *Plant Physiol*, *152*(3), 1284–1296. https://doi.org/10.1104/pp.109.147371

Yang, C., Zhang, X., Guo, Y., Meng, F., Sachs, F., & Guo, J. (2015). Mechanical dynamics in live cells and fluorescence-based force/tension sensors. *Biochim Biophys Acta*, *1853*(8), 1889–1904. https://doi.org/10.1016/j.bbamcr.2015.05.001

Yu, J., Zhang, B., Zhang, Y., Xu, C., Zhuo, W., Ge, J., Li, J., Gao, N., Li, Y., & Yang, M. (2018). A binding-block ion selective mechanism revealed by a Na/K selective channel. *Protein & Cell*, *9*(7), 629–639. https://doi.org/10.1007/s13238-017-0465-8

Yuan, F., Yang, H., Xue, Y., Kong, D., Ye, R., Li, C., Zhang, J., Theprungsirikul, L., Shrift, T., Krichilsky, B., Johnson, D. M., Swift, G. B., He, Y., Siedow, J. N., & Pei, Z.-M. (2014). OSCA1 mediates osmotic-stress-evoked Ca2+ increases vital for osmosensing in Arabidopsis. *Nature*, *514*(7522), 367–371. https://doi.org/10.1038/nature13593

Zancani, M., Casolo, V., Petrussa, E., Peresson, C., Patui, S., Bertolini, A., De Col, V., Braidot, E., Boscutti, F., & Vianello, A. (2015). The Permeability Transition in Plant Mitochondria: The Missing Link. *Frontiers in Plant Science*, *6*. https://doi.org/10.3389/fpls.2015.01120

Zhang, M., Wang, D., Kang, Y., Wu, J.-X., Yao, F., Pan, C., Yan, Z., Song, C., & Chen, L. (2018). Structure of the mechanosensitive OSCA channels. *Nat Struct Mol Biol*, *25*(9), 850–858. https://doi.org/10.1038/s41594-018-0117-6

Zhang, W., Cheng, L. E., Kittelmann, M., Li, J., Petkovic, M., Cheng, T., Jin, P., Guo, Z., Göpfert, M. C., Jan, L. Y., & Jan, Y. N. (2015). Ankyrin Repeats Convey Force to Gate the NOMPC Mechanotransduction Channel. *Cell*, *162*(6), 1391–1403. https://doi.org/10.1016/j.cell.2015.08.024

Zhang, X., Wang, J., Feng, Y., Ge, J., Li, W., Sun, W., Iscla, I., Yu, J., Blount, P., Li, Y., & Yang, M. (2012). Structure and molecular mechanism of an anion-selective mechanosensitive channel of small conductance. *Proceedings of the National Academy of Sciences*, *109*(44), 18180–18185. https://doi.org/10.1073/pnas.1207977109

Zhang, Z., Tong, X., Liu, S.-Y., Chai, L.-X., Zhu, F.-F., Zhang, X.-P., Zou, J.-Z., & Wang, X.-B. (2019). Genetic analysis of a Piezo-like protein suppressing systemic movement of plant viruses in Arabidopsis thaliana. *Sci Rep*, *9*, 3187. https://doi.org/10.1038/s41598-019-39436-3

Zhao, F., Chen, W., & Traas, J. (2018). Mechanical signaling in plant morphogenesis. *Current Opinion in Genetics & Development*, *51*, 26–30. https://doi.org/10.1016/j.gde.2018.04.001

Zhao, Q., Wu, K., Geng, J., Chi, S., Wang, Y., Zhi, P., Zhang, M., & Xiao, B. (2016). Ion Permeation and Mechanotransduction Mechanisms of Mechanosensitive Piezo Channels. *Neuron*, *89*(6), 1248–1263. https://doi.org/10.1016/j.neuron.2016.01.046

Zhu, L., Zhao, W., Yan, Y., Liao, X., Bourtsalas, A., Dan, Y., Xiao, H., & Chen, X. (2020). Interaction between mechanosensitive channels embedded in lipid membrane. *Journal of the Mechanical Behavior of Biomedical Materials*, *103*, 103543. https://doi.org/10.1016/j.jmbbm.2019.103543

CV

ANGELA M. SCHLEGEL

PhD Candidate, Haswell Lab
Program in Plant and Microbial Biosciences
Division of Biology and Biomedical Sciences
Washington University in St. Louis

Angela.schlegel.ths@gmail.com

EDUCATION

Washington University in St. Louis 2013-2020 (expected)
Ph.D., Plant and Microbial Biosciences
Thesis Advisor: Dr. Elizabeth S. Haswell

University of Arizona 2009-2013
B.S., Biochemistry with Honors, *magna cum laude*
Minor in Chemistry
Undergraduate Thesis Advisor: Dr. Samuel K. Campos

EMPLOYMENT

CACTUS Communications Service Pte Ltd Sep 2018-Nov 2019
Freelance Editor, Biochemistry, Molecular Biology, Genetics

AWARDS, FELLOWSHIPS, and INTERNSHIPS

Washington University in St. Louis
William H. Danforth Fellowship in Plant Sciences 2014
Spencer T. and Ann W. Olin Fellowship 2013

University of Arizona
Lela E. Booher Memorial Scholarship 2013
University of Arizona Outstanding Biochemistry Senior 2013
Michael A. Wells Memorial Research Scholarship 2012
Undergraduate Biology Research Program Intern 2010-2013

PUBLICATIONS

1. A. M. Schlegel and E. S. Haswell. (2020). Charged Pore-Lining Residues are Required for Normal Channel Kinetics in the Eukaryotic Mechanosensitive Ion Channel MSL1. ***Channels.*** *Accepted*.

2. Z. Deng, G. Maksaev*, A. M. Schlegel*, J. Zhang, M. Rau, JAJ Fitzpatrick, E. S. Haswell and P. Yuan. (2020). Structural Mechanism for Gating of a Eukaryotic Mechanosensitive Ion Channel of Small Conductance. ***Nature Communications*** 11: 3690. https://doi.org/10.1038/s41467-020-17538-1. *Equal Contributions
3. A. M. Schlegel and E. S. Haswell. (2020). Analyzing plant mechanosensitive ion channels expressed in giant *E. coli* spheroplasts by single channel patch-clamp electrophysiology. ***Methods in Cell Biology.*** https://doi.org/10.1016/bs.mcb.2020.02.007
4. A. M. Schlegel and E. S. Haswell. (2020). Plant Biomechanics: No pain, no gain for birch tree stems. ***Current Biology*** 30: R164-166.
5. M.P. Bronnimann, C.M. Calton, S.F. Chiquette, S. Li, M. Lu, J.A. Chapman, K.N. Bratton, A.M. Schlegel, S.K. Campos. (2016). Furin Cleavage of L2 During Papillomavirus Infection: Minimal Dependence on Cyclophilins. ***Journal of Virology*** 90(14): 6224-34. doi: 10.1128/JVI.00038-16
6. E. S. Hamilton, A. M. Schlegel, E. S. Haswell. (2015). United in Diversity: Plant Mechanosensitive Channels. ***Annual Review of Plant Biology*** 66: 113-37. doi: 10.1146/annurev-arplant-043014-114700
7. C.M Calton, A.M. Schlegel, J.A. Chapman, S.K. Campos. (2013). Human Papillomavirus Type 16 Does Not Require Cathepsins L or B for Infection. ***Journal of General Virology.*** doi: 10.1099/vir.0.053694-0

TEACHING EXPERIENCE

Graduate Teaching Assistant Spring 2014

BIO3041: Plant Biotechnology and Genetic Engineering

Washington University in St. Louis

DEPARTMENT SEMINARS and CONFERENCE TALKS

1. "Mechanosensitive Ion Channel MscS-Like 1 (MSL1) Channel Behavior is Modulated by Charged Pore-Lining Residues", Angela M. Schlegel, Elizabeth S. Haswell, Lightning Talk, Force Gated Ion Channels Conference, Berlin, Germany (October 2018)
2. "From Proteins to Organisms: Using Single Channel Experiments to Address Larger Biological Questions in Arabidopsis", WUSM CIMED seminar, St. Louis, MO (April 2018)
3. "Structure/Function Analysis of the Arabidopsis Mitochondrial Mechanosensitive Ion Channel MSL1", Department Bioforum Seminar, WUSTL Department of Biology, St. Louis, MO (November 2017)
4. "Stretching the Limits of Measurement: Development a Lateral Membrane Tension Biosensor", Angela M. Schlegel, Ryan A. Richardson, Elizabeth S. Haswell, Short Talk, Gordon Research Conference on Bacterial Cell Surfaces, West Dover, VT (June-July 2016)
5. "The Practice and Purpose of Mechanosensation in Plants", Angela M Schlegel, Elizabeth S .Haswell, Midwest Plant Cell Dynamics Meeting, Madison, WI (June 2014)

CONFERENCE POSTER PRESENTATIONS

1. "Mechanosensitive Ion Channel MscS-Like 1 (MSL1) Channel Behavior is Modulated by Charged Pore-Lining Residues", Angela M Schlegel, Elizabeth S Haswell, Force Gated Ion Channels Conference, Berlin, Germany (October 2018)

2. "Structure/Function Analysis of the Arabidopsis Mitochondrial Mechanosensitive Ion Channel MSL1", Angela M Schlegel, Gregory S Jensen, Grigory Maksaev, Elizabeth S Haswell" at Gordon Research Conference on Organellar Channels & Transporters, West Dover, VT (July-August 2017)
3. "Stretching the Limits of Measurement: Development a Lateral Membrane Tension Biosensor", Angela M Schlegel, Ryan A Richardson, Elizabeth S Haswell, Gordon Research Conference on Bacterial Cell Surfaces, West Dover, VT (June-July 2016)
4. "Towards a Genetically Encoded Fluorescence-Based Membrane Tension Sensor", Angela M Schlegel, Emma January, Adam Cohen, Elizabeth S Haswell, American Society of Plant Biologists annual meeting, Portland, OR (July 2014)
5. "The Practice and Purpose of Mechanosensation in Plants", Angela M Schlegel, Elizabeth S Haswell, Midwest Plant Cell Dynamics Meeting, Madison, WI (June 2014)
6. "Possible Role for Adaptor Protein Complexes in Sorting of Human Papillomavirus", Angela M Schlegel, Janice A Chapman, Samuel K Campos, American Society for Microbiology Arizona/Southern Nevada branch meeting, University of Arizona, Tucson, AZ (April 2013)
7. "The Identification of Enzymes Used in *Salvia divinorum* to Produce Salvinorin A", Angela M Schlegel, David R Gang, American Society of Plant Biologists (ASPB) Western Section annual meeting, Tucson, AZ (April 2009)
8. "The Identification of Enzymes Used in *Salvia divinorum* to Produce Salvinorin A" Angela M Schlegel, David R Gang, Society for Molecular Biology and Evolution (SMBE) annual meeting, University of Iowa, Iowa City, IA (June 2009)

REFERENCES

Dr. Elizabeth S. Haswell
Professor, HHMI-Simons Foundation Scholar
Washington University in St. Louis, St. Louis, MO
Office: (314) 935-9223
E-mail: ehaswell@wustl.edu

Dr. Joseph Jez
Professor, Biology Department Chair, HHMI Professor
Washington University in St. Louis, St. Louis, MO
Office: (314) 935-3376
E-mail: jjez@biology2.wustl.edu

Dr. Samuel K. Campos
Associate Professor
Department of Immunobiology, BIO5 Institute
University of Arizona, Tucson, AZ
Office: (520) 626-4842
E-mail: skcampos@email.arizona.edu

Dr. David R. Gang
Professor and Fellow, Institute of Biological Chemistry
Washington State University, Pullman, WA
Office: (509) 335-0550

Email: gangd@wsu.edu